Addis Ababa University
College of Technology and Built Environment
School of Electrical and Computer Engineering

Parameter Estimation and Sensorless Control of Variable Phase-Pole Induction Machines in the Context of Magnetic Pole Transition

By Mesfin Tilahune Tessema

A dissertation submitted to the Graduate School of Electrical and Computer Engineering in partial fulfillment of the requirements for the Degree of Doctor of Philosophy (Ph.D.) in Electrical Engineering (Electrical Control Engineering).

May, 2025

Addis Ababa, Ethiopia

Supervisor

Mengesha Mamo (Ph.D.)
Addis Ababa University,
College of Engineering and Environmental Built,
Addis Ababa,
Ethiopia

Supervisor

Luca Peretti (Ph.D.)
KTH Royal Institute of Technology,
Stockholm,
Sweden

Addis Ababa University
College of Technology and Built Environment
School of Electrical and Computer Engineering

Parameter Estimation and Sensorless Control of Variable Phase-Pole Induction Machines in the Context of Magnetic Pole Transition

---

By Mesfin Tilahune Tessema

Supervisor

Mengesha Mamo (Ph.D.)
Addis Ababa University,
College of Engineering and Environmental Built,
Addis Ababa,
Ethiopia

Supervisor

Luca Peretti (Ph.D.)
KTH Royal Institute of Technology,
Stockholm,
Sweden

Approved by Examining Committee

Dean, School of Graduate Studies	Signature	Date
Sosina Mengistu (Ph.D.)		
Advisor-1		
Mengesha Mamo (Ph.D.)		
Advisor-2		
Luca Peretti (Ph.D.)		
Internal Examiner		
Dereje Shiferaw (Ph.D.)		
External Examiner		
Ayman Samy Abdel-Khalik (Prof.)		

Declaration

This Ph.D. dissertation is a presentation of my work and any material used from other sources has been clearly identified and properly acknowledged and cited.

Acknowledgments

The special and adventurous journey of my Ph.D. project has been completed. I would like here to acknowledge all the great people who helped and supported me during all these years. First, I would like to thank my supervisors, Dr. Mengesha Mamo from Addis Ababa Institute of Technology and Dr. Luca Peretti from KTH Royal Institute of Technology, and for their valuable guidance, inspiration, and encouragement during all these years.

During my five-year Ph.D. journey, I had the privilege of collaborating with many outstanding individuals. I would like to express heartfelt thanks to the late Prof. Oskar Wallmark for his invaluable insights and to Dr. Mats Leksell for his ongoing encouragement and inspiration. I am particularly grateful to Gustaf Falk Olson and Yixuan Wu for their steadfast commitment to building the WICSC experimental setup and for their complete support in every aspect during my tenure at KTH Royal Institute of Technology in Stockholm, Sweden. Additionally, I extend my gratitude to the entire EMD (Multiphase) team, especially Omer Ikram Ul Haq, for his assistance with experimental measurements at the ABB research center in Västerås, Sweden.

I would like to express my heartfelt appreciation to all my friends in Ethiopia and Sweden for their unwavering support and the cherished moments we have shared. Special thanks to Kirubel Eshetu, Nebiyu Tenaye, Teshome Hambissa, Nebiyu Yonas, Abebe Teklu, Yonas Yehualashet, Natan Tadesse, Demlash Yibeltal, Sisay Tsegaye, Zelalem Mengistu, Fikremariam Yehualashet and Antenhe Tamiru for their generosity, motivation, and treasured memories. My deepest gratitude goes out to my friends, whose steadfast encouragement has been invaluable throughout this journey. Your companionship, empathy, and constant motivation have provided strength during difficult times. Thank you for the numerous discussions, shared laughter, and moments of relief that have made this journey not only bearable but truly unforgettable. Your belief in me has been a driving force and I am forever grateful for your friendship.

Special thanks to the Swedish International Development Agency (SIDA) for providing the financial support necessary to conduct this research. Without their generous funding, this project would not have been possible.

My heartfelt appreciation is extended to my parents, Wolansa Kebede and Tilahune Tessema, as well as to my sisters Bezunesh Chere, Tigist Tilahune, and Addisalem Tilahune, for their continual love and encouragement through the years. I am profoundly thankful to my beloved son, Yanis Mesfin, to Yanis's mother, Netsanet Tadesse, and my nephew Nathaneal Demlash. Your unwavering love, patience, and understanding have been pillars of support and motivation throughout this journey. Your boundless curiosity and energy have taught me the virtues of perseverance and enthusiasm. Thank you for being my source of inspiration, bringing joy and balance to my life. This accomplishment is as much yours as it is mine.

“Plough deep while sluggards sleep,
and you shall have corn to sell and keep.”

— Benjamin Franklin (book: Poor Richard’s Almanack (1736))

Abstract

The importance of transitioning from fossil fuel cars to electric vehicles is a critical step in the global initiative to mitigate the impacts of climate change. As electric vehicles become a central element of sustainable transportation systems, countries worldwide, including Ethiopia, are working to achieve their carbon reduction goals. One of the primary reasons for this shift is the absence of tailpipe emissions from EVs, unlike traditional internal combustion engine vehicles, which release substantial amounts of carbon dioxide CO_2 and other harmful pollutants into the environment. Hence, replacing conventional cars with electric ones significantly reduces greenhouse gas emissions, which are a major contributor to global warming.

The first part of this dissertation focuses on the necessity of accurately estimating electrical parameters for multiphase machines to be used in advanced control approaches. This necessity is especially pertinent for the special subclass of multiphase machines identified as Variable Phase-Pole Induction Machines (VPPIMs). This part of the research explores, calculates, and experimentally confirms various parameter estimation techniques for a wound stator coil induction machine with independent slot current control capable of dynamically adjusting the phase-pole configuration in real time. The parameter estimation techniques covered are a traditional finite element analysis-based stator impedance calculation and an application of the finite element-based harmonic plane decomposition (HPD) method. Experimental validation demonstrates the proposed estimation methods across different machine configurations. When comparing the two methods, parameter estimation based on HPD theory aligns closely with practical outcomes. The classical method results in a 22% relative error for the magnetizing inductance (L_M) and a 62% overestimation for the leakage inductance (L_σ) in the 3-phase/2-pole VPPIM compared to measurements. The HPD approach reduces these errors to 15% for magnetizing inductance and 36% for leakage inductance. The conventional approach yields a 17% rate for the magnetizing inductance L_M, which decreases to 6% with the HPD method. Similarly, for the leakage inductance (L_σ), the rate of 54% is reduced to 23% in the 9-phase/2-pole VPPIM configuration. Additionally, the HPD model cuts computing time to one-eighth of the conventional methods, significantly enhancing computational efficiency.

The latter portion of this research concentrates on variable phase-pole induction machines, which show potential for electromobility applications because of their ability to electronically modify the number of magnetic poles during operation, consequently enhancing the machine's torque-speed performance. This research introduces a model reference adaptive system approach for the sensorless speed operation of a nine-phase variable phase-pole induction machine. The same adaptive full-order observer estimates mechanical speed in two distinct ways, each corresponding to a different pole-pair configuration of interest. Sensorless drive operation is sustained during pole-pair configuration transitions through an appropriate switch between the two speed-estimation strategies, ensuring accurate rotor flux linkage information for high-performance control. The proposed method's simulation and experimental outcomes strongly correlate, affirming the sensorless methodology's effectiveness under variable load scenarios and during positive/negative speed transitions.

Keywords: *Electric drives, Electrical machine, Multiphase drive, Pole-phase changing, State-space model, Speed control, Sensorless control.*

Contents

*

List of Figures

List of Tables

Acronyms

AI	**A**rtificial Intelligence
CH_4	**M**ethane
CO_2	**C**arbon Dioxide
DNN	**D**eep Neural Network
DSP	**D**igital Signal Processor
DTC	**D**irect Torque Control
DTCIM	**D**irect Torque Control of Induction Motor
EHV	**E**lectric Hybrid Vehicle
EKF	**E**xtended Kalman Filter
EV	**E**lectric Vehicle
FEA	**F**inite Element Analysis
FEM	**F**inite Element Method
FPGA	**F**ield-Programmable Gate Array
FW	**F**ield Weakening
HPD	**H**armonic Plane Decomposition
IFOC	**I**ndirect Field-Oriented Control
IGBT	**I**nsulated Gate Bipolar Transistor
IM	**I**nduction Machine
IPM	**I**nterior-Permanent Magnet
ISCAD	**I**ntelligent Stator Cage Drive
ML	**M**achine Learning
MMF	**M**agnetomotive Force
MPC	**M**odel Predictive Control
MRAS	**M**odel Reference Adaptive System
MTPA	**M**aximum Torque per Ampere
N_2O	**N**itrous Oxide
NOAA	**N**ational Oceanic and Atmospheric Administration
PPC	**P**hase Pole Configuration
ppm	**p**arts per million
PSO	**P**article Swarm Optimization
PWM	**P**ulse Width Modulation
SDG	**S**ustainable Development Goal
SVM	**S**pace Vector Modulation
SVPWM	**S**pace Vector Pulse Width Modulation
THD	**T**otal Harmonic Distortion
VPPIM	**V**ariable Phase Pole Induction Machines
VSD	**V**ector Space Decomposition
WLTP	**W**orldwide harmonized light vehicles test procedure
WICSC	**W**ound Independently-Controlled Stator Coils

Nomenclature

A_z	**M**agnetic vector potential, z component
B	**M**agnetic flux density
B_r	**R**adial component of the magnetic flux density
B_φ	**T**angential component of the magnetic flux density
B_φ^*	**C**omplex conjugate of the axial magnetic field
C	**F**lux coupling matrix
$C_{s,lam}$	**S**tator lamination stacking factor
c_s	**S**tator winding connection factor
dF	**F**orce on the differential volume dv
dq	**D**ifferential charge element
dT_e	**D**ifferential torque
$d\theta_m$	**D**ifferential angular displacement
e_z	**T**he unit vector in the z direction
$F_{r,1}$	**M**agneto-motive force in the air gap due to the rotor current
$F_{s,1}$	**M**agneto-motive force in the air gap due to the stator current
J_z	**C**urrent density
k_1	**F**undamental winding factor
L_M	**M**agnetizing inductance (inverse-Γ model)
μ	**M**agnetic permeability
q_s	**S**lots per pole per phase
R_r'	**R**otor resistance referred to the stator side
r	**P**osition vector
r_r	**M**agneto-motive force in the air gap due to the rotor current
$r_{s,in}$	**M**agneto-motive force in the air gap due to the rotor current
σ	**E**lectric conductivity
T_e	**E**lectromagnetic torque
T_s^*	**S**ampling time
v	**V**elocity vector field
$v_{s,k}$	**C**oil voltage
$v_{z,k}$	**C**onverter voltage
V_{pot}	**E**lectrical scalar potential
ω_m	**M**echanical speed
ω_s	**S**lip frequency
ζ	**P**hase-lag angle between the stator and the induced rotor bar currents
$\phi^s_{\delta,k}$	**S**tator coils flux
$\phi^r_{\delta,k'}$	**R**otor bar flux
θ_r	**R**otor angle
$\hat{\omega}_{sl}$	**E**stimated Slip Angular Frequency
$\hat{\theta}_R^{(h)}$	**E**stimated Rotor Flux Angle at the h^{th} Harmonic Plane
D	**E**lectric displacement field

ρ	**C**harge density
$A^{(h)}$	**S**tate Matrix of the h^{th} Harmonic Plane
B	**I**nput Matrix
$C^{(h)}$	**O**utput Matrix of the h^{th} Harmonic Plane
$\psi^{*(h)}_{R,\alpha\beta}$	**C**omplex Conjugate Rotor Flux of the h^{th} Harmonic Plane
$e^{(h)}_{is,\alpha}, e^{(h)}_{is,\beta}$	α- and β-Component Stator Current Error of the h^{th} Harmonic Plane
$\hat{A}^{(h)}$	**E**stimated State Matrix of the h^{th} Harmonic Plane
$\hat{x}$	**E**stimated State Variables
$\hat{\omega}_r$	**E**stimated Rotor Angular Speed
$\hat{\omega}_{sl}$	**E**stimated Angular Slip Frequency
$\hat{\psi}_r$	**E**stimated Rotor Flux
$\hat{\psi}_s$	**E**stimated Stator Flux
h	**H**armonic plane order, $h \in 1,3,5,\ldots,\zeta$
$i^{(h)}_{s,\alpha}, i^{(h)}_{s,\beta}$	α- and β-Component Stator Current of the h^{th} Harmonic Plane
$K^{(h)}$	**O**bserver Gain Matrix of the h^{th} Harmonic Plane
L_m	**M**agnetizing Inductance
$L^{(h)}_M$	**M**agnetizing Inductance of the h^{th} Harmonic Plane
L_r	**R**otor Self Inductance
L_s	**S**tator Self Inductance
$L^{(h)}_\sigma$	**L**eakage Inductance of the h^{th} Harmonic Plane
m	**N**umber of Phases
$p^{(h)}$	**P**ole Pairs of the h^{th} Harmonic Plane
R_r	**R**otor Resistor
$R^{(h)}_R$	**R**otor Resistance of the h^{th} Harmonic Plane
R_s	**S**tator Resistor
τ_e	**E**lectromagnetic Torque
τ^*	**R**eference Torque
$v^{(h)}_{s,\alpha}, v^{(h)}_{s,\beta}$	α- and β-Component Stator Voltages of the h^{th} Harmonic Plane
ω_r	**R**otor Angular Speed
ω^*_r	**R**eference Rotor Angular Speed
$\omega^{(1,3)}_r$	**E**stimated Rotor Speed within the Combined First and Third Harmonic Planes
ω_s	**S**tator Angular Speed
$\psi^{(h)}_{R,\alpha}, \psi^{(h)}_{R,\beta}$	α- and β-Component Rotor Flux of the h^{th} Harmonic Plane
$\psi^{(h)}_{R,\alpha\beta}$	$\alpha\beta$-Component Rotor Flux of the h^{th} Harmonic Plane
$\psi^{(h)}_{s,\alpha}, \psi^{(h)}_{s,\beta}$	α- and β-Component Stator Flux of the h^{th} Harmonic Plane
$\psi^{(h)}_{s,\alpha\beta}$	$\alpha\beta$-Component Stator Flux of the h^{th} Harmonic Plane
σ	**L**eakage coefficient
$\sigma^{(h)}$	**L**eakage coefficient of the h^{th} Harmonic Plane
K_d	**W**inding factor, diagonal matrix

1 Introduction

1.1 Background

In recent times, there has been worldwide recognition of the difficulties posed by global warming. This problem comes from the "greenhouse effect", which is driven by the presence of CO_2 and other gases such as CH_4 in the atmosphere. These gases capture the Sun's infrared radiation reflected from the ground, holding energy in the atmosphere and raising the temperature. The increase in the Earth's temperature results in considerable ecological harm to ecosystems, leading to natural disasters that influence human populations. One of the effects of this, according to NOAA, has been the recent landslides in Ethiopia, which have killed more than 200 people. Based on a recent publication by the NOAA, the average global surface temperature in July 2024 was 2.18 ($^{\circ}F$) higher than the mean of 60.4 ($^{\circ}F$). This set a new record as the hottest July and marked it as the month with the second lowest extent of sea ice in the 175-year global record of NOAA, as illustrated in Figure 1.1. Although the economic slowdown triggered by the coronavirus pandemic was significant, the concentrations of the two main human-caused greenhouse gases, carbon dioxide and methane, continued to increase without interruption in 2020 [1].

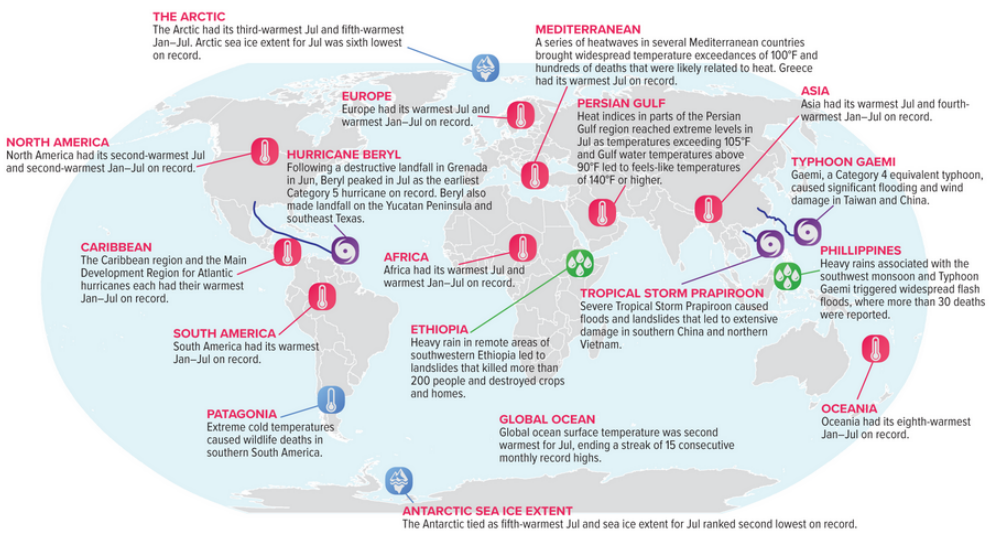

Figure 1.1: Significant climate anomalies and events (Image credit: NOAA)

Furthermore, the Global Monitoring Laboratory accurately measures the three main greenhouse gases: CO_2, CH_4, and N_2O, from four separate monitoring stations. In 2020, the global average surface concentration of carbon dioxide reached 412.5 ppm, increasing by 2.6 ppm over the year. This rise marks the fifth-highest rate of change in the 63-year history of NOAA. Figure 1.2, depicts the average global atmospheric carbon dioxide burden, based on data gathered by the NOAA global greenhouse gas reference network [1]. The figure illustrates that predictions for 2030 foresee a persistent increase in CO_2 emissions. The increased focus on climate change and the reduction of harmful emissions in the atmosphere has generated interest in environmentally friendly

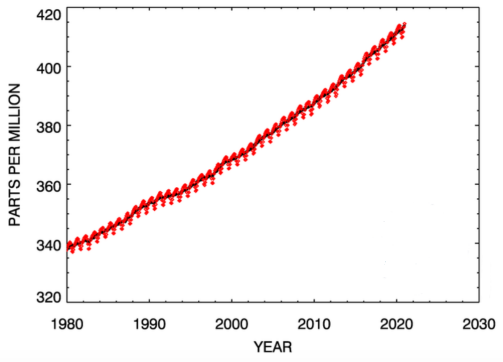

Figure 1.2: Global monthly mean of CO_2

modes of transportation. This interest has spurred significant advancements in areas such as electric ship propulsion, more electric aircraft, electric and hybrid road vehicles, and electric locomotive traction [1], [2].

One strategy for reducing CO_2 emissions is to substitute gasoline-powered cars with EVs. Multiphase electric machines are gaining recognition as up-and-coming candidates for electric vehicle applications and have emerged as a fascinating topic within electric drive research.

1.1.1 Construction of the VPPIM

A subcategory of multiphase machines, known as Variable Phase-Pole Induction Machines (VPPIMs), is gaining attention in applications requiring extensive torque-speed operating ranges, such as electromobility. An illustration of a special VPPIM with individual stator slot coils wound on the external part of the stator [3], is shown in Figure 1.3. Other types of VPPIMs with more conventional windings are possible [4]. The fundamental feature of VPPIMs is their ability to change the number of phases and magnetic poles in real time, thereby extending their operational range [5]. Nevertheless, the dynamic behavior of these machines during a magnetic pole transition presents challenges for adequate control.

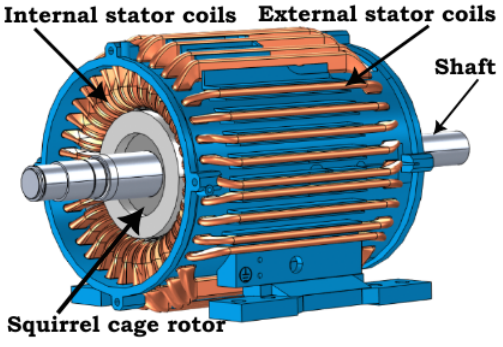

Figure 1.3: Variable Phase-Pole Induction Machine

VPPIMs are awakening interest in those applications where sizeable torque-speed operating areas are in demand, like electromobility. The essence of VPPIMs lies in the capability of altering the magnetic pole number in real time to increase their operational range. However, the dynamic nature of these machines during a magnetic pole change poses challenges to effective control, particularly when speed sensors are not used. Studies on sensorless-based speed control for VPPIMs are essentially non-existent. However, based on the modeling and control approach established in [5], it is possible that conventional model-based sensorless approaches could be extended to the VPPIM case with reasonable modifications.

1.1.2 The space harmonics in multiphase machines

One intriguing technical feature of multiphase machines is the geometric distribution of their MMF compared to traditional three-phase machines. The MMF geometric distribution around the air gap generates space harmonics when coupled with time harmonics from sinusoidal or non-sinusoidal input voltages/currents at the machine terminals. These space harmonics impact the geometric distribution of the flux linkage, which in turn influences torque. The equation:

$$\nu = p(q - 2km) \tag{1.1}$$

where ν denotes the frequency of a space harmonic, which refers to variations in the magnetic field pattern around the stator. These variations depend on the number of phases and the number of poles in the machine. p signifies the number of pole pairs in the machine, a factor linked to the design, impacting how the magnetic field engages with the rotor. q is the time-harmonic index, denoting the frequency component of the waveform of the input current or voltage. To illustrate, $q = 1$ indicates the fundamental frequency, while larger q values represent higher-order harmonics (for instance, $q = 2$ for the second harmonic), m represents the number of phases in the machine, k is an integer which can be 0, ±1, ±2, ..., indicating the relational multipliers between time and space harmonics for a given machine setup [6]. The equation $\nu = p(q - 2km)$ offers a link between the space harmonic frequency (ν) and the time-harmonic frequency (q), implying:

- For every time-harmonic associated with a particular q value, there are several related space harmonics. The frequencies of these space harmonics are influenced by the number of phases (m) and the number of pole pairs (p).
- The term $2km$ in the equation accounts for the fact that the space harmonics are not necessarily directly aligned with the time harmonics. They are spaced according to a function of both the number of phases m and an integer k, which allows for multiple space harmonics corresponding to the same time harmonic.
- The spatial harmonics produced will change depending on the value of k, indicating that for each q, multiple space harmonics exist with frequencies that are influenced by the various values of k.

Understanding the formation of space harmonics concerning q and m is crucial for multiphase machines because:

- Space harmonics impact the magnetic field configuration in the air gap, consequently affecting the machine's torque generation, efficiency, and noise features.
- The number of phases (m) has a direct effect on the quantity of space harmonics produced per time harmonic. An increase in the number of phases, such as in machines with 5 or 7 phases, usually results in a more complex yet smoother MMF distribution.
- The number of pole pairs (p) is crucial for establishing the exact frequency of space harmonics. The pole count affects both the synchronous speed of the machine and the frequency at which the magnetic field revolves around the stator.

In the fundamental time-harmonic scenario where ($q = 1$), examined the impact of fully pitched windings, those that extend over the entire pole pitch of the machine. Here, harmonic generation is observed without incorporating specific winding skew or other alterations. Fully pitched windings generally produce a straightforward, symmetric MMF pattern, reducing distortions in the space harmonic generation. This occurs because no intentional shifts in the winding setup are made to mitigate harmonics or enhance field distribution. Figure 1.4 provides a 3D representation of the time and space harmonics in multiphase machines.

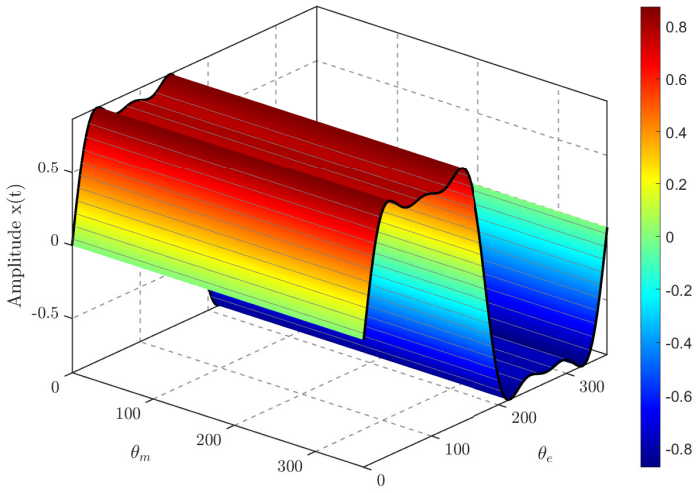

Figure 1.4: 3D Space Harmonic Visualization (p = 1 pole pairs)

1.1.3 Transformation of the multiphase machines

The Vector Space Decomposition (VSD) theory, which is used to model and control multiphase machines, is exemplified with two different phase configurations. First, a 3-phase machine to represented in the VSD model one vector space which is the fundamental and the homopolar axis are present as seen in (1.2).

$$\boldsymbol{VSD}_{m=3} = \frac{2}{3}\begin{bmatrix} 1 & \cos(\theta) & \cos(2\theta) \\ 0 & \sin(\theta) & \sin(2\theta) \\ 1 & 1 & 1 \end{bmatrix} \tag{1.2}$$

where $\theta = \frac{2\pi}{3}$,
Second in 6-phase machines, three vector spaces are present: the fundamental, the third, and the fifth vector space as described in (1.3).

$$\boldsymbol{VSD}_{m=6} = \frac{1}{3}\begin{bmatrix} 1 & \cos(\theta) & \cos(2\theta) & \cos(3\theta) & \cos(4\theta) & \cos(5\theta) \\ 0 & \sin(\theta) & \sin(2\theta) & \sin(3\theta) & \sin(4\theta) & \sin(5\theta) \\ 1 & \cos(3\theta) & \cos(6\theta) & \cos(9\theta) & \cos(12\theta) & \cos(15\theta) \\ 0 & \sin(3\theta) & \sin(6\theta) & \sin(9\theta) & \sin(12\theta) & \sin(15\theta) \\ 1 & \cos(5\theta) & \cos(10\theta) & \cos(15\theta) & \cos(20\theta) & \cos(25\theta) \\ 0 & \sin(5\theta) & \sin(10\theta) & \sin(15\theta) & \sin(20\theta) & \sin(25\theta) \end{bmatrix} \tag{1.3}$$

where $\theta = \frac{\pi}{3}$,
The above two equations show an inconsistent number of vector spaces presented in phase-changing mode.

The VSD encounters difficulties managing currents within neighboring slots of the same phase belt, especially during PPC transitions. To mitigate this, a generalized VSD approach called HPD was proposed in [5]. This method defines a fixed number of subspaces, equating to a predetermined number of current controllers. Unlike conventional VSD models, this approach preserves model consistency regardless of the PPC, thus solving the continuity problem linked with VSD-based modeling across various PPCs. The HPD accomplishes this by separating all possible magnetic pole numbers. For a VPPIM with stator space Q_s with independent coil excitation, the number of subspaces is $Q_s/2$, based solely on Q_s. Each harmonic plane in the HPD, similar to

the VSD, is independently represented by a lumped parameter model, such as the inverse-Γ or T-equivalent model. In particular, the parameters of VSD and HPD are interrelated, as detailed in [7]. All odd harmonics of the base case are present since HPD is a DFT of the slot variables, and the fundamental reference frame unifies the magnetic axes for the VSD as described in the following equations.

$$\underline{X}_{\alpha\beta,h} = \frac{4}{Q_s} \sum_{k=0}^{Q_s/2-1} x_{k+1} e^{\left(\frac{j2\pi kh}{Q_s}\right)} = \frac{4}{Q_s} \sum_{k=-Q_s/2}^{-1} x_{k+1} e^{\left(\frac{j2\pi kh}{Q_s}\right)} \tag{1.4}$$

$$\underline{X}_{\alpha\beta,h} = \frac{2}{Q_s} \sum_{k=-Q_s/2}^{Q_s/2-1} x_{k+1} e^{\left(\frac{j2\pi kh}{Q_s}\right)} \tag{1.5}$$

Depending on the pole number, each phase-pole configuration is assigned to one base case. Multiple base cases, i.e., odd and even, are needed to cover all phase-pole configurations. Matrix repetition is also required to maintain dimensionality. The transformation of the space-vector quantities from the fundamental 123 reference frame [8] to the stationary $\alpha\beta 0$ reference frame is as follows:

$$\mathbf{x}_{\alpha\beta} = \underbrace{\left(\frac{2}{m_{b,o}}\right)^{K} \mathbf{K}_d \mathbf{C}}_{\mathbf{T}_{123\to\alpha\beta}} \cdot \mathbf{x}_{123} \tag{1.6}$$

$$\mathbf{x}_{123} = \underbrace{\left(\frac{2}{m_{b,o}}\right)^{1-K} \mathbf{C}^{\mathrm{T}} \mathbf{K}_d}_{\mathbf{T}_{\alpha\beta\to 123}} \cdot \mathbf{x}_{\alpha\beta} \tag{1.7}$$

$$\mathbf{C} = \begin{bmatrix} 1 & \cos(\delta) & \cos(2\delta) & \dots & \cos((m-1)\delta) \\ 0 & \sin(\delta) & \sin(2\delta) & \dots & \sin((m-1)\delta) \\ 1 & \cos(3\delta) & \cos(6\delta) & \dots & \cos((m-1)3\delta) \\ 0 & \sin(3\delta) & \sin(6\delta) & \dots & \sin((m-1)3\delta) \\ \vdots & \vdots & \vdots & \ddots & \vdots \\ 1 & \cos(\xi\delta) & \cos(2\xi\delta) & \dots & \cos((m-1)\xi\delta) \\ 0 & \sin(\xi\delta) & \sin(2\xi\delta) & \dots & \sin((m-1)\xi\delta) \end{bmatrix}$$

Where,

$$\delta = \frac{\pi}{m}$$

Assuming half-wave symmetry, which is given by the windings. Therefore, only half of all slots are taken for the transformation, limiting the frequency resolution and considering only the odd harmonics. However, it needs to be incorporated into the even base cases as well. So the solution is to discard the assumption of half-wave symmetry and take all slots into account for Clarke transformation using only mechanical angles.

$$x_{\alpha\beta,h} = \frac{2}{Q_s} \sum_{k=0}^{Q_s-1} x_{k+1}\, e^{j\left(\frac{2\pi k}{Q_s} h\right)} \tag{1.8}$$

In contrast to the traditional $\alpha\beta 0$ and $dq0$ transformation theories used for three-phase machines, the VSD approach necessitates an extra intermediary reference frame, referred to as the "fundamental winding configuration." Beyond this, the rest of the transformation method mirrors that used in three-phase machines, with the exception that the matrices utilized in the computations are m-by-m, not three-by-three. Figure 1.5 illustrates the transformational flow of the VSD concept to derive variables in a rotating reference frame, where

x represents a generic vector corresponding to any machine variable, such as current or voltage vectors.

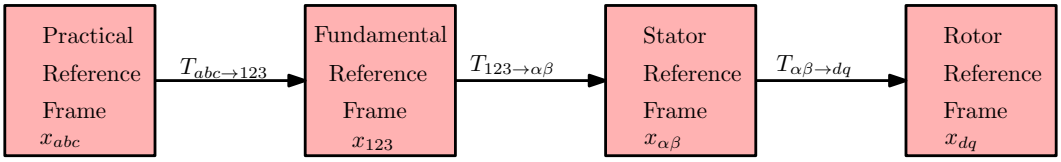

Figure 1.5: Transformation chain in the Vector Space Decomposition approach.

1.1.4 Phase-Pole Modulation in the VPPIM

There is a trade-off between phase and pole configurations in the operation of electrical machines. Machines with more phases offer greater fault tolerance, enhancing reliability. Increasing the number of poles results in higher maximum torque but reduces maximum speed. When selecting the maximum phase number, it is essential to consider the given pole number. However, not every phase-pole arrangement is practical or beneficial in real-world applications. Phase belts with only one slot are particularly noteworthy for their unique characteristics. As illustrated in Figure 1.6, the relationship between the mechanical speed and torque for two different sets of parameters: (m_1, p_1) and (m_2, p_2).

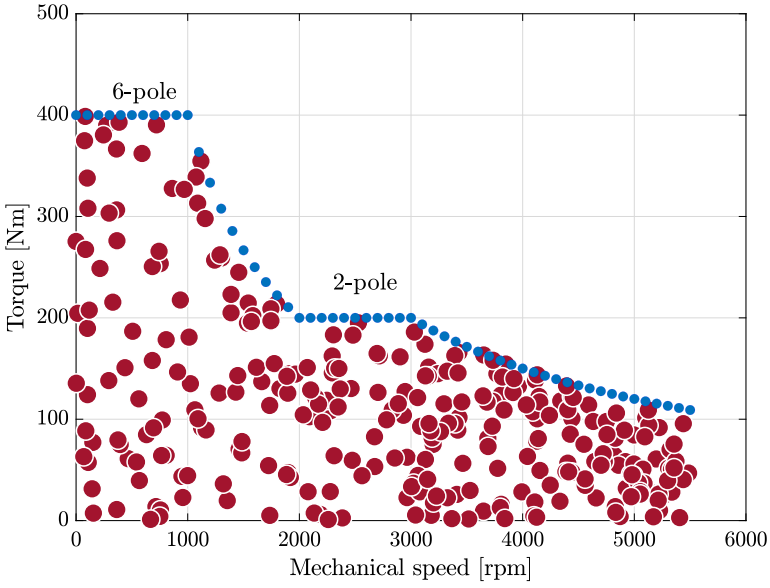

Figure 1.6: Torque-Speed envelope.

The concept of pole changing extends the torque-speed envelope to the right. This means that by adjusting the pole number, the machine can achieve higher speeds while maintaining adequate torque. This flexibility allows for a broader range of operating conditions, making the machine more versatile and adaptable to various applications. By strategically changing the pole number, one can optimize the machine's performance for both low-speed, high-torque scenarios and high-speed, lower-torque scenarios, thereby enhancing the overall efficiency and effectiveness of the system.

This dissertation examines and leverages the benefits of using VPPIM to mitigate the greenhouse effect, proposing its application in the electromobility sector.

1.2 General Objective

The primary objective of this dissertation is to analyze the VPPIM model through the application of the finite element method, evaluate its performance using advanced numerical methods, and compare it with conventional analytical techniques. Additionally, the research employs the HPD modeling approach to explore effective parameter estimation strategies for the VPPIM drive, highlighting its ability to adjust phase and poles during real-time operation. The study also develops a sensorless MRAS-based speed control system tailored to the unique characteristics of the VPPIM, with a focus on reliable speed estimation methods that have been validated through experimental testing.

1.2.1 Specific Objectives

- The VPPIM model is analyzed using the finite element approach, and its effectiveness is thoroughly assessed through sophisticated numerical methods.
- Finding suitable methods for parameter estimation for the VPPIM drive, focusing on the drive's ability to change the phase and magnetic pole during real-time operation.
- The creation of a sensorless MRAS-based speed control method for the VPPIM drive which was verified through experimental testing and focused on the machine's special features and speed estimation techniques.
- Enhancing estimation accuracy in the presence of parameter mismatches and load torque disturbances.
- Combining sensorless control and parameter estimation to guarantee real-time flexibility in changing circumstances.
- Creating a closed-loop sensorless control system for multiphase IM drives, such as Field-Oriented Control.

1.3 Problem Statement

According to data reviewed by Darwin Motion, a manufacturer of variable-speed drives, the global implementation of these drives results in substantial energy savings. Specifically, it is estimated that their use leads to annual energy savings exceeding 115 million megawatt hours. This significant figure underscores the potential for variable-speed drives to reduce global energy consumption and improve energy efficiency. Nevertheless, the data also reveals a recurring problem: less than 10% of motors used globally have variable-speed drives installed, despite these encouraging advantages. This suggests that there is a great deal of unrealized potential for increasing energy efficiency by using variable-speed drive technology more widely [9].

Sustainable Development Goal seven of the UN seeks to guarantee everyone access to modern, reasonably priced, dependable, and sustainable energy by 2030, making this difficulty especially pertinent. Doubling the rate of global gains in energy efficiency is one of the main objectives of this aim. Since variable-speed drives may improve energy utilization, eliminate waste, and lower operating costs, their incorporation into industrial applications is essential to achieving this goal. Given that only a small portion of motors now employ variable-speed drives, there is a big chance to accelerate the achievement of these international energy efficiency targets.

Furthermore, variable-speed drive technology is a promising candidate for applications in the quickly expanding field of electromobility due to the advantages of increasing power efficiency. EVs and other electromobility technologies mainly depend on effective power conversion systems to improve performance, lower energy consumption, and prolong battery life. VPPIMs are perfect for increasing the energy efficiency of EVs and other electric-powered systems because of their adaptability to a variety of electromobility applications, which include their capacity to support a broad range of phase-pole configurations. Provided a multitude of phase-pole configurations:

- How can a set number of controllers regulate the currents in each stator coil while preserving the dynamic characteristics?
- How can the parameters of the VPPIM be precisely estimated using harmonic plane decomposition and finite element methods?
- How can the VPPIM drive's sensorless speed control be implemented in several harmonic planes?

1.4 Original Contributions

The original contributions of this dissertation are listed as follows:

- The HPD parameter estimate method for the VPPIM, which has not yet been empirically verified in practical applications, is extensively examined in this dissertation. This approach's efficacy in precisely estimating important VPPIM characteristics, including inductance, resistance, and flux linkage, under various operating situations is examined and contrasted with other well-established analytical and numerical techniques. The study intends to evaluate the HPD method's potential benefits, such as its accuracy, computing efficiency, and adaptability to the dynamic characteristics of the VPPIM, by comparing it with alternative parameter estimate strategies. The thesis also highlights the HPD method's shortcomings and recommends areas for additional study or development, which advances our knowledge of its usefulness in sophisticated motor control systems.
- The dissertation focuses on experimentally validating the improved torque-speed profile from the magnetic pole change in a VPPIM to create an adaptive flux and speed observer in a sensorless system. Sensorless control schemes are a well-established topic in the scientific literature. However, their application to multiphase machines represents a novel area of research, as evidenced by the limited number of publications on the subject. The extension of the algorithms to multiphase machines is not merely a matter of applying the algorithms already known to machines with many phases that are a multiple of three. Rather, it takes advantage of the degrees of freedom available by this technology to enhance the performance of the drive and its reliability. Additionally, no prior studies have investigated sensorless speed control for Variable Phase-Pole Induction Machines. This research delves into this approach by integrating it with the Harmonic Plane Decomposition method. Without the HPD model, achieving speed sensorless operation with the same performance would not be possible. Thus, this work represents a relevant scientific advancement.

1.5 Outline of the Dissertation

The format of this doctoral dissertation is a collection of works. The thorough scientific contributions are described in detail in the included publications. The purpose of the following chapters is to give an overview of the appended papers and highlight the main ideas and important discoveries.
The dissertation's writing is structured as follows:
Chapter 2 explores the most recent developments in the literature about VPPIM's modeling, parameter estimation, and sensorless control. It gives a thorough overview of the many modeling approaches—including steady-state and transient analysis—that have been developed to accurately represent the behavior of VPPIMs under different operational conditions. To ensure correct motor performance in real-world applications—especially when coping with uncertainties and fluctuating load conditions—the chapter also examines parameter estimate approaches.
Chapter 3 gives a thorough analysis of FEA, a computer technique used to solve complex physical problems by breaking the problem domain down into smaller components. This method makes it easier to approximate the behavior of the system. In order to comprehend and model the machine's mechanical and electromagnetic characteristics under various operating conditions, VPPIM relies heavily on FEA. To ensure accurate and reliable results, the finite element modeling for VPPIM includes a number of crucial procedures and considerations.
Chapter 4 investigates the use of FEM for VPPIM parameter estimation, emphasizing both the theoretical approach and its experimental support. Key characteristics that characterize the machine's behavior under different operating situations, including inductances, resistances, and magnetic flux couplings, are derived in this chapter using the FEM approach. To acquire accurate and trustworthy estimates of these electrical and magnetic parameters—which are essential for precise machine modeling and performance prediction—the chapter describes how FEM simulations are combined with parameter estimation approaches.
Chapter 5 An important advancement in the realm of sophisticated motor control approaches is examined in this section: the implementation of a sensorless speed control strategy for the VPPIM based on a Model Reference Adaptive System. Physical speed sensors, which are commonly employed in traditional motor control systems but can introduce complexity, expense, and maintenance concerns, are not necessary for speed estimates when using the MRAS technique. The MRAS algorithm continuously adjusts to deliver precise speed estimations by using a reference model that replicates the intended behavior of the VPPIM under various operating situations and compares it with the actual motor performance.
Chapter 6 Key findings about the VPPIM's performance and potential, control strategies, and methods are derived from the thorough analysis and experimental results provided in this chapter. The chapter shows how well the MRAS-based sensorless speed control works to improve the operational efficiency and flexibility of the VPPIM, and it also emphasizes how well FEM estimates the machine's parameters. The importance of parameter estimation and sensorless control methods in overcoming typical obstacles like expense, intricacy, and dependence on physical sensors is also emphasized, making the VPPIM a strong contender for cutting-edge applications like electric traction and electromobility in general.

1.6 List of Appended Publications

This dissertation is based on the papers listed below:

I ***"Validation of FEM-Based Parameter Estimation for Variable Phase-Pole Induction Machines."*** **Mesfin Tilahune**, Gustaf Falk Olson, Luca Peretti, and Mengesha Mamo, in IEEE Transactions on Energy Conversion, vol. 38, no. 4, pp. 2310-2317, Dec. 2023, DOI: 10.1109/TEC.2023.3272950

II ***"Speed-Sensorless Control of Pole Transition for Variable Phase-Pole Induction Machines."*** - **Mesfin Tilahune**, Luca Vancini, Omer Ikram ul Haq, Michele Mengoni, Luca Peretti, Mengesha Mamo *IEEE Transactions on Energy Conversion,* DOI: 10.1109/TEC.2025.3571996

III ***"Performance Analysis of Variable Phase-Pole Induction Machine for Electric Traction Application: Finite Element Method."*** **Mesfin Tilahune**, Luca Peretti, Mengesha Mamo, 2023 IEEE AFRICON, Nairobi, Kenya, 2023, pp. 1-6, DOI: 10.1109/AFRICON55910.2023.10293402

IV ***"Experimental Evaluation in the Design of MRAS-Based Speed Estimator for Variable Pole Induction Machines: Reference Frame Selection."*** **Mesfin Tilahune**, Luca Vancini, Omer Ikram ul Haq, Michele Mengoni, Luca Peretti, Mengesha Mamo *European Conference on Power Electronics and Applications,* DOI : 10.34746/epe2025-0338

2 Literature Review

2.1 Background

Since the late 1990s, various studies have emphasized the advantages of multiphase machines over traditional three-phase machines, particularly in their modeling, parameter estimation, and control. One can look at the trend in publication counts over time in IEEE to assess interest in multiphase drives, as shown in Figure 2.1.

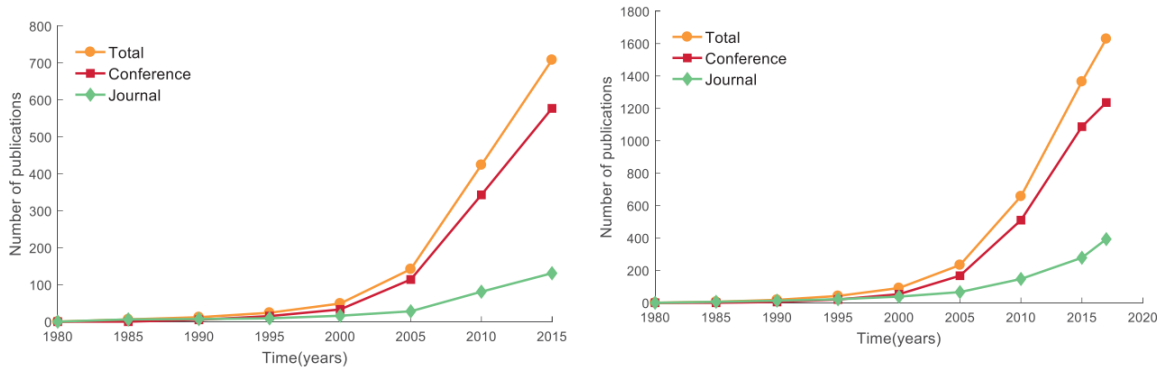

Figure 2.1: Evolution of multiphase electric drives in IEEE database.

A straightforward search in IEEE Xplore illustrates the progression of conference and journal publication counts as depicted. The early twentieth century marked the onset of a significant surge in research publications in this domain. Moreover, as shown in the figure above, the total number of publications increased twofold during the five years from 2015 to 2020.

2.2 Recent Developments in Modeling of the Multiphase Machines

Recent progress in multiphase machine modeling has been driven by the need for more reliable, efficient, and fault-tolerant systems in various fields such as electric vehicles, renewable energy, and industrial drives. Compared to conventional three-phase machines, machines with five or more phases have several advantages, such as increased power density, decreased torque ripple, and improved fault tolerance. These characteristics provide efficiency and dependability, making them perfect for applications that need to run continuously even in the case of a phase failure. Recent attempts to improve fault condition modeling have been prompted by the remarkable advantages that multiphase machines provide for fault-tolerant applications. Maintaining system functionality during faults requires efficient fault detection, diagnosis, and recovery techniques such as phase reconfiguration. According to [10], these developments are especially important in sectors that place a high value on operational uptime and reliability, such as electric vehicles and renewable energy solutions.

Comprehending the intricate electromagnetic interactions between the stator and rotor components is essential to building models for multiphase machines. This involves computing flux linkages for each phase, which are frequently coupled, and generating equations for both voltage and current. The distribution of flux and current in such devices is widely analyzed using space vector models, which offer lucid insights into the behavior of the system under various operating conditions. These models serve as the foundation for sophisticated control schemes and performance forecasts. Furthermore, modeling techniques for a variety of multiphase machines, such as those with permanent magnets and induction types, have been extensively studied. For instance, permanent magnet multiphase machines combine the great efficiency of permanent magnet technology with the advantages of multiphase structures. To model these machines, flux linkage, and torque generation changes must be considered, along with the interaction of permanent magnets with multiphase currents. According to [11], research on induction-based multiphase machines has also concentrated on enhancing the precision of steady-state and dynamic performance estimations, which are crucial for high-power applications.

The modeling of multiphase machines has advanced significantly in the last few years. One significant development is the increasing use of numerical techniques, such as FEA, to more accurately model and predict these machines' performance. These techniques make it possible to analyze electromagnetic fields in great detail, which makes it easier to anticipate losses, efficiency, and thermal behavior. Furthermore, the prediction of transient behaviors in multiphase machines has been improved by the development of dynamic modeling tools, particularly during failures like open-phase or short-circuit circumstances. According to [12], this is essential for ensuring the safe and dependable operation of multiphase systems.

A generalized dq model for multiphase induction motor drives has been investigated in a large and expanding body of research. These multiphase (n-phase) induction motor drives, which have more than three phases, have several benefits over traditional three-phase drives, according to [13]. These include reduced torque ripple, increased torque density, enhanced fault tolerance, stability, high efficiency, and a lower current per phase without raising the voltage per phase. Additionally, the study showed that a larger power output inside the same frame is possible when the number of phases is increased. A generalized model dq for n-phase induction motor drives has been investigated in a thorough and expanding body of research. Multiphase (m-phase) induction motor drives, which have more than three phases, provide many benefits over conventional three-phase drives, as demonstrated by reference [13]. Among these benefits are reduced torque pulsation, increased torque density, enhanced fault tolerance, stability, high efficiency, decreased current ripple, and a drop in current per phase without raising the voltage per phase. Additionally, they talked about how adding additional phases enables higher power within the same frame.

In two volumes, [11] has discussed recent developments in the design, modeling, and control of multiphase machines. Using the extra degrees of freedom in multiphase machines and taking advantage of their fault-tolerant features without the need for additional hardware is explored in the first volume. The second book looks at multiphase generation, particularly in freestanding and grid-connected wind energy conversion systems. Multiphase machines have many advantages, including lowering the stator current per phase without increasing the voltage per phase, lowering the DC link current harmonics, and increasing dependability, even though their main purpose was initially to reduce torque pulsation. It is also possible to increase the torque per RMS ampere while maintaining the same machine volume by increasing the number of phases. In multiphase systems, the additional degrees of freedom enable the supply of numerous motors from a single inverter or the injection of harmonic currents. Better noise characteristics and lower stator copper losses are two more benefits of multiphase systems. It is anticipated that high-phase order drives will only be used in specific applications that demand a high degree of reliability, such as ship propulsion, aircraft, electric/hybrid cars, and high-power applications where one leg of the drive consists of merging multiple solid-state devices. Because many of

the required components are already included in contemporary designs, large drives are not burdened by the requirement for separate drive units in a multiphase system.

A decoupled machine model and the unique mapping of all odd-order harmonics into the resulting subspaces are two benefits of utilizing VSD to describe a multiphase machine, according to research on the VSD method for asymmetrical multiphase machines by [14]. Recently, [15] converted the conventional three-phase induction motor into a device with coiled stator coils that are independently regulated. The stator winding design, which makes it easier to independently energize and operate each coil in the stator slot, is the distinctive characteristic. As a result, the possibility to change the stator winding's active phases and pole count while it is operating is investigated.

Particularly in electromobility, VPPIMs are becoming more and more important for applications requiring a broad range of torque and speed. According to [5], [16], one of the main advantages of VPPIMs is their capacity to alter the number of magnetic poles in real-time, therefore increasing their operating capabilities. These studies highlight the importance of VPPIMs in applications like electromobility that call for a variety of torque-speed profiles. The primary benefit of VPPIMs is their ability to dynamically modify the number of magnetic poles while in use, significantly increasing their adaptability and functional range. Furthermore, the machine modeling is covered in great detail by the HPD theory[17], [18].

2.3 Recent Developments in Multiphase Converters

The growing need for high-performance, energy-efficient, and dependable power conversion systems in a variety of applications, such as industrial drives, EVs, and renewable energy, has fueled recent advancements in multiphase converters. Compared to conventional three-phase converters, multiphase converters—which function with more than three phases—offer a number of benefits, including enhanced thermal performance, decreased harmonic distortion, and enhanced fault tolerance. Because of these benefits, they are very appealing for high-power applications where compactness, efficiency, and resilience are crucial. The increasing needs of contemporary electrical systems have necessitated improvements in multiphase power electronics' design, control schemes, and integration.

The creation of more effective topologies is one of the major developments in multiphase converters. Despite their widespread use, traditional three-phase converters can have substantial harmonic distortion and decreased efficiency at high power levels. Higher efficiency and better power quality are the outcomes of multiphase converters, especially those built on five- or six-phase topologies, which provide a more balanced load distribution and lower THD. In order to capitalize on these advantages, researchers have concentrated on creating novel converter topologies, such as hybrid converters, modular multilevel converters (MMC), and multilevel converters. These topologies make better use of the available voltage levels, which lowers the converter's size and cost while increasing its overall performance and efficiency. For example, scalability is made possible by the use of modular converters, which is especially helpful in applications where the converter must manage different power levels, such as renewable energy generation [19].

Control strategies for multiphase converters have also seen significant advancements. One major development is the implementation of more sophisticated modulation techniques, such as SVM, which can effectively control the output voltage and current waveforms in multiphase systems. SVM has become the preferred technique for multiphase converters due to its ability to reduce harmonic distortion, improve efficiency, and provide better dynamic response. Researchers have developed various SVM approaches tailored to multiphase systems, including optimized algorithms for multi-level and multi-phase converters that help minimize switching losses and improve the overall performance of the converter [20]. Additionally, predictive control methods, such as MPC, are gaining popularity in multiphase converter applications. MPC allows for better regulation of output

voltage and current, especially under varying load conditions, by predicting future states of the system and adjusting control inputs accordingly [21].

Research on the fault tolerance and dependability of multiphase converters has also been ongoing. The capacity of multiphase systems to function even in the face of faults, including open-phase failures, is one of its intrinsic advantages. The goal of recent research has been to create fault-tolerant control schemes that allow multiphase converters to function in deteriorated environments without suffering appreciable performance losses. To increase the dependability of multiphase converters in industrial and automotive applications, for instance, phase reconfiguration techniques have been developed, in which the converter dynamically reconfigures its operation to avoid problematic phases [22]. These methods not only increase the converter's fault tolerance but also help systems last longer and require less maintenance.

Integrating power electronics with digital control systems is another significant advancement in multiphase converter technology. More accurate and real-time management of multiphase converters is now possible thanks to the growing availability of high-performance DSPs and FPGAs. These digital platforms make it possible to apply sophisticated algorithms that enhance the overall robustness and performance of multiphase converters, such as adaptive control and fault detection. Additionally, multiphase converter designs are more flexible and scalable due to the ease with which digital control systems can adapt sophisticated modulation methods [23]. Better integration with renewable energy systems, where the converter must manage fluctuating power input and output conditions, is also made possible by the combination of multiphase converter topologies and improved digital control. An ideal pulse pattern PWM was suggested in [24] for a high-capacity nine-phase VSI powering a nine-phase induction motor (which has a single three-phase winding on the rotor and three sets of independent three-phase windings on the stator). The current control loop was removed from the inverter's control system. A new setup was introduced, incorporating nine low-rating (20%) of the motor capacity) single-phase reactors. The reactor turns ratio was chosen to be 1:2 $\sin(\pi/18)$:1 to eliminate lower order harmonics (5th, 7th, 11th, and 13th) from the inverter/motor phase voltages and currents and to balance fundamental currents during unbalances. To remove even harmonics from the current/voltage waveform, an optimal pulse pattern based on the Lagrangian multiplier method was developed. The proposed optimal pulse pattern PWM technique was compared to the ramp comparison PWM and demonstrated a significant reduction in harmonic amplitude. Additionally, the new configuration significantly reduces the electromagnetic noise of the motor.

Looking forward, the future of multiphase converters lies in continued advancements in converter topologies, control strategies, and fault tolerance methods. As the demand for more efficient and reliable power conversion systems grows, research will likely focus on optimizing multiphase converters for even higher power levels, greater scalability, and better integration with emerging technologies, such as electric grid systems and distributed energy resources. Additionally, the development of more compact, cost-effective components and the integration of advanced digital control methods will continue to push the boundaries of what multiphase converters can achieve in both commercial and industrial applications.

2.4 Recent Developments in Multiphase Controllers

Direct torque control stands as a highly effective technique for achieving superior performance in motor drive regulation and is widely recognized across industries for controlling three-phase induction motors. DTC operates fundamentally on instantaneous space vector theory, harnessing the non-ideal characteristics of inverters to provide exceptional dynamic control. The idea of DTC was recently modified for five-phase induction motor control in [25], and a comparison of three-phase and five-phase DTC systems was provided. To implement the control architecture, a 32-bit floating-point TMS320C32 DSP was used. A five-phase inverter

has 32 potential voltage space vectors, allowing for more flexible control than a three-phase inverter, which can only use up to eight in motor applications. In comparison to three-phase induction systems, the use of a five-phase drive system resulted in improved performance with the induction motor, offering more accurate and quick control over flux and torque as well as noticeably less torque and flux ripple.

In addition to these advancements, multiphase converters are being increasingly used in renewable energy and electric vehicle systems, where dependability and efficiency are crucial. Multiphase converters are utilized in the propulsion systems of electric vehicles to regulate the power supply to the electric motor, resulting in improved performance and a longer lifespan. Multiphase converters are used in renewable energy systems, such wind and solar power, to effectively transform power from variable sources into usable electricity, guaranteeing increased system efficiency and reduced losses. Multiphase converters are perfect for these energy-intensive applications because of their versatility to various power levels and capacity to lessen component stress under high load situations [26].

The use of multiphase inverters was first reported by [27] in a variable-speed five-phase induction motor drive application. It utilized a forced commutated thyristor-based inverter in ten-step operating mode. The torque ripple decreased to one third compared to the equivalent three-phase case and was at an increased frequency. However, the machine current contained a strong third-harmonic component, which generated additional losses. To avoid these losses and obtain fast current control, several PWM techniques have been developed for multiphase VSIs, such as those reported in [28]. A novel SVPWM algorithm for multilevel multiphase voltage source converters is presented by [29]. This algorithm is the result of the two main contributions of this paper: the demonstration that a multilevel multiphase modulator can be realized from a two-level multiphase modulator, and the development of a new two-level multiphase SVPWM algorithm. It also has low computational complexity, and it is suitable for hardware implementations. A complete mathematical model of a five-phase VSI, based on space vector representation, was developed by [30]. The inverter operation in ten-step mode and PWM mode was discussed. The hysteresis-type PWM current regulation was used for the drive under rotor flux-oriented indirect vector control conditions. An SVPWM was proposed by [31] for a five-phase VSI control in conjunction with induction motor drives. The same strategy was employed by [32] in a five-phase synchronous reluctance motor drive.[33] employed the SVPWM technique in a split-phase induction motor drive fed by a six-phase VSI.

Vector control and direct torque control of a five-phase induction motor with concentrated full-pitch winding was also developed and implemented again using 32 bit floating point DSP TMS320C32 in [25]. The proposed vector controller uses fundamental current in conjunction with 15 third harmonic stator current injection to provide quasi-rectangular current, which yields a rectangular air gap flux in the concentrated winding induction motor. It was shown that this approach enhances the torque output by 11.2% under dynamic conditions and by 10 during the steady state operation, compared to the case when only fundamental current is fed to the machine. The DTC provides high performance in terms of smaller current, flux, and torque ripples due to a large number of space vectors for controlling the machine. Further, zero switching vectors are not needed to implement space vector modulation for five-phase PWM inverter for DTC, and thus, the wear and tear of motor bearing can be avoided. In [32], a vector control method utilizing space vector PWM was developed for a five-phase synchronous reluctance motor drive. This drive's control system was also realized using a 32-bit floating point DSP TMS320C32.

MPC for multiphase electric drives has garnered more attention in recent years because of its many benefits for managing non-linearity in power systems and attaining quick dynamic response. MPC is a control approach that anticipates and responds to changes in system circumstances more effectively than traditional controllers because it solves an optimization problem at each sample time to forecast the future behavior of the system. The intricacies of multiphase converters, which are frequently exposed to fluctuating load circumstances,

suboptimal components, and dynamic disturbances, benefit greatly from this predictive capabilities. MPC has proven to be a successful strategy in the context of renewable energy systems, where electricity output from sources like solar and wind is erratic and intermittent. Through improved voltage management, smoother power conversion, and increased overall efficiency, it can maximize the performance of multiphase converters. As explained in [34], MPC's capacity to handle these difficulties makes it a viable option for enhancing the control and stability of multiphase converters in renewable energy applications, where accuracy and flexibility are essential for preserving grid reliability and optimizing energy efficiency.

2.5 Recent Developments in VPPIMs

Recent advancements in VPPIMs have drawn a lot of interest because of their potential benefits in a number of applications, most notably in enhancing electric drive performance, flexibility, and efficiency. An electric motor type known as a variable phase-pole induction machine has a distinct advantage over conventional fixed-pole machines in that its number of poles may be dynamically changed while it is operating. These machines are appropriate for applications where efficiency, adaptability, and performance are critical, such as electric vehicles, renewable energy systems, and industrial machinery, because of their capacity to adjust the number of poles, which enables a wider variety of operating speeds and torque capacities.

The difficulty of simulating and managing the behavior of the machines under varying operating settings is one of the main obstacles in the development of VPPIMs. Induction machines are often modeled using a set number of poles, and their steady-state performance is examined. However, the electrical and mechanical properties of the machine, including inductance, back EMF, and torque generation, get more complicated in VPPIMs as the pole number varies dynamically. The development of precise mathematical models that can forecast these devices' performance under various pole configurations has been the focus of recent studies. These models usually include dynamic simulations that consider the interactions between the stator and rotor as the number of poles changes, as well as a complete examination of the electromagnetic field [35]. To increase the precision and effectiveness of these simulations, sophisticated methods like FEA and multiphase modeling are being utilized more and more.

The control strategies for VPPIMs have been another important area of development. Constant-frequency control, which is best suited for a fixed pole arrangement, is used in conventional induction devices. VPPIMs, on the other hand, call for more complex control methods that can adapt to variations in the number of poles while preserving peak performance throughout a broad range of operating speeds. Sensorless control, MPC, and adaptive control approaches—which enable real-time modifications to the machine's operational parameters—have been the main focus of recent developments in control strategies for VPPIMs. These methods ensure that the machine operates efficiently even when the pole number is dynamically changed, minimizing losses and maximizing torque output at various speeds. In particular, sensorless control strategies, which do not require direct measurement of rotor position or speed, are a promising development that can reduce system complexity and cost in practical applications [36].

From a design perspective, VPPIMs present unique challenges. The mechanical design of the rotor and stator must accommodate the ability to change the number of poles without sacrificing structural integrity or efficiency. Researchers have explored innovative rotor topologies and stator winding configurations that enable seamless transitions between different pole numbers while maintaining good performance and reducing the risk of mechanical failure. In addition, advancements in materials, such as the use of high-performance magnetic materials, have contributed to improving the overall efficiency and torque density of VPPIMs [37]. These design improvements, coupled with enhanced cooling systems, help in managing the thermal challenges that arise from the increased complexity of variable pole operations.

Applications for VPPIMs include renewable energy systems like wind turbines and electric vehicles (EVs) that need variable speed drives. VPPIMs give EVs the adaptability to effectively change operating speeds, which enhances overall energy efficiency and lessens component wear. The ability to change the pole number in wind energy systems optimizes power generation and lessens mechanical stress on the system by enabling the machine to function more effectively throughout a variety of wind speeds. VPPIMs' capacity to adapt to various operating situations also makes them ideal for industrial settings where exact speed and torque control is essential for energy conservation and process optimization.

Future developments for VPPIMs are probably going to require more improvement in mechanical designs, control schemes, and modeling methodologies. Integrating VPPIMs with cutting-edge power electronics, such solid-state transformers and sophisticated inverters, to allow for more adaptable and effective operation, is one exciting field of study. Furthermore, the performance of VPPIMs in a variety of applications could be further improved by the creation of machine learning algorithms for real-time machine parameter optimization, making them even more adaptable and efficient in satisfying the needs of contemporary energy systems [8].

After identifying the variables that affect pole phase changing, this research created a thorough framework to help designers examine how multiphase drive pole phase change affects controller performance. [38] described pole-changing winding with close ratio and 1:N ratio utilizing the 3//Y / 3//y approach, and [39] provided a thorough description of the design, modeling, and control for pole-phase modulation induction motors. [40] used a multi-harmonic technique to analyze a phase-pole variable induction machine. Discrete DFT will be used to interpret the Clarke transform as a space, making it easier to distinguish between vector and harmonic spaces. For every phase-pole arrangement, the same amount of harmonic spaces will be produced using this interpretation. The obtained transform will then be used to convert the WICSC machine parameters into the $\alpha\beta 0$ and $dq0$ reference planes.

[41] has discussed finite element and experimental studies of an electronic pole-change drive. An induction motor drive with a wide speed range that uses electronic pole change has been studied and examined. [42] examines modular multiphase drives for variable pole induction machines in electric vehicles. Electric vehicles require high-power drivetrains that are reliable, efficient, and small. Significant results show that, in comparison to fixed-pole machines, variable-pole induction machines (IM) provide a feasible magnet-free solution with notable benefits, including a wider speed range and improved performance under all load circumstances. [43] investigates the viability of rearranging multiphase machine windings for all-electric cars. The objectives are to increase the machine's constant torque area, prevent torque pulsations related to gear shifts, postpone the onset of field weakening, and reduce the dangers connected with it. Measurement data from a test setup using a six-phase machine is used to develop and validate the reconfiguration approach.

In [44], a dynamic pole-phase modulation induction machine model has been examined. The model and the paper's conclusions explain machines with any number of electrical inputs and combinations of pole counts. For each number of poles, decoupled energy conversion subspaces are constructed using the degrees of freedom available in multiphase vector space decomposition. This makes it possible to use traditional control methods. Results from simulations that use field-oriented control approaches to show a smooth 2-pole/6-pole transition are shown.

PAM's approach in [45] tackles the problem of extending the speed range without increasing the size of high-speed induction motors. In the article, a possible nine-phase six-terminal induction motor having a distributed wind fractional slot concentrated winding schema. This configuration makes electronic pole-changing with a 2:1 pole ratio, achieving equal magnetizing current for both winding pole sets. The machine has shown through simulations and experiments constant power operation over a speed range surpassing 4 per unit.

2.6 Recent Developments in Multiphase Machine Parameter Estimation Methods

Since they are essential to improving the performance and dependability of multiphase machines, recent advancements in parameter estimation approaches have attracted a lot of interest. Accurate estimation of machine characteristics is crucial for optimal machine design, control, and diagnostics, as multiphase machines such as five-phase and six-phase systems are utilized more frequently in applications requiring high power, efficiency, and fault tolerance. Greater fault-tolerant capabilities, increased energy economy, and greater machine control are all made possible by accurate parameter estimates. Machine variability, operating conditions, and the complexity of multiphase designs make traditional parameter estimation techniques like direct measurements or depending on manufacturer data often inadequate. Newer methods have therefore been created to get around these restrictions.

System identification methods, which model the machine's dynamic behavior and compare it to observed data to extract the machine parameters, are one of the most well-known modern approaches to parameter estimation. These strategies fall into two categories: offline and online. Through controlled experimental data, offline methods determine machine characteristics that may be utilized for analysis and simulation. However, offline approaches frequently overlook real-time operational conditions. Online system identification techniques have been created to get around this, enabling real-time estimation of parameters, including mutual coupling between phases, resistance, and inductance. Online techniques use real-time machine data, which increases their flexibility in response to changing operating conditions and yields more precise findings for control purposes [46], [47].

Combining AI and ML approaches is another important development in parameter estimation for multiphase machines. The use of machine learning methods, such as support vector machines, neural networks, and evolutionary algorithms, to estimate parameters from massive datasets has grown in popularity. Because multiphase systems are complicated and nonlinear, these techniques are especially useful when more conventional approaches cannot produce reliable estimates. For example, the link between the input voltages, currents, and mechanical outputs of multiphase machines has been modeled using neural networks. Then, under various operating situations, these models can be utilized to estimate machine parameters like resistance and inductance [48]. Furthermore, by decreasing the error between anticipated and measured values, genetic algorithms have been utilized to optimize parameter estimation, providing a reliable solution to multivariate problems.

Notable developments have also been made in applying optimization methods for parameter estimation. Techniques such as PSO, Kalman filtering, and least-squares estimation have been used to improve parameter estimation in multiphase machines. For instance, Kalman filtering has been used to monitor real-time machine parameter changes while accounting for measurement noise and uncertainty. This is especially helpful for multiphase machines, whose characteristics may fluctuate due to different operating conditions and failures. By mimicking the behavior of particles in a swarm, PSO, on the other hand, has been used to determine the ideal parameter values. Iteratively, it finds the best answer. PSO works especially well for complex multiphase machine problems, including high-dimensional parameter estimates [49].

Furthermore, the necessity for hybrid approaches that incorporate several estimating techniques has arisen due to the growing complexity of multiphase machines. These hybrid techniques seek to increase accuracy and resilience by utilizing the advantages of different methodologies. For example, more precise and trustworthy parameter estimates can be obtained by integrating machine learning or optimization methods with system identification. Studies have demonstrated that hybrid approaches, including fusing neural networks with particle swarm optimization, can significantly enhance the efficiency of parameter estimation algorithms in multiphase machines, resulting in improved fault detection and control [50].

In fault diagnosis and fault-tolerant control, the significance of precise parameter estimation is especially noticeable. In multiphase machines, defects like insulation deterioration or winding short circuits can alter parameters like resistance and inductance. To guarantee the ongoing and dependable operation of these devices, early and precise problem detection is essential. By comparing the estimated parameters with nominal values and discovering any discrepancies that might point to possible problems, parameter estimating algorithms have been modified to detect these defects. The increasing usage of multiphase machines in safety-critical applications such as electric vehicles, industrial automation, and aerospace has been facilitated by these advancements in fault detection and diagnosis [51].

The identification of parameters for distributed multiphase winding induction machines has been documented in two volumes by [52]. This study suggests straightforward offline techniques to estimate the stator resistance and stator leakage inductance of multiphase IMs with distributed windings under different conditions, leveraging the degrees of freedom provided by the non-flux/non-torque producing current components. In the initial paper, once these parameters are identified, the rotor parameters can be easily derived by combining them with the total values obtained from locked-rotor tests. This process allows the simple differentiation of the stator and rotor parameters, which is notoriously challenging in three-phase IMs, where the equality of leakage inductances and a constant stator resistance are typically presumed.

Thus, the magnetizing inductance can be more precisely evaluated from no-load tests, as this avoids the estimation error that would occur if both leakage inductances were assumed to be the same. The proposed methods are experimentally validated on two different five-phase induction motors. The second paper details and applies a procedure to estimate the parameters of a five-phase induction machine, which can also be extended to other multiphase machines with a higher number of phases. The method relies on standstill time-domain tests and recursive least-squares algorithms. Experimental results demonstrate the identification method developed by tests on two different five-phase induction machines. The results are correlated with parameters obtained in Part 1 of this paper, where the electrical parameters of the same two five-phase inverter-fed induction motors were identified using different procedures based on the sinusoidal excitation of the machine.

Reference [53] presents a detailed analysis of methodologies for estimating the parameters of RFO induction motors. The paper includes experimental and simulation examples to illustrate different parameter estimation techniques.

2.7 Recent Developments in Sensorless Drives

Recent developments in multiphase sensorless drives have sparked significant interest due to their ability to enhance the performance, reliability, and cost-effectiveness of electric drives, particularly in high-power applications such as electric vehicles (EVs), industrial automation, and renewable energy systems. Position and speed sensors are frequently used in conventional drive systems to supply feedback for motor control. However, using sensors adds complexity, expense, and reliability problems, particularly in severe situations. A possible way to get around these issues while preserving high performance and fault tolerance is to use sensorless control approaches for multiphase machines, such as five-phase and six-phase systems.

Creating more precise rotor position and speed estimate techniques is one of the significant developments in multiphase sensorless drive technology. Because multiphase machines have intricate electromagnetic interactions, it can be challenging to estimate rotor position and speed without physical sensors. Conventional approaches to sensorless control have been widely employed, including model-based observers and back EMF-based systems. Nevertheless, these methods frequently suffer from transitory circumstances, noise, and parameter fluctuations. To improve the robustness and accuracy of rotor position and speed estimates in

multiphase systems, recent research has concentrated on utilizing sophisticated filtering techniques, such as Kalman filters and sliding mode observers [54]. More accurate control in dynamic and fault-prone contexts is made possible by these filters, which lessen the impacts of measurement noise and parameter uncertainties.

Incorporating cutting-edge ML and AI approaches is another noteworthy advancement in multiphase sensorless drives. By understanding the fundamental dynamics of the multiphase machine, machine learning algorithms—in particular, deep learning and neural networks—have demonstrated promise in raising the accuracy of sensorless control. These methods can simulate intricate, nonlinear interactions between mechanical and electrical variables that are hard to capture with conventional control techniques. To estimate rotor position and speed in real time, for example, researchers have used DNNs. This has increased performance in situations when traditional estimating techniques are not as effective, including when operating at low speeds or when there is a lot of noise [55]. AI-based methods are ideal for complicated multiphase sensorless drives because they provide several benefits, including fault tolerance, adaptability to changing operating conditions, and the capacity to learn from past data.

To enhance sensorless operation in multiphase machines, model-based approaches have been developed alongside machine learning. Advanced observers like the Luenberger observer and extended Kalman filters (EKF) have been investigated to improve rotor position and speed estimation under dynamic operating conditions. These observers use multiphase machine models and update their estimates regularly using stator voltage and current measurements. The creation of adaptive observers—which react in real time to shifting machine parameters like resistance and inductance that are impacted by load and temperature—has been the focus of recent study. The sensorless drive system is guaranteed to stay dependable and efficient under various operating situations thanks to these adaptive mechanisms [56].

Multiphase sensorless drives must also include fault detection and tolerance, especially in applications where safety is a top priority. Sensorless control techniques can be modified to improve fault detection and recovery tactics, and multiphase systems, by nature, have greater fault tolerance than conventional three-phase systems. To identify problems like phase failures, short circuits, and open circuits, researchers have created sophisticated fault detection algorithms that rely on estimating machine parameters and analyzing the electrical behavior of the machine. When paired with sensorless control strategies, these approaches can assist guarantee uninterrupted operation even when malfunctions occur. One significant development that enhances the robustness and dependability of multiphase sensorless drives in industrial and automotive applications is the capacity to identify and correct errors without needing external sensors. Furthermore, multiphase sensorless drives can now be used in real-time applications thanks to advancements in hardware and computational methods. Complex algorithms necessary for sensorless control may now be executed more quickly due to the growing processing capacity of DSPs and FPGAs. Because of this, sensorless drives are now more feasible for high-performance applications where quick reaction times are crucial. Additionally, by facilitating smoother and more effective operation of multiphase machines, developments in power electronics, such as creating more compact and efficient inverters, have supported the expansion of sensorless drive systems [57], [58].

There are virtually no studies on sensorless-based speed control for VPPIMs. However, standard model-based sensorless techniques might be extended to the VPPIM scenario with appropriate changes, based on the modeling and control methodology presented in [5]. VPPIMs' most notable technical feature concerns their MMF distribution relative to their traditional three-phase equivalents. The MMF can assume extremely particular characteristics with specified space harmonic content because VPPIMs are multiphase. This then translates into the potential for producing torque with various chosen space harmonics, or, to put it another way, producing torque with various pole pair numbers. Using the HPD theory to simulate the variable pole machine's air gap MMF, non-sinusoidal current, voltage, and air-gap flux linkage waveforms can be produced using harmonic injection techniques.

The need for sensorless algorithms for VPPIMs may be addressed by MRAS, Luenberger observers, EKFs, or other methods used for three-phase and multi-phase machines, as the HPD theory is an extension of the VSD used to control multiphase machines [59]–[63]. Although EKFs have a high computational cost, they are well known for producing highly accurate estimates of state variables in noisy environments. To reduce the discrepancy between, say, the estimated and actual rotor flow, the adaptive type observer modifies the parameters in real time. Because of this, it is a helpful tool for regulating and estimating the motor's speed and torque. The MRAS algorithm's adaptability guarantees that the estimation is accurate even in the face of shifting circumstances, including alterations in load and temperature cite1360072. However, how the rotor flux and speed estimation function while a VPPIM alters the number of magnetic poles is crucial to its application for VPPIMs.

2.8 Identification of the knowledge gap

According to the literature assessment, the challenges of calculating parameters and controlling the speed of these machines without using sensors are not sufficiently addressed by current research. This deficiency can result from the complex nature of VPPIMs, where precise estimation of the parameters and operating speed of the induction machine is essential for maximum efficacy, and an overall general lack of a universal modelling approach for VPPIMs. Existing approaches either fall short or require large sensor-dependent systems.

The study suggests the adoption of an HPD technique to get around this. Without requiring direct readings from physical sensors, this innovative method of modeling VPPIMs enables the extraction of essential characteristics and speed control. By separating and analyzing the machine's harmonic components, the HPD method dramatically improves the accuracy of speed control and parameter estimation, enabling the achievement of comparable or even higher performance levels than conventional, sensor-based methods. Since current methods are not as precise or effective in addressing the intricacies of VPPIMs in sensorless situations, it would be difficult, if not impossible, to achieve the same level of performance without using the HPD method. Accordingly, the paper contends that implementing HPD results in substantial scientific progress, bridging the knowledge gap and offering a fresh approach to the study and use of VPPIMs across various industries. By providing a novel technique (HPD) to produce a more efficient, sensorless approach to parameter estimation and speed control, the research essentially underlines the significance of the study in advancing the state-of-the-art in VPPIMs, marking a significant advancement in the field.

3 Modeling of the VPPIM

This chapter describes the determination of electric motor finite element-based modeling for variable phase-pole induction machines, serving as a general introduction of this thesis. This section is based on paper III.

3.1 Background

In the transportation industry, electric vehicles are being considered as a potential solution to reduce CO_2 emissions. Despite the enormous efforts toward fulfilling the stringent torque-speed and energy efficiency requirements of the propulsive units with synchronous machines, it seems that induction machines are still attracting some interest because of their rugged, affordable, and magnet-free construction [37].

The so-called VPPIMs represent a particular development in this field. The VPPIMs are essentially multiphase machines capable of changing the number of magnetic poles during real-time operation. In contrast to a conventional three-phase machine, this capability enables a larger torque-speed envelope that suits typical electromobility requirements [44], [64], [65]. Within VPPIMs, the literature presents essentially two design philosophies. On the one hand, there is the ISCAD [65], which uses a stator cage where each stator bar is individually supplied with a power electronics module. This approach brings high current and low voltage demands on the stator side, which might contrast with the increasing voltage levels in traction systems.

The other VPPIM option is constructing the stator using toroidal coils, each multi-turn coil wound around a single slot [44], [66], [67]. This approach allows for lower currents and higher voltages, potentially matching the voltage levels of the rest of the electrical system. There are also possible modifications of the single-slot toroidal coil approach, where multiple slots are wound together in a multi-turn coil. In this case, the stator winding manufacturing is simplified, although the VPPIM loses some phase-pole reconfigurability.

There are positive indicators that interest in VPPIMs is expanding. References [68], [69], suggest that variable phase-pole drives offer a less expensive, robust alternative capable of handling high overloads. VPPIMs have a torque density that is greater than that of conventional three-phase induction machines. Moreover, they are potentially equally torque-dense and more efficient than interior permanent magnet synchronous machines designed for electric traction applications if one considers a specific high-speed and low-torque operating point related to highway cruising speed [41], [70]. In electrical machinery, the primary focus is on the electromagnetic fields that dictate their functionality. As a result, the foundation lies in Maxwell's equations (3.1), (3.2), (3.3) and (3.4), a quartet of coupled partial differential equations that integrate the principles of electricity and magnetism in low-frequency approximation.

$$\nabla \cdot D = \rho \tag{3.1}$$

$$\nabla \cdot B = 0 \tag{3.2}$$

$$\nabla \times E = -\frac{\partial B}{\partial t} \tag{3.3}$$

$$\nabla \times H = J + \frac{\partial D}{\partial t} \approx J \tag{3.4}$$

Table 3.1: GEOMETRICAL DATA AND MATERIAL PROPERTIES OF THE VPPIM.

Parameters	Symbol	Value	Unit
Number of stator slots	Q_s	36	–
Number of rotor bars	Q_r	26	–
Number of turns	n_s	52	–
Air-gap	δ	0.3	mm
Axial Length	L_a	135	mm
Stator radius	$r_{s,in}$	75.1	mm
Rotor radius	r_r	74.25	mm
Shaft radius	r_{shaft}	18.3	mm
Description	Material	μ_r	$\sigma[Sm^{-1}]$
Stator lamination	Iron	$1x10^4$	0
Stator slot coil	Copper	1	$48x10^6$
Stator slot wedge	Air	1	0
Air-gap	Air	1	0
Rotor lamination	Iron	$1x10^4$	0
Rotor bar	Aluminum	1	$26x10^6$
Shaft	Steel	1	0

3.2 FEA Model of the VPPIM

VPPIMs are, in principle, induction machines with a couple of important modifications. When the single slots (or groups of slots) are wound independently, they allow the freedom to choose currents with amplitudes and phases resembling different phase-pole configurations. This phase-pole modulation capability resembles (but does not fully substitute) a multi-stage transmission drive. Moreover, they are inherently fault-tolerant values [66], [71]. The main drawback of VPPIMs is the potential complexity of the stator design and its supply, which needs to be a multiphase system with a centralized controller.

The VPPIM machine's 3D model, showing the squirrel cage rotor, the shaft, the internal stator coils, which are the path for the torque-producing currents, and the external stator coils, which serve as the returning current path, is illustrated in Figure 3.1 (a). The domain discretization (triangular mesh) and geometrical FEA model of the VPPIM is also illustrated in Figure 3.1 (b). Additionally, in Table 3.1, the geometrical parameters

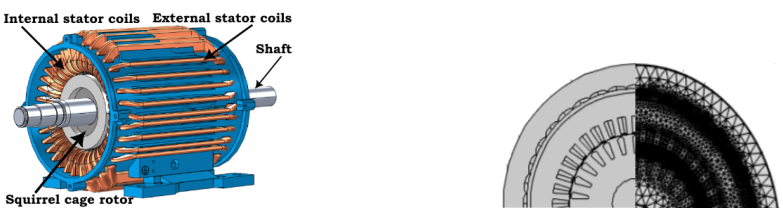

(a) The VPPIM **(b)** Geometry and mesh

Figure 3.1: 3D-CAD and FEA VPPIM design.

and defined materials for the analyzed VPPIM are illustrated. Once the prototype FE model has been developed, the subsequent action involves simulating the model, as depicted in the flowchart in Figure 3.2, followed by a verification of the results utilizing data from the data plate.

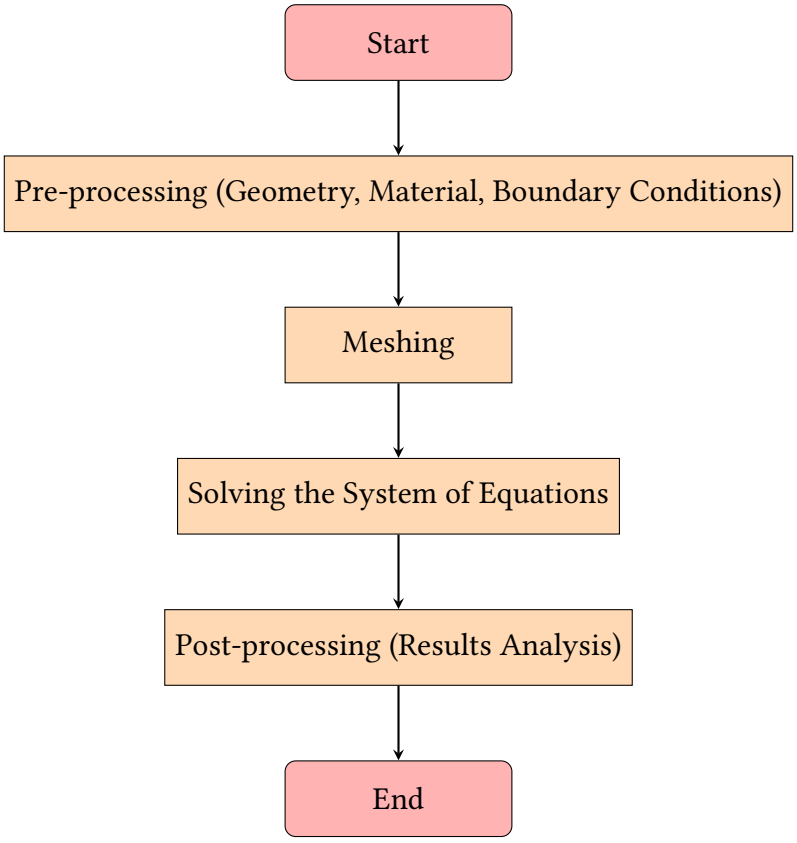

Figure 3.2: Flow chart of the Finite Element Method (FEM) process in COMSOL software.

3.2.1 Performance Analysis of the VPPIM

The design of an electrical machine is based on knowledge of the machine's magnetic field, which is used to compute the developed electromagnetic torque. However, solving the field equations is exceedingly time-consuming due to the complex shapes of electrical machines and the nonlinearity caused by the saturation of the iron core [64].

Squirrel-cage or wound-rotor induction motors supplied by sine-wave voltages have typically been the subject of conventional calculation techniques. However, these techniques are not capable of adequately analyzing motors with a unique geometry, such as VPPIM. The finite element method is effective when dealing with the complex geometry of the electrical machine [37]. Finite element methods are used to analyze the transient operation (locked-rotor) operation as well as the steady-state operation close to the synchronous speed. As creating real-scale prototypes is expensive and time-consuming, reliable calculations are required to ascertain whether the design is viable [72].

In the subsequent subsections, the VPPIM's performance, the developed electromagnetic torque, and the magnetic flux density distribution are analyzed in two different finite element-based techniques.

3.2.2 Computing torque using the Maxwell stress tensor method

The results of finite element analysis are typically used to determine the torque using the Maxwell stress tensor technique. In this method, the torque is determined by integrating the air-gap flux density in several contours that surround the rotor. In [73], the relation between electromagnetic torque based on Maxwell's stress tensor

and the MMF, is related as:

$$T_e = \frac{L_a \mu_0 r_{s,in}^2}{\delta} \int_0^{2\pi} S_{s,1}(F_{s,1} + F_{r,1}) d\varphi \tag{3.5}$$

In the air-gap, the magnetic flux density's radial component is also defined as:

$$B_r = \frac{\mu_0 (F_{s,1} + F_{r,1})}{\delta} \tag{3.6}$$

Following that, the line integral of the magnetic field intensity, H is evaluated along the circular path, C as:

$$\oint_C H.dl = H_\varphi r_{s,in} d\varphi \tag{3.7}$$

Since the stator current is represented as an (infinitely thin) current sheet located at the radius $r = r_{s,in}$, and integrating the current density over the surface, S, which is enclosed by the curve, C, along the circumference of the air-gap yields:

$$\int_S J.dS = \frac{\partial F_{s,1}}{\partial \varphi} \tag{3.8}$$

From the definition of Ampere's law, the magnetic field intensity is also obtained as:

$$H_\varphi = \frac{1}{r_{s,in}} \frac{\partial F_{s,1}}{\partial \varphi} = S_{s,1} \tag{3.9}$$

Now, since $B_\varphi = \mu_0 H_\varphi$, then the stator linear current density, $S_{s,1}$ can be equivalently expressed as:

$$S_{s,1} = \frac{B_\varphi}{\mu_0} \tag{3.10}$$

As a result, a linear current density at the stator's inner radius corresponds to the flux density's tangential component in the air gap. By inserting (3.6) and (3.10) into (3.5), the electromagnetic torque can be calculated as:

$$T_e = \frac{L_a r_{s,in}^2}{\mu_0} \int_0^{2\pi} B_r B_\varphi d\varphi \tag{3.11}$$

Different electrical machine characteristics, such as electromagnetic torque and magnetic flux density, are computed in a time-stepping and a time-harmonic analysis using FEA. The analysis then offers the model's dynamic and steady-state numerical solutions. The physics studies, in the subsequent subsections, discuss the above mentioned solutions approach.

3.2.2.1 Time-stepping study

The magnetic field of the induction machine is solved by using a time-stepping method, in which the rotor is rotated by an angle equivalent to the angular velocity of the rotor at each time step. The calculation of the magnetic field is a 3-dimensional problem by nature, but if effects like the skew of the rotor slots and end-winding fields are taken into consideration, it can be accurately expressed in a 2-dimensional model [72].

The axial effects are frequently neglected in a two-dimensional problem. When computing a fast-moving rotor, a small step length should be utilized. This results in long computation times [71]. To start with finding a numerical solution, the magnetic vector potential is introduced as:

$$B = \nabla \times A \tag{3.12}$$

Using Ampere's law formulation and inserting (3.12) into it results in:

$$\nabla \times (\nabla \times A) \approx \mu J \tag{3.13}$$

The current density resulting from a time-varying charge distribution and an additional voltage is then further expressed:

$$\frac{\nabla^2 A}{\mu} - \sigma \frac{\partial A}{\partial t} = -J_z + \sigma \nabla V_{pot} \tag{3.14}$$

For the rotor slots, which are short-circuited on each axial end, $V_{pot} = 0$ holds. Hence, the reduced electric scalar potential only contains z component, and is described as follows:

$$\nabla V_{pot} = \frac{\partial V_{pot}}{\partial x}\hat{x} + \frac{\partial V_{pot}}{\partial y}\hat{y} + \frac{\partial V_{pot}}{\partial z}\hat{z} = \frac{\partial V_{pot}}{\partial z}\hat{z} \tag{3.15}$$

With the above assumptions, the equation has been re-expressed as:

$$\frac{\nabla^2 A_z}{\mu} - \sigma \frac{\partial A_z}{\partial t} = -J_z + \sigma \frac{\partial V_{pot}}{\partial z} \tag{3.16}$$

Then the magnetic flux density B is readily obtained from the magnetic vector potential as:

$$B = B_x\hat{x} + B_y\hat{y} = \nabla \times A_z\hat{z} = \frac{\partial A_z}{\partial y}\hat{x} - \frac{\partial A_z}{\partial x}\hat{y} \tag{3.17}$$

The magnetic flux lines are, hence, useful for understanding how the flux is distributed in different parts of the machine. Hence, the Maxwell stress tensor approach calculates the electromagnetic torque as follows from the above-described equations:

$$T_e = \frac{C_{s,lam} L_a}{\mu_0} \left(\frac{r_r + r_{s,in}}{2} \right)^2 \int_0^{2\pi} B_r B_\varphi d\varphi \tag{3.18}$$

3.2.2.2 Time-harmonic study

Induction machine steady-state operation can be predicted with the use of time-harmonic modeling. Time-stepping is a more complex simulation because of the time dependence [73]. To circumvent the problem with time dependence as expressed in (3.14), it can be assumed that all the field quantities are varying sinusoidally with a single, fixed frequency ω. Thus, a $j\omega$-phasor is introduced in the expression of the z-component of the magnetic vector potential and current density elaborated as:

$$\frac{\nabla^2 \bar{A}_z}{\mu} - j\omega\sigma\bar{A}_z = -\bar{J}_z \tag{3.19}$$

Once a solution is found for the above equation, the magnetic vector potential is found as:

$$A_z = \Re(\bar{A}_z e^{j\omega t}) = \Re(\bar{A}_z)cos(\omega t) - \Im(\bar{A}_z)sin(\omega t) \tag{3.20}$$

Hence, the flux density B is calculated from the magnetic vector potential computation as:

$$B = \bar{B}_x\hat{x} + \bar{B}_y\hat{y} = \nabla \times \bar{A}_z\hat{z} = \frac{\partial \bar{A}_z}{\partial y}\hat{x} - \frac{\partial \bar{A}_z}{\partial x}\hat{y} \tag{3.21}$$

The Maxwell stress tensor torque computation in the case of time-harmonic analysis is expressed as:

$$T_e = \frac{C_{s,lam} L_a}{2\mu_0} \left(\frac{r_r + r_{s,in}}{2} \right)^2 \int_0^{2\pi} \Re(\bar{B}_r \bar{B}_\varphi{}^*) d\varphi \tag{3.22}$$

Provided that, the integral should be evaluated in the middle of the air gap.

3.2.3 Computing torque using Arkkio's method

An electrical machine's design is based on knowledge about the machine's magnetic field for calculating the developed electromagnetic torque. Averaging a large number of various integration pathways is one strategy to increase the precision of the stress tensor method. For this, the so-called Arkkio's approach is frequently applied. Instead of using a line integral, this approach uses a surface integral to calculate the torque. In a numerical solution, Arkkio discovered that the effect of the integration path on the result can be as much as 50% from the average torque [72].

Therefore, volume consideration is applied to determine torque throughout the meshing process. Hence, most of the numerical ripple will cancel out. It is an illustration of the weighted stress tensor technique and is effective for cylinder-shaped air gaps [73]. As a result of this, Arkkio's method can be used to calculate the electromagnetic torque to improve the numerical inaccuracies further and is expressed as:

$$T_e = \frac{L_a}{2\mu_0 (r_{s,in} - r_r)} \int_S \Re(\bar{B}_r \bar{B}_\varphi{}^*) r dS \tag{3.23}$$

Then electromagnetic torque computation is performed in the time-dependent and time-harmonic simulation using the COMSOL Multiphysics platform.

3.3 Simulation Results

Two different phase-pole configurations of the VPPIM are simulated to analyze the performance in the application for electric traction. For simulation purposes, different COMSOL multi-physics interfaces are used. Namely, the Rotating Machinery Magnetic interface (rmm), which models the electromagnetic field and rotation in the time domain, the inputs are the currents from the stator coils and voltages across the rotor bars. This module solves the magnetic vector potential in the z direction, A_z. Hence, the induced voltages across the coils, induced currents in the bars, and axial torque on the rotor are achieved. Also, the electrical interface module is used to examine the end winding impacts on the rotor model.

The time-harmonic and time-stepping studies are made to obtain the machine's steady state and dynamic performance, respectively, at the rated current of 4.89 $[A]$ peak for the 3-phase/4-pole and 3.45 $[A]$ peak for the 6-phase/2-pole VPPIM. The results for the two machine configurations are discussed in the following subsections.

3.3.1 Time-harmonic results for 3-phase/4-pole VPPIM

In Figure 3.3, the magnetic flux density of the VPPIM is depicted in time-harmonic simulation. The contour lines represent the magnetic vector potential and the surface plot is the magnetic flux density. The result shows that the magnetic flux density is higher close to the tooth of the stator slots and the rotor bars. The stator yoke has a lower value as compared to the stator tooth, which has a peak value of approximately 2 $[T]$, and becomes close to the saturation point at rated values.

The time-harmonic result of the electromagnetic torque is also shown in Figure 3.4(a). Given the 2D nature of the adopted motor model, it can be shown that the rated torque is predicted at the specified slip frequency. The machine's field-weakening mode of operation is studied as a result of this finding. A much sharper peak is shown at a lower slip frequency value and the breakdown torque is limited by magnetic saturation. As a result of failing to take into consideration the volume-wise computation of the Maxwell stress tensor method during the mesh pre-processing procedure, which is less sensitive to meshing errors, the findings of this computation are, nonetheless, a bit different from Arkkio's method result. Additionally, Figure 3.4(b) illustrates the radial direction magnetic field plot.

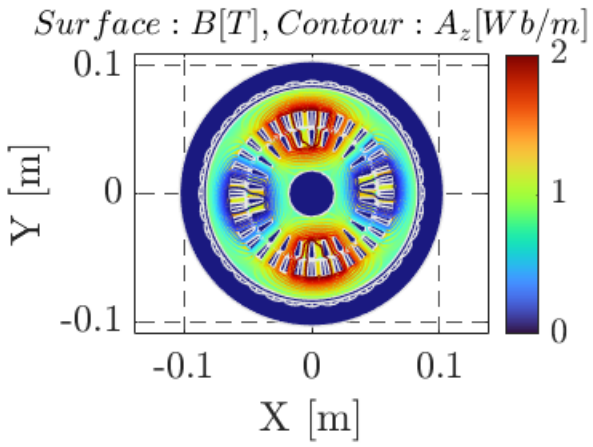

Figure 3.3: Magnetic flux density distribution: Time-harmonic study result for 3-phase/4-pole VPPIM.

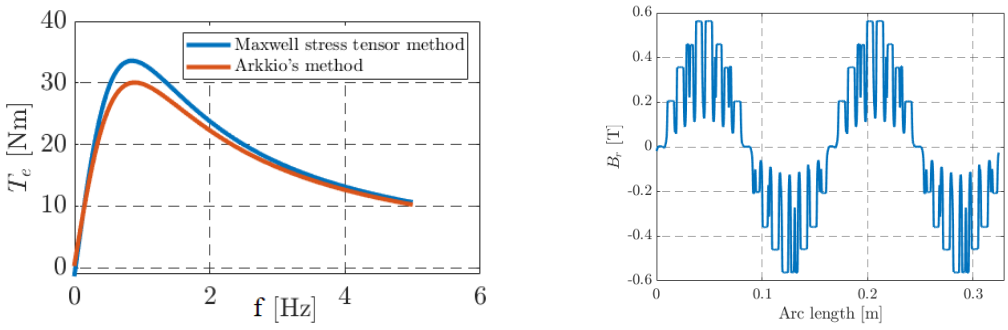

(a) **(b)**

Figure 3.4: (a) Electromagnetic torque for the machine configurations in time-harmonic study: Time-harmonic study result for 3-phase/4-pole VPPIM. (b) The spatial air-gap flux density along the middle of the air-gap over 4 poles.

3.3.2 Time-stepping results for the 3-phase/4-pole VPPIM

Time-stepping simulation result of the magnetic flux distribution of the VPPIM is illustrated in Figure 3.5. The figure shows the magnetic flux density peak value is around 2.5 $[T]$ at both the stator and rotor tooth and showed less intense distribution at the stator and rotor yoke. Furthermore, the time-dependent simulations of the VPPIM are important to predict non-steady-state operating conditions. The torque time-stepping simulation result for the VPPIM with different torque calculation methods are shown in Figure 3.6. The result demonstrated

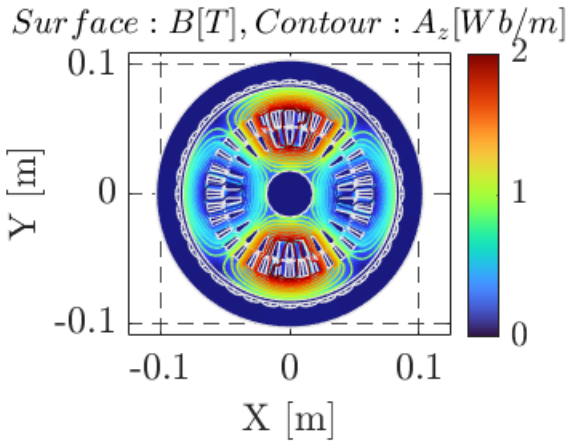

Figure 3.5: Magnetic flux density distribution: time-stepping study results for 3-phase/4-pole VPPIM.

that the torque computed in the two finite-element methods has agreed well. At 2 seconds, a step change in the load torque is applied. The motor gradually generates an equal amount of torque by sacrificing some speed. The torque ripples during startup should be mitigated with the use of suitable controllers.

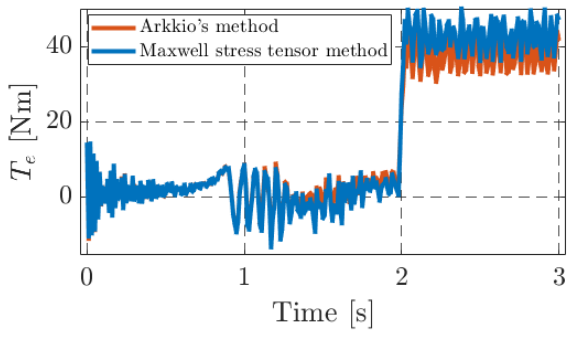

Figure 3.6: Electromagnetic torque for the machine configurations in time-stepping study: time-stepping study result for 3-phase/4-pole VPPIM.

3.3.3 Time-harmonic results for the 6-phase/2-pole VPPIM

Time-harmonic simulation result of the magnetic flux distribution of the VPPIM is illustrated in Figure 3.7. At the stator yoke, the magnetic flux density peaks at a value of around 2 $[T]$, near the stator tooth, it is less intense. Because more magnetic flux lines are crossed at the stator's yoke. As can be seen from the result, the 6-phase/2-pole VPPIM operates close to the saturation point at nominal values.

The simulated electromagnetic torque result for 6-phase/2-pole VPPIM is shown in Figure 3.8(a). The result demonstrated good agreement between the torque computed by both torque methods of the FEA analysis. The peak of the torque curve is substantially sharper, and the maximum torque is reached at a lower slip frequency. From the result also, it can predict the rated torque at the rated slip frequency. These findings are also used to examine the machine operation in the field weakening region. Furthermore, Figure 3.8(b) presents the magnetic field plot oriented in the radial direction.

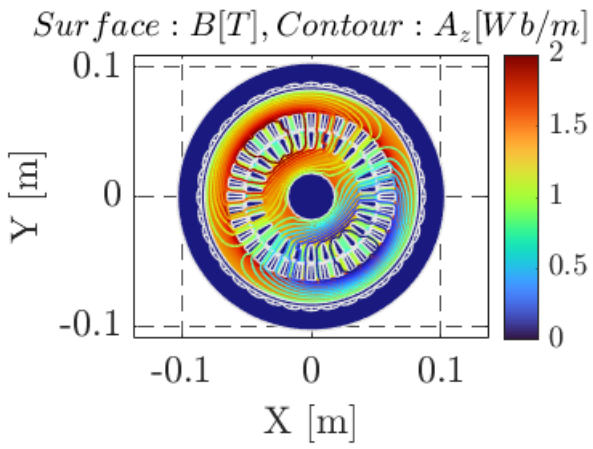

Figure 3.7: Magnetic flux density distribution: Time-harmonic study result for 6-phase/2-pole VPPIM.

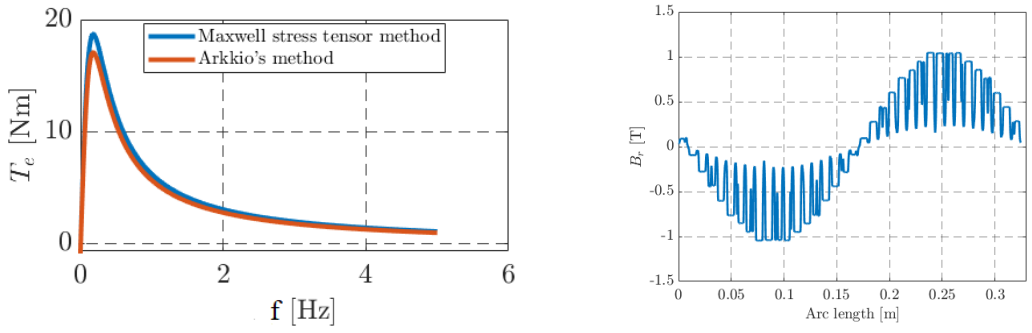

(a) **(b)**

Figure 3.8: (a) Electromagnetic torque for the machine configurations in time-harmonic study: The time-harmonic study results for 6-phase/2-pole VPPIM. (b) The spatial air-gap flux density along the middle of the air-gap over 2 poles.

3.3.4 Time-stepping results for the 6-phase/2-pole VPPIM

Time-stepping simulation result of the magnetic flux distribution of the VPPIM is illustrated in Figure 3.9. The magnetic flux density peak value is about 2 $[T]$, at the stator and rotor yoke and has less magnitude at the tooth of the stator slots and rotor bars.

The electromagnetic torque time-stepping simulation results for the VPPIM are shown in Figure 3.10. The result demonstrated the agreement between the two methods. In addition, the magnitude of the torque at the rated speed is reduced when compared with the 3-phase/4-pole counterparts. Fewer torque ripples are also seen during the start, highlighting the importance of the VPPIM's multi-phase nature. Hence, the above-mentioned merits lead to the application of traction being perfectly fitted.

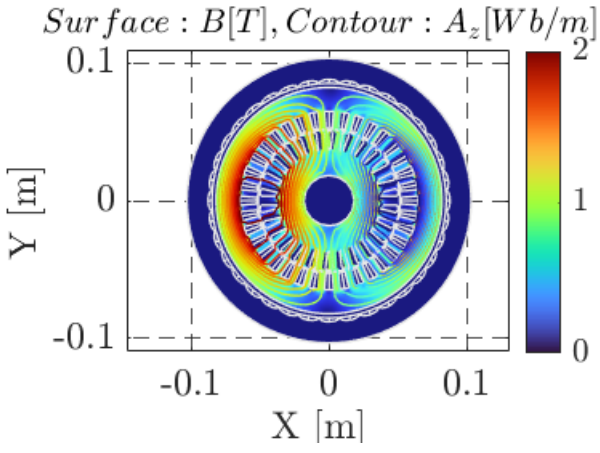

Figure 3.9: Magnetic flux density distribution: time-stepping study results for 6-phase/2-pole VPPIM.

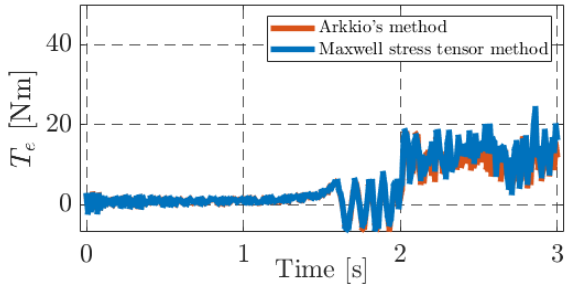

Figure 3.10: Electromagnetic torque for the machine configurations in time-stepping study: time-stepping study result for 6-phase/2-pole VPPIM.

3.3.5 Torque-speed plot for the 3-phase/4-pole VPPIM

A time-stepping simulation at rated torque and rated speed for 3-phase/4- pole machine is depicted in Figure 3.11. At the rated torque of 10 $[Nm]$, the rated speed is approximately 1500 $[rpm]$. The electromagnetic torque exhibits an oscillatory behavior during the start-up and gradually reaches a peak value at around 1 s. The load torque is changed stepwise at 2 s. By reducing speed slightly, the motor progressively produces an equivalent amount of torque.

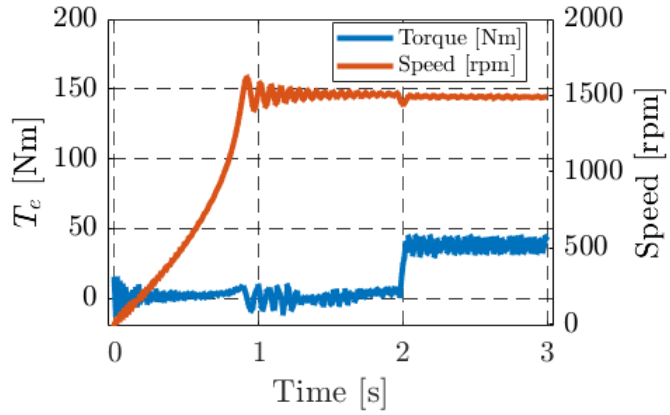

Figure 3.11: Torque-speed plot for 3-phase/4-pole VPPIM at rated load.

3.3.6 Torque-speed plot for the 6-phase/2-pole VPPIM

A time-stepping simulation at rated torque and rated speed for 6-phase/2- pole machine is depicted in Figure 3.12. With torque rated 5 Nm, the speed is rated around 3000 [rpm]. The electromagnetic torque oscillates during startup and increases steadily until it reaches a maximum value of about 1.7 s. After 2 s, the load torque is changed stepwise at 2 s. The VPPIM gradually generates an equivalent amount of torque by lowering the speed. As a result, to precisely match the field-weakening operation needs of the electric traction, the speed range is expanded at the expense of the electromagnetic torque.

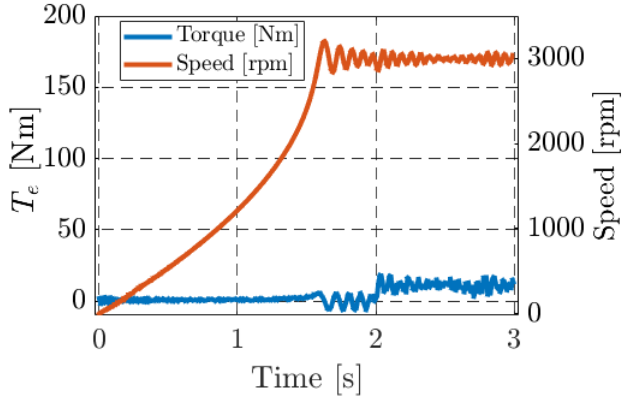

Figure 3.12: Torque-speed plot for 6-phase/2-pole VPPIM at rated load.

3.4 Summary

The chapter explores the advantages of induction machines over synchronous machines due to their durable and magnet-free construction. Particularly, VVPPIMs are discussed for their ability to modify the number of magnetic poles in real time, fitting well with the needs of electromobility. Two primary VPPIM designs are contrasted: the Intelligent Stator Cage Drive (ISCAD) and stators with toroidal coils. The VPPIM shows

promise with its high torque density and efficiency, superior to traditional three-phase induction machines and comparable to permanent magnet synchronous machines in certain conditions. Finite element analysis (FEA) is utilized for simulation, addressing the machine's electromagnetic torque and magnetic flux distribution. Results indicate that VPPIMs effectively maintain performance under high-speed and low-torque conditions, suggesting further research into optimal pole-phase configurations.

4 Parameter Estimation of the VPPIM

This chapter describes the determination of finite element-based parameter estimation techniques for variable phase-pole induction machines. This section is based on paper I.

4.1 Background

There is a class of electric machines known as variable phase-pole induction machines, where the number of pole pairs can be changed in real time by shaping the stator magnetomotive force shape through an increased amount of independent phases [44]. These machines are attractive for applications with a stretched torque-speed map over a wide area, like in electromobility, where it is challenging to design a conventional machine with a fixed number of pole pairs. VPPIMs could be surprisingly beneficial in this matter, with competitive efficiency and no use of magnets [74]–[76].

If such machines are supposed to be modeled and regulated in torque and speed with vector-controlled strategies, the knowledge of the electrical parameters in every phase-pole configuration is essential. While it is not an issue for three-phase induction machines [53], [77], [78], the situation is different for multiphase machines where parametric identification techniques are rather recent and there is still room for improvement. In a two-part article [52] and [79], an offline parameter identification algorithm for a multiphase induction machine with distributed windings in sinusoidal and time-domain excitation techniques is proposed, respectively. The technique focuses on parameter estimation based on current injection into non-flux and non-torque-producing vector spaces. Therefore, it has been shown that the segregated parameters of the stator and rotor can be accurately estimated.

The estimation procedures for multiphase machines found in the literature target the parameters of the VSD model, which is fundamental to their dynamic modeling and control [14], [80]. However, the VSD is a per-phase model, and therefore clashes with the nature of VPPIMs that do not have a fixed number of phases [7]. If the VSD theory is used to model and control VPPIMs, it will introduce discontinuities during the real-time phase-pole reconfiguration. This is due to the variation of the number of vector spaces as the number of phases changes [17].

To address the discontinuity problem, an extended theory that builds on the existing VSD theory, namely the HPD, has been introduced. The HPD allows the VPPIMs modeling and its current/speed regulation even in phase-pole transitions. It uses only one Clarke and one Park transformation for all possible phase-pole configurations. The principle of HPD lies in modeling the VPPIMs with several independent windings, each with its magnetic axis, that combined can form all the desired phase-pole configurations [81].

Adopting the HPD for VPPIMs helps in two ways: it introduces only one model for all possible phase-pole configurations, and it requires only one set of parameters that will remain constant throughout the operation of the VPPIM. In principle, the HPD model parameters could be estimated by numerical analysis, but no established and experimentally proven numerical method has been developed so far.

The work in [7] presents a numerical method for the parameter estimation of VPPIMs, using a different methodology concerning, for example, the analysis in [69]. The method is experimentally unproven. Thus, this research presents a theoretical and experimental comparison of the classical and HPD-based parameter

estimation techniques based on the FEA of VPPIMs, showing also the computational rapidity and accuracy of the latter with respect to experimental data.

4.2 The VPPIM

The WICSC machine is a VPPIM similar to the one used [44], and to some extent to the one used in [65]. All these machines can change the number of phases and poles during real-time operation. Different from [65], the stator is wound with one independent multi-turn toroidal coil for each available slot, where the return current runs externally to the stator frame [44], [66]. Figure 4.1 depicts the actual stator of the VPPIM in the KTH laboratory and its 2D-3D models. VPPIMs have two main advantages over conventional machines. The first is

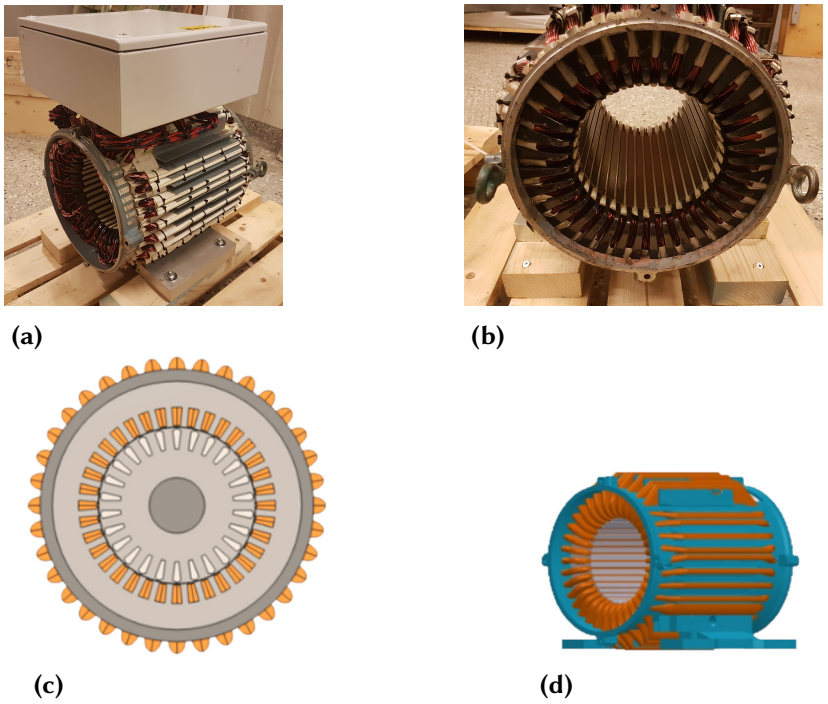

Figure 4.1: Picture and renderings of the VPPIM stator.

that the coils are wound independently, enabling a coil current control in each stator slot that allows complete freedom in the choice of phases and poles (within the limits given by the slot number). Second, the loss of a faulty coil affects the stator in a much lower grade than in conventional stator windings. The machine can also continue to operate with different nominal values even in the absence of individual coils. On the other hand, the return path of the current on the outside of the stator does not contribute to torque generation and is more or less equivalent to end windings [66]. The geometrical parameters and the defined materials for the studied VPPIMs are illustrated in Table 4.1.

4.3 Parameter estimation methods

The following sections describe the two-parameter estimation techniques used in this work for both the simulation and experimental results. The goal of the FEA-based methods described here below is to determine a value of the stator and rotor resistances, the self and mutual inductances, considering a linear magnetic circuit.

Table 4.1: GEOMETRICAL DATA AND MATERIAL PROPERTIES OF THE VPPIMs.

Parameters	Symbol	Value	Unit
Number of stator slots	Q_s	36	–
Number of rotor bars	Q_r	28	–
Number of turns	n_s	40	–
Air-gap	δ	0.85	mm
Axial Length	L_a	200	mm
Stator radius	$r_{s,in}$	75.1	mm
Rotor radius	r_r	74.25	mm
Shaft radius	r_{shaft}	22.55	mm
Description	Material	μ_r	$\sigma[Sm^{-1}]$
Stator lamination	Iron	$1x10^4$	0
Stator slot coil	Copper	1	$48x10^6$
Stator slot wedge	Air	1	0
Air-gap	Air	1	0
Rotor lamination	Iron	$1x10^4$	0
Rotor bar	Aluminium	1	$26x10^6$
Shaft	Steel	1	0

Magnetic saturation is temporarily neglected to demonstrate the correctness of the HPD approach which also builds on the assumption of linear magnetic circuits - as the conventional theory too.

4.3.1 FEA-based per-phase analysis

A two-dimensional FEA time harmonic analysis is adopted, where the rotor is held at a standstill and the frequency of the currents in the stator winding corresponds to the slip frequency [82]. From the steady-state analysis of AC motors, the slip of the induction motor is defined as the ratio of the difference between the stator and rotor angular frequency relative to the stator angular frequency:

$$s = \frac{\omega - \omega_m}{\omega} = \frac{\omega_1 - p\omega_m}{\omega_1} = \frac{\omega_s}{\omega_1} \tag{4.1}$$

where ω is the angular speed of the stator (mech.rad/s), ω_m is the angular speed of the rotor (mech.rad/s), p is the number of pairs of poles, ω_1 is the angular speed of the stator (el.rad/s), and ω_s is the angular slip frequency (rad/s). The per-phase stator impedance of the conventional T-equivalent circuit model is and expressed as:

$$Z_s = \frac{V_s}{I_s} = R_s + j\omega_s L_{\lambda,s} + \frac{\omega_s L_m (R_r^{'} + j\omega_s s L_{\lambda,r}^{'})}{\omega_s s (L_{\lambda,r}^{'} + L_m) - jR_r^{'}} \tag{4.2}$$

where R_s is the stator resistance, L_m is the magnetizing inductance, $L_{\lambda,s}$ is the stator leakage inductance, $L_{\lambda,r}^{'}$ is the rotor leakage inductance referred to the stator side, and $R_r^{'}$ is the rotor resistance referred to the stator side.

The T-model is then translated into the inverse-Γ model (see Figure 4.2) by using the subsequent relations.

$$\left.\begin{aligned} L_M &= \frac{L_m^2}{L_m + L_{\lambda,r}} \approx L_m \\ L_\sigma &= \frac{L_m(L_{\lambda,s} + L_{\lambda,r}) + L_{\lambda,s}L_{\lambda,r}}{L_m + L_{\lambda,r}} \approx L_{\lambda,s} + L_{\lambda,r} \\ R_R &= \left(\frac{L_m}{L_m + L_{\lambda,r}}\right) R_r \approx R_r \end{aligned}\right\} \tag{4.3}$$

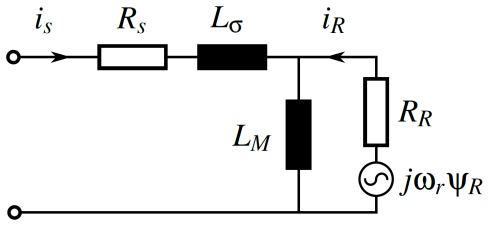

Figure 4.2: Dynamic inverse-Γ model for the induction machine.

From the analogy of the two models, the per-phase stator impedance for the equivalent inverse-Γ model is described as:

$$Z_s = R_s + j\omega_s\left(\frac{\bar{\phi}_s}{\bar{I}_s}\right) \tag{4.4}$$

where $\bar{\phi}_s$ is the per-phase flux linkage phasor extracted from the FEA simulation, and $\bar{I}_s$ is the per-phase stator current phasor. The phase inductance defined in (4.5) is a complex-valued quantity and computed from FEA simulations:

$$L_{ph}(\omega_s) = \frac{\bar{\phi}_s}{\bar{I}_s} \tag{4.5}$$

The phase inductance in (4.5) is segregated into its real and imaginary parts in (4.6).

$$L_{ph}(\omega_s) = \underbrace{L_\sigma + \frac{L_M}{1 + \omega_s^2\tau^2}}_{\text{Real}} - \underbrace{j\frac{\omega_s\tau L_M}{1 + \omega_s^2\tau^2}}_{\text{Imaginary}} \tag{4.6}$$

where L_σ is the sum of the leakage inductance for the stator and rotor sides, L_M is the magnetizing inductance, and τ is the rotor time constant[82]. The imaginary part of (4.6) is further elaborated with:

$$\Im\left(\frac{\bar{\phi}_s}{\bar{I}_s}\right) = -\omega_s\tau L_M - \omega_s^2\tau^2\Im\left(\frac{\bar{\phi}_s}{\bar{I}_s}\right) \tag{4.7}$$

Finally, from a set of n simulations where the slip frequency $\omega_s = 2\pi f_{slip}$ is varied, (4.6) can be expressed in matrix form as:

$$\begin{bmatrix} \Im(\frac{\bar{\phi}_{s,1}}{\bar{I}_s}) \\ \Im(\frac{\bar{\phi}_{s,2}}{\bar{I}_s}) \\ \vdots \\ \Im(\frac{\bar{\phi}_{s,n}}{\bar{I}_s}) \end{bmatrix} = \begin{bmatrix} \omega_{s,1} & \omega_{s,1}^2\Im(\frac{\bar{\phi}_{s,1}}{\bar{I}_s}) \\ \omega_{s,2} & \omega_{s,2}^2\Im(\frac{\bar{\phi}_{s,2}}{\bar{I}_s}) \\ \vdots & \vdots \\ \omega_{s,n} & \omega_{s,n}^2\Im(\frac{\bar{\phi}_{s,n}}{\bar{I}_s}) \end{bmatrix} \begin{bmatrix} \tau L_M \\ \tau^2 \end{bmatrix} \tag{4.8}$$

where the subscript 1, 2, ..., n denotes the n different simulations and the above matrix equation can be solved with a least-square method enabling L_M and R_R to be obtained. Inserting the obtained values into the real part

of (4.6), L_σ can be obtained. Furthermore, R_s is evaluated from the resistive losses in no-load operation (zero slip).

4.3.2 FEA-based per-solenoid analysis

The classical method described above analyzes electrical machines using the per-phase approach. It allows the analysis of balanced three-phase systems with the same effort as for a single-phase system, and by keeping the superposition of effects, other phases are computed accordingly. A per-solenoid analysis is extensively discussed in [7]. The per-solenoid dynamic model of the induction machine used for this analysis is reported in (4.9), which later is solved by the FEA.

$$\begin{bmatrix} V_s \\ V_r \end{bmatrix} = \begin{bmatrix} R_s & \frac{dL_{sr}}{dt} \\ \frac{dL_{rs}}{dt} & R_r \end{bmatrix} \begin{bmatrix} I_s \\ I_r \end{bmatrix} + \begin{bmatrix} L_{ss} & L_{sr} \\ L_{rs} & L_{rr} \end{bmatrix} \begin{bmatrix} \frac{dI_s}{dt} \\ \frac{dI_r}{dt} \end{bmatrix} \tag{4.9}$$

where V_s is the stator coil voltage, V_r is the induced rotor voltage, L_{ss} is the stator self inductance matrix, L_{rr} is the rotor self inductance, L_{sr} is stator-rotor mutual inductance, L_{rs} is rotor-stator mutual inductance, R_s is the stator coil resistance, and R_r is the rotor resistance.

Each solenoid's stator flux linkage is complexly estimated in the frequency domain and calculated in the slots by integrating the magnetic vector potential in each solenoid:

$$\phi_s = \int_s \nabla \times A.\, ds = \oint A.\, dl \tag{4.10}$$

where A is the magnetic vector potential. Also from [83], the flux in the area spanned between two points $(x_1, y_1$ to $x_2, y_2)$ and extending up to the axial length of the machine can be computed as:

$$\phi_s = L_a[A(x_1, y_1) - A(x_2, y_2)] \tag{4.11}$$

where L_a represents the axial length in the direction normal to the x, y plane. An automatic FEA calculation is performed to calculate the parameters of the per-solenoid system in (4.9) according to the following procedure.

4.3.3 Computation of the mutual inductance, L_{sr}

The analysis considers a unity current in the one rotor bar and calculates the stator slot flux linkage using (4.11) for all stator slots. The calculation is repeated for all rotor bars. The results are stored in a matrix whose elements $L_{sr,x,y}$ represent the mutual inductance between solenoid x and rotor bar y. Once the first element $L_{sr,11}(\theta_r)$ is computed, other elements of the matrix can be easily obtained using symmetry considerations [7]. The elements are a function of the rotor position θ_r, as reported in the matrix (4.12).

$$L_{sr}(\theta_r) = \begin{bmatrix} L_{1,1}(\theta_r - 0\frac{2\pi}{Q_s}) & L_{1,1}(\theta_r + 1\frac{2\pi}{Q_r} - 0\frac{2\pi}{Q_s}) & \dots & L_{1,1}(\theta_r + (Q_r - 1)\frac{2\pi}{Q_r} - 0\frac{2\pi}{Q_s}) \\ L_{1,1}(\theta_r - 1\frac{2\pi}{Q_s}) & L_{1,1}(\theta_r + 1\frac{2\pi}{Q_r} - 1\frac{2\pi}{Q_s}) & \dots & L_{1,1}(\theta_r + (Q_r - 1)\frac{2\pi}{Q_r} - 1\frac{2\pi}{Q_s}) \\ \vdots & \vdots & \vdots & \vdots \\ L_{1,1}(\theta_r - (Q_s - 1)\frac{2\pi}{Q_s}) & L_{1,1}(\theta_r + 1\frac{2\pi}{Q_r} - (Q_s - 1)\frac{2\pi}{Q_s}) & \dots & L_{1,1}(\theta_r + (Q_r - 1)\frac{2\pi}{Q_r} - (Q_s - 1)\frac{2\pi}{Q_s}) \end{bmatrix} \tag{4.12}$$

Given the matrix L_{sr}, the value of L_{rs} is obtained by symmetry considerations:

$$L_{rs} = L_{sr}^{T} \tag{4.13}$$

4.3.4 Computation of the stator self-inductance, L_{ss}

This parameter is computed by energizing the internal coil of a stator slot with a unity positive current and the corresponding external stator coil of the same slot in the VPPIMs with the opposing negative current [7]. The flux linkage (4.11) is computed for all stator slots following the geometrical definitions of Figure 4.3(a) and (b).

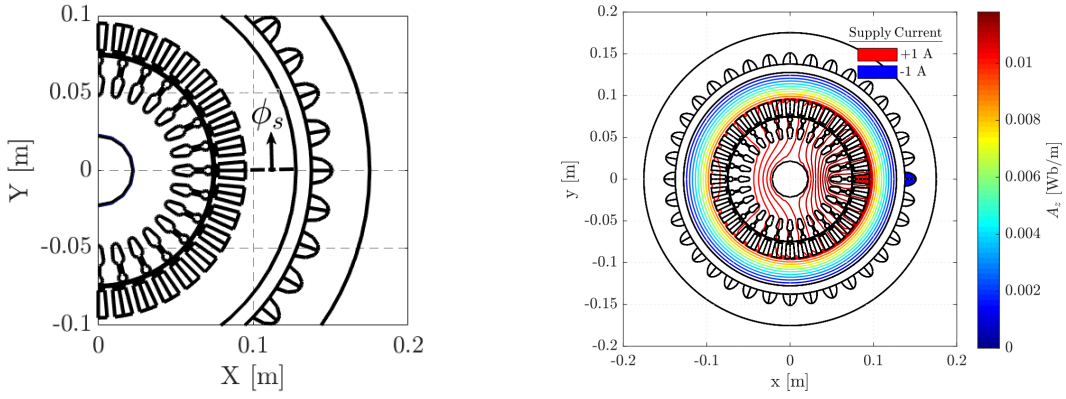

(a) **(b)**

Figure 4.3: (a) Geometrical definitions for L_{ss}. (b) A_z, induced in stator slot 1.

4.3.5 Computation of the rotor self-inductance, L_{rr}

Similarly to the case of L_{ss}, a rotor bar is provided with a unity positive current. However, this is not enough to define a current loop as the current provided is required to return somewhere. Therefore, it is assumed that the shaft will handle the return negative current. This assumption is based on the consideration that in normal operating conditions, the currents in the rotor bars have a zero-sum. The addition of virtual coils with a corresponding negative rotor bar current flowing in the shaft will also have a zero-sum, thus not contributing to the flux density in the rotor lamination [7]. The FEA calculations are then performed as in the L_{ss} case, following the geometrical definitions of Figure 4.4(a) and (b).

4.3.6 Computation of the stator resistance, R_s

The resistance of the stator coils is calculated using the n_s series of turn resistances with the assumption of ambient temperature [7].

$$R_s = n_s R_{turn} = n_s \left(\rho_{Cu} \frac{2L_a}{S_{cond}} \right) \tag{4.14}$$

where R_{turn} is the resistance of one turn, L_a is the length of the machine lamination stack, ρ_{Cu} is the resistivity of the copper wire, and S_{cond} is the total cross-sectional area of the stator conductors.

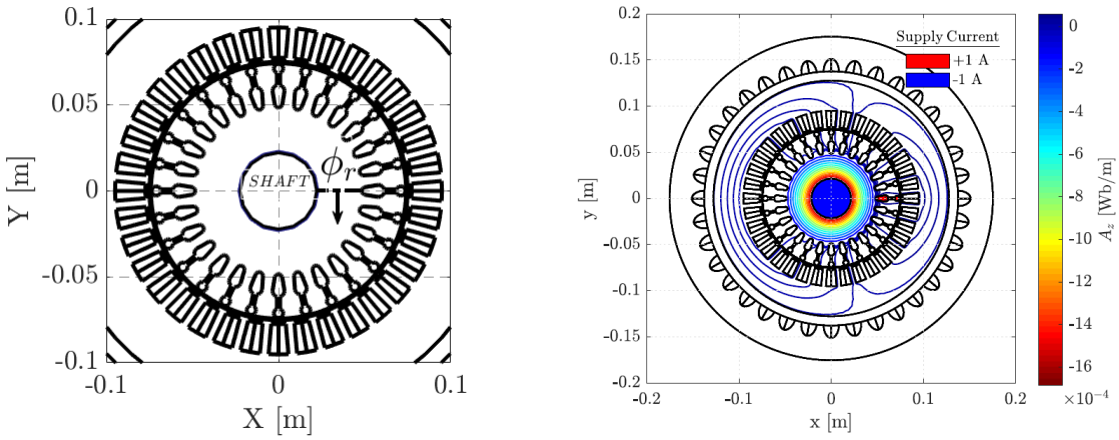

(a) **(b)**

Figure 4.4: (a) Geometrical definitions for L_{rr}. (b) A_z, induced in rotor bar 1.

4.3.7 Computation of the rotor resistance, R_r

The total equivalent rotor resistance is calculated considering the rotor bars' actual resistance and the end rings' resistance [83].

$$R_r = R_b + \frac{R_{er}}{2sin^2\left(\frac{p\pi}{Q_r}\right)} \tag{4.15}$$

where R_b is the actual resistance of the rotor bar and calculated by:

$$R_b = \rho_{Al}\left(\frac{l_b}{bd}\right) \tag{4.16}$$

where ρ_{Al} is the resistivity of aluminum, l_b is the length of one rotor bar, b is the equivalent bar width, and d is the equivalent bar depth of the rotor, and R_{er} is the resistance of the end-ring portion over one rotor slot pitch:

$$R_{er} = \rho_{Al}\left(\frac{\tau_p}{t_{be}d_{be}}\right) \tag{4.17}$$

where τ_p is the tooth pitch at the middle of the air gap, t_{be} is the end-ring width, and d_{be} is the end-ring depth. It is interesting to remark that the equivalent rotor bar resistance depends on the number of magnetic poles. In the next subsections, the transformation used in the HPD theory is applied to all motor parameters. As an extension of VSD, harmonic plane decomposition theory aims to unify the Clarke transformation with respect to all possible phase-pole configurations in a fixed number of orthogonal harmonic planes. In HPD, the lumped parameters computed in FEA are transformed into parameters of an equivalent circuit model based on the physical winding arrangement of the VPPIMs and following a similar transformation sequence to the VSD technique. In [17] and [18], the HPD transformation technique used for the different odd and even base-case scenarios of the pole-pair configurations is elaborated.

4.3.8 Parameter transformation in 123 reference frame

The foundational instances utilize mechanical angles instead of electrical ones, and the matrix for transformation $T_{abc\rightarrow 123}$ is contingent on the pole-pair count p. For instance, the transformation matrices when $p = 1, 2$ are presented in (4.18). In this context, I_m denotes an identity matrix and 0 represents a zero matrix with a rank of

m. Consequently, the matrix $T_{abc\rightarrow 123}$, possesses dimensions of $m_{b,o} \times 2m_{b,o} = 2m_{b,e} \times 4m_{b,e} = 18 \times 36$ in both foundational instances [18].

$$T_{abc\rightarrow 123}(p_{b,o}) = \begin{bmatrix} I_{m_{b,o}} & -I_{m_{b,o}} \end{bmatrix} \qquad T_{abc\rightarrow 123}(p_{b,e}) = \begin{bmatrix} I_{m_{b,e}} & -I_{m_{b,e}} & 0 & 0 \\ 0 & 0 & -I_{m_{b,e}} & I_{m_{b,e}} \end{bmatrix} \tag{4.18}$$

Compared to the conventional $\alpha\beta$ and dq transform theory for three-phase machines, the VSD requires an additional intermediate reference frame, which is indicated as the 123 frame or fundamental reference frame [84]. In this frame, the equivalent quantities of the practical abc frame, which are the solenoid-based parameters from FEA simulations, will be transformed into the machine coil parameters.

The fundamental winding configuration in the 123 frame has the phases shifted by $[\pi/m]$, with m as the number of phases. Consequently, the machine symmetry is changed from a two-pole symmetry to a one-pole symmetry. In this way, the components distributed over $[\pi]$ electric degrees allow the description of variable phase-pole machines in a generalized form [7]. The underlying equations show the parameter transformations in this frame.

$$\left.\begin{aligned} L_{ss,123} &= [T_{abc\rightarrow 123}][L_{ss}][T_{abc\rightarrow 123}]^T \\ L_{rs,123} &= [L_{rs}][T_{abc\rightarrow 123}]^T \\ L_{sr,123} &= [T_{abc\rightarrow 123}][L_{sr}] \\ L_{rr,123r} &= [L_{rr}] \\ R_{b,123r} &= [R_b] \\ R_{er,123r} &= [R_{er}] \\ R_{s,123} &= [T_{abc\rightarrow 123}][R_s][T_{abc\rightarrow 123}]^T \end{aligned}\right\} \tag{4.19}$$

where $[L_{ss}]$ is the stator self inductance matrix, $[L_{rr}]$ is the rotor self inductance matrix, $[L_{sr}]$ is stator-rotor mutual inductance matrix, $[L_{rs}]$ is rotor-stator mutual inductance matrix, $[R_b]$ is the rotor bar resistance matrix, $[R_{er}]$ is the rotor end-ring resistance matrix, and $[T_{abc\rightarrow 123}]$ is the transformation matrix from the practical frame to the 123 frame.

4.3.9 Parameter transformation in stationary reference frame

Here a generalized Clarke transform that considers m-phase systems and a one-pole symmetry is used. The 123 fundamental reference frame parameters are transformed into the stationary $\alpha\beta$ reference frame following the indications of [17], [18]. Additionally, the number of turns N_s is used as a coupling factor between the stator

and the rotor sides. The transformed parameters are represented in the next set of equations.

$$\left.\begin{aligned}
L_{ss,\alpha\beta} &= [T_{123\to\alpha\beta}][L_{ss,123}][T_{\alpha\beta\to 123}] \\
L'_{rs,\alpha\beta} &= N_s[T_{123r\to\alpha\beta}][L_{rs,123}][T_{\alpha\beta\to 123}] \\
L_{sr,\alpha\beta} &= \frac{2N_s m_b}{Q_r}[T_{123\to\alpha\beta}][L_{sr,123}][T_{\alpha\beta\to 123r}] \\
L'_{rr,\alpha\beta} &= \frac{4N_s^2 m_b}{Q_r}[T_{123r\to\alpha\beta}][L_{rr,123r}][T_{\alpha\beta\to 123r}] \\
R'_{b,\alpha\beta} &= \frac{4N_s^2 m_b}{Q_r}[T_{123\to\alpha\beta}][R_{b,123}][T_{\alpha\beta\to 123r}] \\
R'_{er,\alpha\beta} &= \frac{4N_s^2 m_b}{Q_r}[T_{123\to\alpha\beta}][R_{er,123}][T_{\alpha\beta\to 123r}] \\
R_{s,\alpha\beta} &= [T_{123\to\alpha\beta}][R_{s,123}][T_{\alpha\beta\to 123}]
\end{aligned}\right\} \tag{4.20}$$

where $[T_{123\to\alpha\beta}]$ is the transformation matrix from 123 to $\alpha\beta$ frame, and $[T_{123r\to\alpha\beta}]$ is the transformation matrix of the rotor side from 123 to $\alpha\beta$ frame referred to the stator side. From the orthogonality property of the transformation matrix in the $\alpha\beta$ frame, each parameter is extracted from the diagonal elements of the transformed matrices in the T-equivalent model [7].

As described in [83], the magnetizing inductance is extracted from the peak values of the coupling inductance over the air gap circumference of the VPPIMs. This is due to the maximum force exerted on the rotor which is reached when the peak values of the magnetic flux density and surface current waves are coincident:

$$L_m = max(diag(L_{sr,\alpha\beta}(\theta))) = max(diag(L_{rs,\alpha\beta}(\theta))) \tag{4.21}$$

The leakage inductance is then calculated from magnetizing and self-inductance by using:

$$L_{\sigma,s} = diag(L_s) - L_m \qquad L'_{\sigma,r} = diag(L'_r) - L_m \tag{4.22}$$

The resistances of the stator and rotor sides are also calculated from the diagonal elements of the matrix with:

$$R_{s,HPD} = diag(R_s) \qquad R'_{r,HPD} = diag(R'_r) \tag{4.23}$$

Although the T-equivalent dynamic model is physically relevant, it is less good for dynamic analysis and controller design because it is over parameterized. The transformation factor $[b = L_m/L_r]$ of the induction machine equivalent circuit lumps the stator and rotor leakage inductance into a total leakage inductance L_σ that appears on the stator side only. Hence, the mutual and leakage inductances are scaled as:

$$L_M = bL_m \qquad L_\sigma = L_s - L_M \tag{4.24}$$

The stator and rotor side resistances are scaled in the inverse-Γ model as:

$$R_s = R_{s,HPD} \qquad R_R = b^2 R'_{r,HPD} \tag{4.25}$$

In general, and similarly to the VSD approach, each harmonic plane in the machine model is represented with a T-equivalent or an inverse$-\Gamma$ model in the $\alpha\beta 0$ or $dq0$ reference frame [17]. The parameters used in VSD and

HPD are however different. For the sake of clarity, [81] elaborates on the parameter equivalence between the VSD and HPD techniques.

4.4 Simulation Results

This section compares the parameters identified with classical methods and the HPD theory methods. All simulations are performed at fundamental excitation only. The VPPIM is configured as a $[m = 3, p = 2]$ and $[m = 9, p = 2]$ motor.

4.4.1 Inductance results from the per-phase analysis

The magnetic field distribution under no-load operation for 3-phase/2-pole pair and 9-phase/2-pole pair configurations of the VPPIMs are shown in Figure 4.5 and 4.6, respectively. The contour lines represent the magnetic vector potential, and the surface plot is the magnetic flux density distribution. The magnetic field

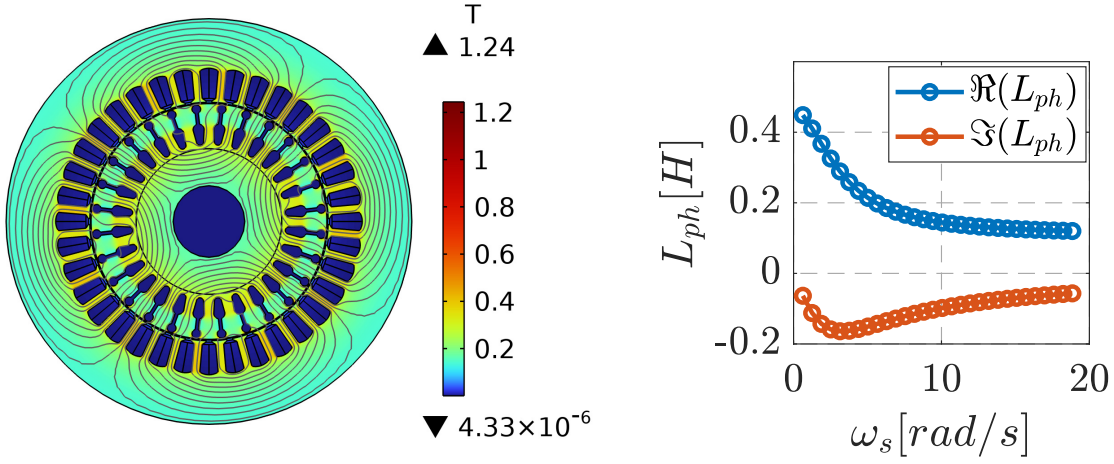

(a) **(b)**

Figure 4.5: (a) Magnetic field density distribution for a 3-phase/2-pole pair VPPIMs. (b) Per-phase inductance plots for a 3-phase/2-pole pair VPPIMs.

distribution under no-load operation for 3-phase/2-pole pair and 9-phase/2-pole pair configurations of the VPPIMs are shown in Figure 4.5 and 4.6, respectively. The contour lines represent the magnetic vector potential, and the surface plot is the magnetic flux density distribution. The maximum values of the magnetic field density are obtained with a magnitude of B_{max}=1.24 [T] for three-phase and B_{max}=1.29 [T] for nine-phase configuration, at the excitation current level of 1 A. Furthermore, Figure 4.5(a) and (b) depict the real and imaginary parts of the phase inductance for the 3-phase/2-pole pair and 9-phase/2-pole pair configurations, respectively. The dependence of phase inductance on slip frequency provides a mechanism for identifying motor parameters using linear least-squares regression methods. The maximum values of the magnetic field density are obtained with a magnitude of B_{max}=1.24 [T] for three-phase and B_{max}=1.29 [T] for nine-phase configuration, at the excitation current level of 1 A.

Furthermore, Figure 4.6(a) and (b) depict the real and imaginary parts of the phase inductance for the 3-phase/2-pole pair and 9-phase/2-pole pair configurations, respectively. The dependence of phase inductance on slip frequency provides a mechanism for identifying motor parameters using linear least-squares regression methods.

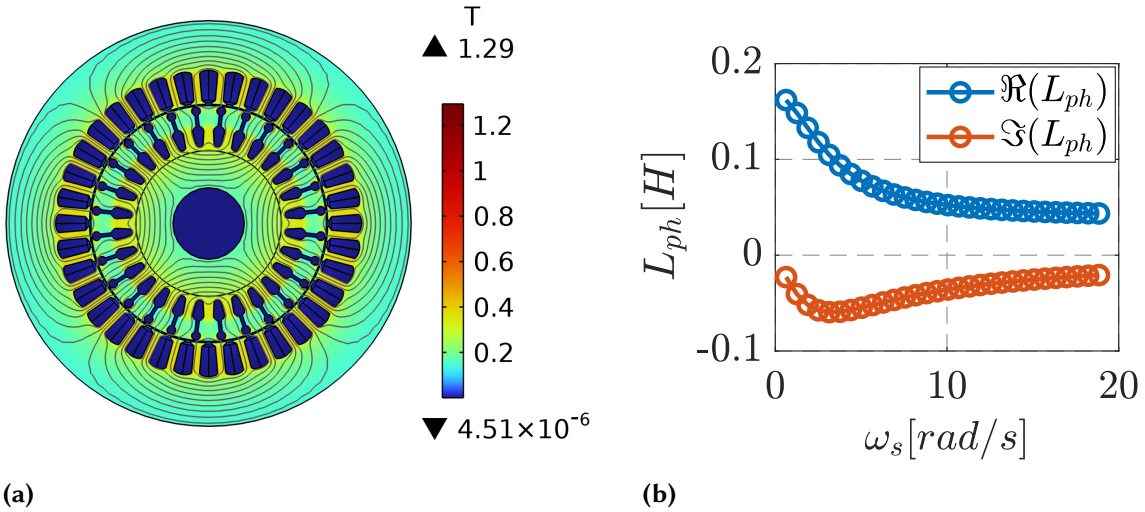

(a) **(b)**

Figure 4.6: (a) Magnetic field density distribution for a 9-phase/2-pole pair VPPIMs. (b) Per-phase inductance plots for a 9-phase/2-pole pair VPPIMs.

4.4.2 Inductance results from the per-solenoid analysis

The results confirm that mutual inductance for coils close to an exciting coil is higher and gradually decreases and reaches a minimum when the coils oppose the exciting coil. Then, all transformation sequences are implemented as described in equations (4.19) and (4.20). The simulation results for the coupling inductance between the first stator slot and the first rotor bar in the 2D plot are shown in Figure 4.7.

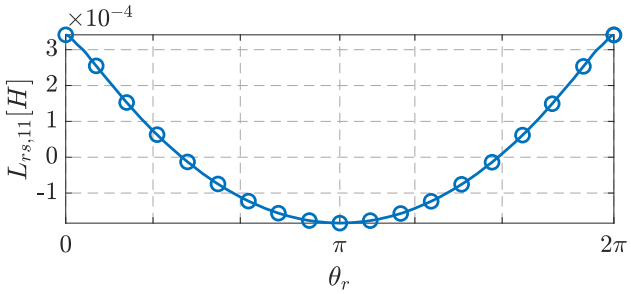

Figure 4.7: 2D Plot for L_{rs} in per-solenoid analysis.

Additionally, the four inductance matrices, L_{ss}, L_{sr}, L_{rs}, and L_{rr} in the HPD method are displayed in a 3D format in surface and mesh plots illustrated in Figure 4.8 and 4.9, respectively. When the inductances are computed, the maximum values from the inductance plots are typically taken. These inductances represent the self and mutual inductances in a system, such as coupled inductors. L_{ss} and L_{rr} are the self-inductances of the stator and rotor, respectively, while L_{sr} and L_{rs} are the mutual inductances between the stator and rotor. By extracting the maximum values from the inductance plots, the highest possible interaction or coupling between the components at any given operating condition is accounted for. This method ensures that the maximum inductive behavior is considered, which is useful for designing systems with reliable performance and ensuring that peak inductance values can be handled under various conditions. The maximum values are critical in evaluating the energy storage and magnetic flux linkages in the system.

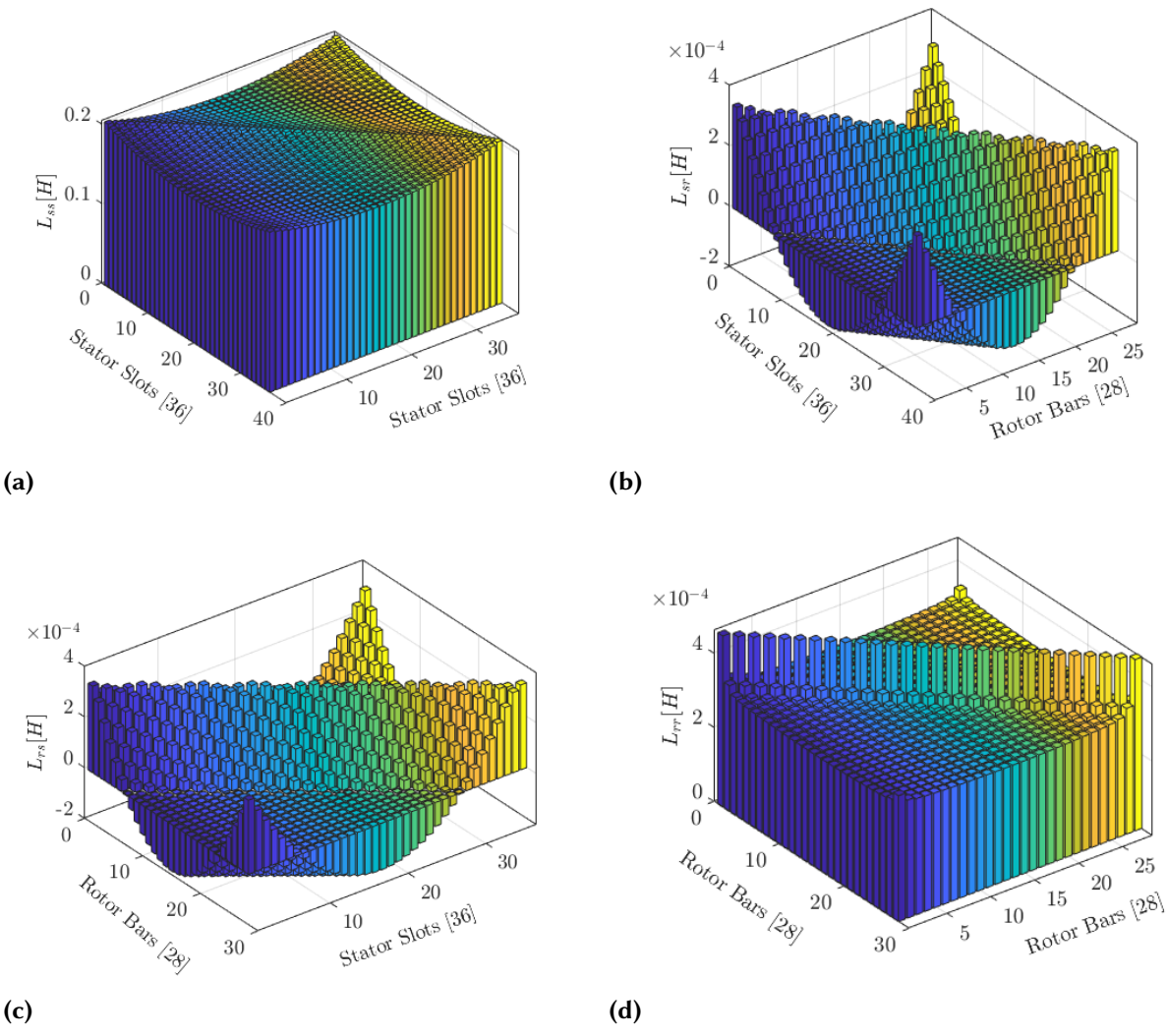

Figure 4.8: 3D inductance matrix surface plot in per−solenoid analysis: (a) L_{ss} (b) L_{sr} (c) L_{rs} (d) L_{rr}

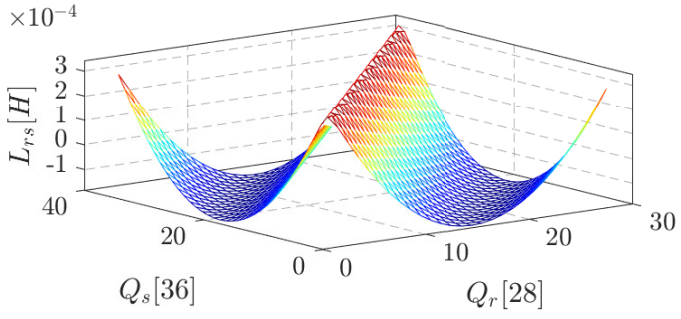

Figure 4.9: 3D mesh Plot for L_{rs} in per−solenoid analysis.

4.5 Experimental Verification

The purpose of this section is to compare the agreement of the results from the methods discussed so far using experimental measurements. The experimental test bench is shown in Figure B.1, where the VPPIMs is powered by a 36-leg inverter and a control board composed of a Xilinx ZynQ-7000 SoC ZC706 board.

For experimental validation, the methods are compared to the results obtained from standard no-load (NL) and locked-rotor (LR) tests on the VPPIMs configured as a $[m = 3, p = 2]$ and $[m = 9, p = 2]$ motor. To create a specific phase belt, the currents in the same belt are controlled with the same phase and magnitude, reproducing the desired phase-pole configuration without the need for a mechanical reconnection. The load machine of Figure B.1 is not used in this case. The procedure and equipment used to perform the tests for the VPPIMs in $[m = 3, p = 2]$ configuration are described in [85]. For the $[m = 9, p = 2]$ configuration, a nine-phase inverter was used in both tests.

The NL test was conducted by turning the shaft with a prime mover at close to synchronous speed ($\lesssim$ 1193 rpm). NL curves were captured to determine $L_{\sigma,s}$ and the unsaturated L_m for each configuration using the s.c. the indirect method in [85]. The LR tests were conducted at a frequency of 10 Hz to mitigate the skin effect, and the voltage was gradually increased until the rated current was reached. Currents were recorded using isolated LEM sensors. The inverter's IGBTs were characterized to compensate for the voltage drop across the switching elements due to current conduction and dead time. These compensated values were used as data points for the voltages.

4.5.1 Estimation of L_M and L_σ for 3-phase/2-pole pair machine.

As can be seen in Table 4.2, the difference between L_M obtained from the classical method and from the measurement is approximately 22 %. The HPD approach performs better with an error of 15 %. The difference between L_σ obtained by the classical method and the measurement is 62 %, which is an overestimated value. Comparing the results obtained from the HPD theory, the difference in leakage inductance is 36 %, again improved. Both FEA simulations may further improve the estimation by adding effects like the rotor skewing, the non-linear behavior of the leakage inductance due to the thin bridges that close the rotor bars, the presence of aluminum in the stator frame where the external coils are accommodated, and the leakage of harmonic magnetic fields in addition to the fundamental only. According to reference [73], analytical computations are carried out. The analytical approach is somewhat inconsistent with the practical results, although it is close to the conventional approach.

4.5.2 Estimation of R_s and R_R for 3-phase/2-pole pair machine.

From Table 4.2, the absolute error of the stator resistances obtained from the two methods is 0.3 Ω, and 0.2 Ω for the classical and HPD methods, respectively. The estimation of R_R for the classical and HPD methods is reflected in 0.4 Ω, and 0.3 Ω, respectively. The result reveals that the stator and rotor resistance estimation in the HPD method is in excellent agreement with the practical measurements. Additionally, estimates made using analytical and HPD approaches are close.

4.5.3 Estimation of L_M and L_σ for 9-phase/2-pole pair machine.

As it can be seen from the data in Table 4.3, the relative error between L_M obtained as output from the classical method and L_M obtained using practical measurement is approximately 17 %. However, comparing HPD output with the measured value of L_M, the difference becomes only 6 %. The difference between L_σ obtained in the

Table 4.2: The proposed methods and practical results for a 3-phase/2-pole pair VPPIM

Parameters	Analytical	Per-phase	Per-sol.	Meas.	$\varepsilon_{r,A}[\%]$	$\varepsilon_{r,Pp}[\%]$	$\varepsilon_{r,Ps}[\%]$
$L_M[mH]$	333	330	484	422	21	22	-15
$L_\sigma[mH]$	116	112	44	69	-68	-62	36
Parameters	Analytical	Per-phase	Per-sol.	Meas.	$\varepsilon_{a,A}[\Omega]$	$\varepsilon_{a,Pp}[\Omega]$	$\varepsilon_{a,Ps}[\Omega]$
$R_s[\Omega]$	3.55	3.5	3.6	3.8	0.25	0.3	0.2
$R_R[\Omega]$	1.8	1.1	1.8	1.5	0.3	0.4	0.3

- where: $[\varepsilon_{r,Pp}]$ and $[\varepsilon_{a,Pp}]$, are the relative and absolute error for the per-phase analysis, respectively, $[\varepsilon_{r,Ps}]$ and $[\varepsilon_{a,Ps}]$, are the relative and absolute error for the per-solenoid analysis, respectively, and $[\varepsilon_{r,A}]$ and $[\varepsilon_{a,A}]$, are the relative and absolute error for the analytical computation, respectively.

classical method and the leakage inductance obtained in the measurement is 54 %. Comparing the results of L_σ obtained from the HPD theory to those from the practical measurements, the difference in leakage inductance is only 23 %. Again, this accuracy may be further improved with the adoption of more sophisticated simulations as suggested in Section 4.5.1. Based on reference [73], analytical computations are performed. The analytical result shows a discrepancy from the practical results but is close to the conventional approach.

4.5.4 Estimation of R_s and R_R for 9-phase/2-pole pair machine.

From Table 4.3, the absolute error of the stator resistances obtained from the two methods is 0.06 Ω. The estimation of R_R for the classical and HPD methods results in 0.2 Ω, and 0.06 Ω, respectively. In general, the result reveals that the stator and rotor resistance estimation in the HPD method is again in excellent agreement with the practical measurements. Additionally, estimates made using analytical and HPD approaches are close.

Table 4.3: The proposed methods and practical results for a 9-phase/2-pole pair VPPIM

Parameters	Analytical	Per-phase	Per-sol.	Meas.	$\varepsilon_{r,A}[\%]$	$\varepsilon_{r,Pp}[\%]$	$\varepsilon_{r,Ps}[\%]$
$L_M[mH]$	118	118	152	143	17	17	-6
$L_\sigma[mH]$	42	40	20	26	-61	-54	23
Parameters	Analytical	Per-phase	Per-sol.	Meas.	$\varepsilon_{a,A}[\Omega]$	$\varepsilon_{a,Pp}[\Omega]$	$\varepsilon_{a,Ps}[\Omega]$
$R_s[\Omega]$	1.18	1.2	1.2	1.26	0.08	0.06	0.06
$R_R[\Omega]$	0.66	0.4	0.66	0.6	0.06	0.2	0.06

- where: $[\varepsilon_{r,Pp}]$ and $[\varepsilon_{a,Pp}]$, are the relative and absolute error for the per-phase analysis, respectively, $[\varepsilon_{r,Ps}]$ and $[\varepsilon_{a,Ps}]$, are the relative and absolute error for the per-solenoid analysis, respectively, and $[\varepsilon_{r,A}]$ and $[\varepsilon_{a,A}]$, are the relative and absolute errors for the analytical computation, respectively.

4.5.5 Computational effort

In this work, Comsol Multiphysics and Intel(R) Core(TM) i7-8665U CPU with 16GB RAM are the software and hardware platforms for the FEA simulations, respectively. The FEA per-solenoid simulation requires 59 minutes to complete, and it is all we need to populate the HPD model and, if necessary, all the equivalent VSD models for all phase-pole configurations. On the other hand, the FEA per-phase simulation requires only 53 minutes for a specific phase-pole arrangement, but it must be repeated for each phase-pole configuration. In the machine used in this work, there are nine possible phase-pole configurations, for a total simulation time of $9 \cdot 53 = 477$ minutes, which is a significant increase.

4.6 Summary

This work discusses the advantages and challenges of using VPPIMs in applications requiring a wide torque-speed range, such as electromobility. It highlights that VPPIMs can change their number of pole pairs in real-time, offering competitive efficiency without using magnets. However, modeling and controlling these machines require accurate knowledge of electrical parameters for all phase-pole configurations, which is more complex for multiphase machines than for three-phase machines. An offline parameter identification algorithm tailored for multiphase induction machines is proposed, focusing on accurate estimation through current injection in non-flux and non-torque-producing vector spaces. Traditional modeling using the VSD theory introduces discontinuities during real-time reconfiguration, whereas the proposed HPD theory mitigates this by using unified transformations across all configurations.

The HPD approach offers computational efficiency and improved accuracy in estimating parameters, validated through FEA and experimental methods. Compared to the classical method, the HPD-based technique demonstrates better agreement with practical measurements for stator and rotor resistances. However, some inaccuracies in leakage inductance remain due to simplifications in the simulation model. Overall, this study confirms the feasibility and advantages of the HPD theory for efficient and accurate parameter estimation in VPPIMs, emphasizing the potential for enhanced dynamic modeling and control in varied phase-pole configurations.

5 Sensorless Control of the VPPIM

This chapter describes the Sensorless-based Speed and Pole Transition Control for variable phase-pole induction machines. This section is based on papers II and IV.

5.1 Background

Variable phase-pole induction machines are a class of multiphase machines with great potential in the context of electromobility. These machines offer advantages like an expanded torque-speed range at a competitive torque density and efficiency due to their pole-change capabilities, a compact drive design, and the absence of rare-earth materials [5], [44], [71], [75]. Nevertheless, defining analytical VPPIM models, developing their control schemes, and estimating their electrical parameters can be challenging. Recent years have seen an increase in the number of publications on these topics, as documented in works such as [5], [71], [75], [86], [87]. One of the most critical aspects of this technology is related to the control of the smooth transition between different pole-pair configurations. Recently, some authors have addressed this problem by proposing various solutions to optimize the transitions [44], [88]–[90]. Still, there seems to be no available solution for the speed-sensorless control of VPPIMs, where the sensorless operation is also intended to persist during pole-pair configuration changes. Besides avoiding the use of speed sensors, thus reducing costs and enhancing fault tolerance, a working sensorless solution can also be used in combination with a speed sensor to enable the implementation of a redundant speed estimation, enhancing the reliability of the system, which is crucial for the rigorous safety standards in electromobility.

VPPIMs are inherently multiphase machines, and thus require multiphase sensorless algorithms as a base. In this field, model-based approaches have been explored, including MRAS based observers, Luenberger observers, and EKF [16], [60], [91]. Kalman filters are renowned for providing precise estimates of state variables in the presence of noise [92], [93]. High-frequency signal injection techniques are also used, leveraging the unique characteristics of multiphase induction drives and their harmonic planes [60], [94]. Implementing sensorless speed control using high-frequency signal injection requires careful design and tuning of the control system [60].

It is widely acknowledged that MRAS-based speed estimators are effective in high-speed conditions but may exhibit some degree of inaccuracy or instability in low-speed regions. The effectiveness of MRAS-based systems has led to their general acceptance as a solution for a wide range of speed requirements [95]–[97]. In the context of VPPIMs, where the pole reconfiguration is likely to happen at relatively high speeds, the use of a MRAS solution seems feasible, as long as the model used for the MRAS algorithm is unique and valid for any pole configuration, to ensure speed estimation even during a pole change. For this reason, the model that forms the basis for the MRAS-based approach developed in this paper is derived from the Harmonic Plane Decomposition (HPD) theory [5], [40], [98], [99]. The HPD approach enables the formulation of a model that remains constant in the number of equations and its parameter values for all possible pole configurations.

5.2 Mathematical Model of the VPPIM

The machine analyzed in this study is a nine-phase VPPIM with a 36-stator slot and with 18 full-pitch multi-turn independent coils phase shifted each other by π electrical radians as shown in Figure 5.1 [4]. This setting allows

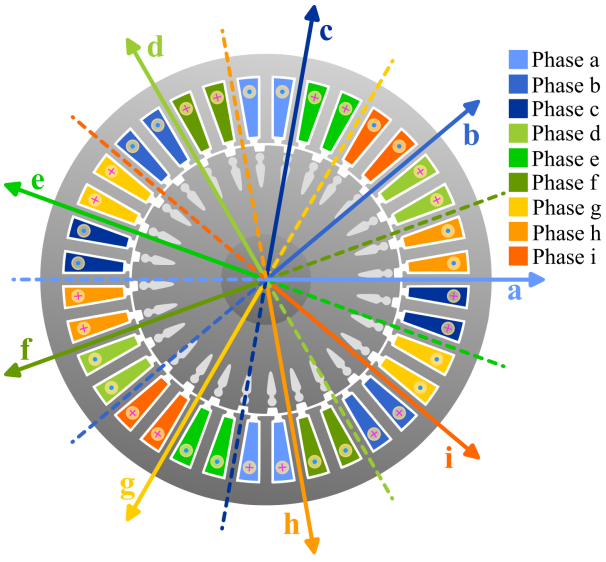

Figure 5.1: Windings connections of the symmetrical nine-phase IM with 36 stator slots and 18 coils.

four phase-pole configurations [100], but this paper focuses only on the two-pole and six-pole configurations. By applying the HPD theory [87] to the nine-phase induction machine, and assuming the linear behavior of the magnetic circuit, the mathematical dynamic model of the machine in the stationary reference frame can be written as follows:

$$\dot{\boldsymbol{x}}^{(h)} = \boldsymbol{A}^{(h)}\boldsymbol{x}^{(h)} + \boldsymbol{B}^{(h)}\boldsymbol{v}_s^{(h)} \tag{5.1}$$

$$\boldsymbol{y}^{(h)} = \boldsymbol{C}^{(h)}\boldsymbol{x}^{(h)} \tag{5.2}$$

The parameters in the state matrix $\boldsymbol{A}^{(h)}$, the input matrix $\boldsymbol{B}$ and the output matrix $\boldsymbol{C}^{(h)}$ need to be determined according to the HPD methods, as described in [99]. The state variables and parameters of the VPPIM, as defined by the inverse-Γ model, are defined as follows:

$$\left\{\boldsymbol{x}^{(h)} = \begin{bmatrix}\boldsymbol{\psi}_{s,\alpha\beta}^{(h)} \\ \boldsymbol{\psi}_{R,\alpha\beta}^{(h)}\end{bmatrix},\ \boldsymbol{y}^{(h)} = \begin{bmatrix}\boldsymbol{i}_{s,\alpha\beta}^{(h)}\end{bmatrix},\ \boldsymbol{v}_s^{(h)} = \begin{bmatrix}\boldsymbol{v}_{s,\alpha\beta}^{(h)}\end{bmatrix},\right. \tag{5.3}$$

$$\left\{\boldsymbol{A}^{(h)} = \begin{bmatrix}-\dfrac{1}{\tau_s^{(h)}}\boldsymbol{I} & \dfrac{1}{\tau_s^{(h)}}\boldsymbol{I} \\ \dfrac{(1-\sigma^{(h)})}{\tau_r^{(h)}}\boldsymbol{I} & -\dfrac{1}{\tau_r^{(h)}}\boldsymbol{I} + \omega_r^{(h)}\boldsymbol{J}\end{bmatrix},\right. \tag{5.4}$$

$$\left\{\begin{array}{l}\boldsymbol{B} = \begin{bmatrix}1 & 0\end{bmatrix},\ \boldsymbol{C}^{(h)} = \begin{bmatrix}\dfrac{1}{L_\sigma^{(h)}}\boldsymbol{I} & -\dfrac{1}{L_\sigma^{(h)}}\boldsymbol{I}\end{bmatrix},\ \boldsymbol{I} = \begin{bmatrix}1 & 0 \\ 0 & 1\end{bmatrix},\ \boldsymbol{J} = \begin{bmatrix}0 & -1 \\ 1 & 0\end{bmatrix}, \\ \sigma^{(h)} = \dfrac{L_\sigma^{(h)}}{L_M^{(h)} + L_\sigma^{(h)}},\quad \tau_s^{(h)} = \dfrac{L_\sigma^{(h)}}{R_s},\quad \tau_r^{(h)} = \sigma^{(h)}\dfrac{L_M^{(h)}}{R_R^{(h)}}\end{array}\right. \tag{5.5}$$

Furthermore, the total electromagnetic torque resulting from the sum of the contributions of all harmonic planes of the VPPIM can be expressed as follows:

$$\tau_e = \frac{m}{2} \sum_{h=1}^{h=\zeta} \frac{p^{(h)}}{L_\sigma^{(h)}} \Im \left\{ \boldsymbol{\psi}_{s,\alpha\beta}^{(h)} \boldsymbol{\psi}_{R,\alpha\beta}^{*(h)} \right\} \tag{5.6}$$

where h is the harmonic plane order, $h \in \{1, 3, 5, 7..., \zeta\}$

5.3 Proposed Adaptive Observer Design

The proposed sensorless control system is based on an MRAS solution that relies on an adaptive observer to estimate the rotor speed and position. This information is then used in a conventional field-oriented control algorithm, under the results of [16], [91]. However, in contrast to [91], two observers are designed in two separate harmonic planes h (the first and the third ones). Their stability is proven using the Lyapunov theory and a linearization of the non-linear models. Subsequently, a method for estimating the speed during pole transition combining the outputs of the two parallel observers is proposed. From a stability standpoint, the estimation remains stable and enables a simple and effective sensorless operation.

It is also worth noting before analyzing the observers that VPPIMs are likely to operate on a single pole pair configuration at any instant except during pole transition. The transition, which is usually dictated by loss minimization considerations [101],[102], never happens at near-zero frequency but rather at significant speeds. During operation at low-to zero frequencies, that is, where he model-based sensorless solutions start to experience observability issues the VPPIM will operate with a high pole number count, to deliver high torque. In such a situation, MRAS algorithms used to estimate its mechanical speed are no different than the ones used for traditional three-phase or multi- phase machines that do not change the number of poles. The same rules on observability apply, and the same results apply [103].

Similar considerations can be applied to the operation at high speeds, where the VPPIM is likely to operate as a machine with a low pole number count. The same observability and stability considerations of three-phase or multi-phase machines can be imported. The key is the operation during pole transition, where multiple harmonics appear and produce torque in the machine.

5.3.1 The Observer and the Speed Adaptation Law

The mathematical formulation of the state-space model for each harmonic plane h in the VPPIM is reported here below, following a similar notation given in [91].

$$\hat{\boldsymbol{x}}^{(h)} = \hat{A}^{(h)} \hat{\boldsymbol{x}}^{(h)} + \boldsymbol{B} v_s^{(h)} + \boldsymbol{K}^{(h)} \left[\boldsymbol{i}_s^{(h)} - \hat{\boldsymbol{i}}_s^{(h)} \right] \tag{5.7}$$

$$\hat{\boldsymbol{i}}_s^{(h)} = \boldsymbol{C}^{(h)} \hat{\boldsymbol{x}}^{(h)} \tag{5.8}$$

Also, the estimated state variable input matrix $\boldsymbol{A}^{(h)}$ is defined by:

$$\hat{A}^{(h)} = \begin{bmatrix} \frac{-1}{\tau_s^{(h)}} \boldsymbol{I} & \frac{1}{\tau_s^{(h)}} \boldsymbol{I} \\ \frac{1 - \sigma^{(h)}}{\tau_r^{(h)}} \boldsymbol{I} & \frac{-1}{\tau_r^{(h)}} \boldsymbol{I} + \hat{\omega}_r^{(h)} \boldsymbol{J} \end{bmatrix} \tag{5.9}$$

By giving the observer gain matrix $\boldsymbol{K}^{(h)}$ a specific form, the adaptive law can be accomplished and extended

to other harmonic planes h. The observer gain $\boldsymbol{K}^{(h)}$ is defined as:

$$\boldsymbol{K}^{(h)} = Q\begin{bmatrix} \boldsymbol{I} & + & sign(\hat{\omega}_r^{(h)})\boldsymbol{J} \\ -\boldsymbol{I} & + & sign(\hat{\omega}_r^{(h)})\boldsymbol{J} \end{bmatrix} \tag{5.10}$$

where

$$Q = \begin{cases} z\dfrac{|\hat{\omega}_r^{(h)}|}{\omega} & \text{if } |\hat{\omega}_r^{(h)}| < \omega \\ z & \text{if } |\hat{\omega}_r^{(h)}| \geq \omega \end{cases}$$

where z and ω are positive constants and can be selected based on the linearized model. In this work, the observer gain is set to $z = 10\ \Omega$ and $\omega = 1$ p.u., where the base value of the angular frequency is set to $2\pi \cdot 50$ rad/s. The parameters Q and z serve as impedances and vary depending on the motor power levels [91]. The block scheme of the proposed adaptive full-order flux linkage and speed observer in the stationary frame is depicted in Figure 5.2. The speed adaptation law is still derived using the Lyapunov stability theory as in [16],

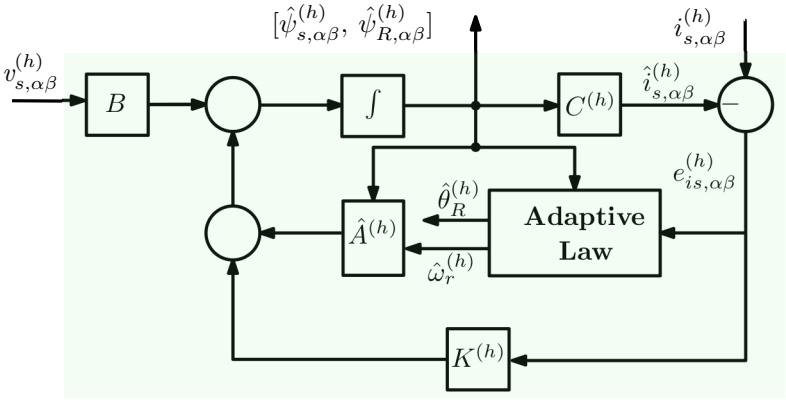

Figure 5.2: Block diagram of the proposed MRAS observer for a single harmonic plane h. Two of them are used in parallel for a VPPIM switching between two pole configurations.

but applied for each harmonic plane. The time derivative of the error function $\boldsymbol{e}$ of the observer is defined by:

$$\dot{\boldsymbol{e}}^{(h)} = (\boldsymbol{A}^{(h)} - \boldsymbol{K}^{(h)}\boldsymbol{C}^{(h)})\boldsymbol{e}^{(h)} + \Delta\boldsymbol{A}^{(h)}\begin{bmatrix} \hat{\boldsymbol{\psi}}_s \\ \hat{\boldsymbol{\psi}}_R \end{bmatrix} \tag{5.11}$$

where

$$\begin{cases} \boldsymbol{e}^{(h)} = \boldsymbol{x}^{(h)} - \hat{\boldsymbol{x}}^{(h)} \\ \Delta\boldsymbol{A}^{(h)} = \boldsymbol{A}^{(h)} - \hat{\boldsymbol{A}}^{(h)} = \begin{bmatrix} 0 & 0 \\ 0 & -\Delta\omega_r^{(h)}\boldsymbol{J} \end{bmatrix} \\ \Delta\omega_r^{(h)} = \omega_r^{(h)} - \hat{\omega}_r^{(h)} \end{cases}$$

The candidate Lyapunov function $V^{(h)}$ in the harmonic plane h is defined by:

$$V^{(h)} = \boldsymbol{e}_n^{(h)T}\boldsymbol{e}_n^{(h)} + \frac{(\omega_r^{(h)} - \hat{\omega}_r^{(h)})^2}{\lambda} \tag{5.12}$$

where λ is a positive constant.

$$\boldsymbol{e}_n^{(h)} = [\boldsymbol{i}_s^{(h)} - \hat{\boldsymbol{i}}_s^{(h)}\ \ \boldsymbol{\psi}_R^{(h)} - \hat{\boldsymbol{\psi}}_R]^T = [\boldsymbol{e}_{is}^{(h)}\ \ \boldsymbol{e}_{\psi_R}^{(h)}]^T = \boldsymbol{\gamma}^{(h)}\boldsymbol{e}^{(h)} \tag{5.13}$$

where $\boldsymbol{\gamma}^{(h)}$ is a non-singular matrix. For the poles to be stable, the H (Hermitian) matrix of (5.14) should be negative semidefinite. The unidentified parameter (ω_r) is taken into account as a constant for the derivation of the adaptive mechanism. Then, the time derivative of V is expressed as a function of the observer trajectories, as in (5.14).

$$\dot{V}^{(h)} = \boldsymbol{e}_n^{(h)T} \underbrace{\{[\boldsymbol{\gamma}(\boldsymbol{A}^{(h)} - \boldsymbol{K}^{(h)}\boldsymbol{C}^{(h)})\boldsymbol{\gamma}^{-1}]^T + [\boldsymbol{\gamma}(\boldsymbol{A}^{(h)} - \boldsymbol{K}^{(h)}\boldsymbol{C}^{(h)})\boldsymbol{\gamma}^{-1}]\}}_{\boldsymbol{H}} \boldsymbol{e}_n^{(h)} + \underbrace{\hat{\boldsymbol{x}}^{(h)T}\Delta\boldsymbol{A}^{(h)T}\boldsymbol{\gamma}^T\boldsymbol{e}_n^{(h)} + \boldsymbol{e}_n^{(h)T}\boldsymbol{\gamma}\Delta\boldsymbol{A}^{(h)}\hat{\boldsymbol{x}}^{(h)}}_{\frac{2\Delta\omega_r^{(h)}}{L_\sigma^{(h)}}[\hat{\boldsymbol{\psi}}_{R,\beta}^{(h)}\boldsymbol{e}_{is,\alpha}^{(h)} - \hat{\boldsymbol{\psi}}_{R,\alpha}^{(h)}\boldsymbol{e}_{is,\beta}^{(h)}]} - \frac{2\Delta\omega_r^{(h)}}{\lambda}\frac{d\hat{\omega}_r^{(h)}}{dt} \tag{5.14}$$

The expression in (5.15) is obtained from (5.14) by equating the last two terms to fulfill the Lyapunov stability criteria:

$$\hat{\omega}_r^{(h)} = k_p^{(h)}[\hat{\boldsymbol{\psi}}_{R,\beta}^{(h)}\boldsymbol{e}_{is,\alpha}^{(h)} - \hat{\boldsymbol{\psi}}_{R,\alpha}^{(h)}\boldsymbol{e}_{is,\beta}^{(h)}] + k_i^{(h)}\int_0^t [\hat{\boldsymbol{\psi}}_{R,\beta}^{(h)}\boldsymbol{e}_{is,\alpha}^{(h)} - \hat{\boldsymbol{\psi}}_{R,\alpha}^{(h)}\boldsymbol{e}_{is,\beta}^{(h)}]dt \tag{5.15}$$

where $k_p^{(h)}$ and $k_i^{(h)}$ are positive adaptation gains. The proportionality term in (5.15) is introduced to enhance the dynamic behavior of speed estimation[16]. The expression in (5.18) defines the law of speed adaptation that applies to any harmonic plane.

The sole presumption regarding the observer gain matrix $\boldsymbol{K}$ up to this point is that the observer poles are stable. The observer's poles are often positioned so that the observer error declines faster than the machine transients, and the speed adaptation technique handles medium- and high-speed ranges quite well. However, it falls short when operating in low-speed regenerative mode. To rectify this, a revised speed estimation law has been suggested in [91]. This law involves rotating the current estimation error by $e^{(-J\delta)}$, aligning the estimated current error parallel to the rotor flux in the dq frame. Hence, the estimation in the low-speed regenerative mode is accomplished, and the angle of rotation is computed in the following expression.

$$\delta = \begin{cases} \delta_m sign(\omega_s)\left(1 - \dfrac{|\omega_s|}{\omega_\delta}\right), & \text{if } \omega_s\hat{\omega}_{sl} < 0 \text{ and } |\omega_s| < \omega_\delta \\ 0, & \text{otherwise} \end{cases}$$

The maximum rotation angle δ_m and positive constant ω_δ are tuned until achieving stable output, as elaborated in [91].

5.3.2 Stability Analysis and Linearization of the Observer

Stability is crucial in designing and using full-order flux observers for VPPIM drive controllers, specifically in the low-speed regenerative mode of operation. The final derived speed estimation law only approximates the relationship between flux linkage and speed identification. The primary source of instability for this type of observer arises from the truncated rotor flux error component in the conventional speed adaptation law derivation. To mitigate this, employing a small signal linearized model of the speed-adaptive full-order flux observer and applying a modification strategy to the adaptation law can assist in selecting the observer gain effectively [93]. The analytical proof of the linearization and the stability in this research is implemented using the details in reference [91]. The root locus plot shows how the open-loop transfer function zeros and the poles of the closed-loop system migrated as the parameter ω_s moves in the low-speed range and regenerative

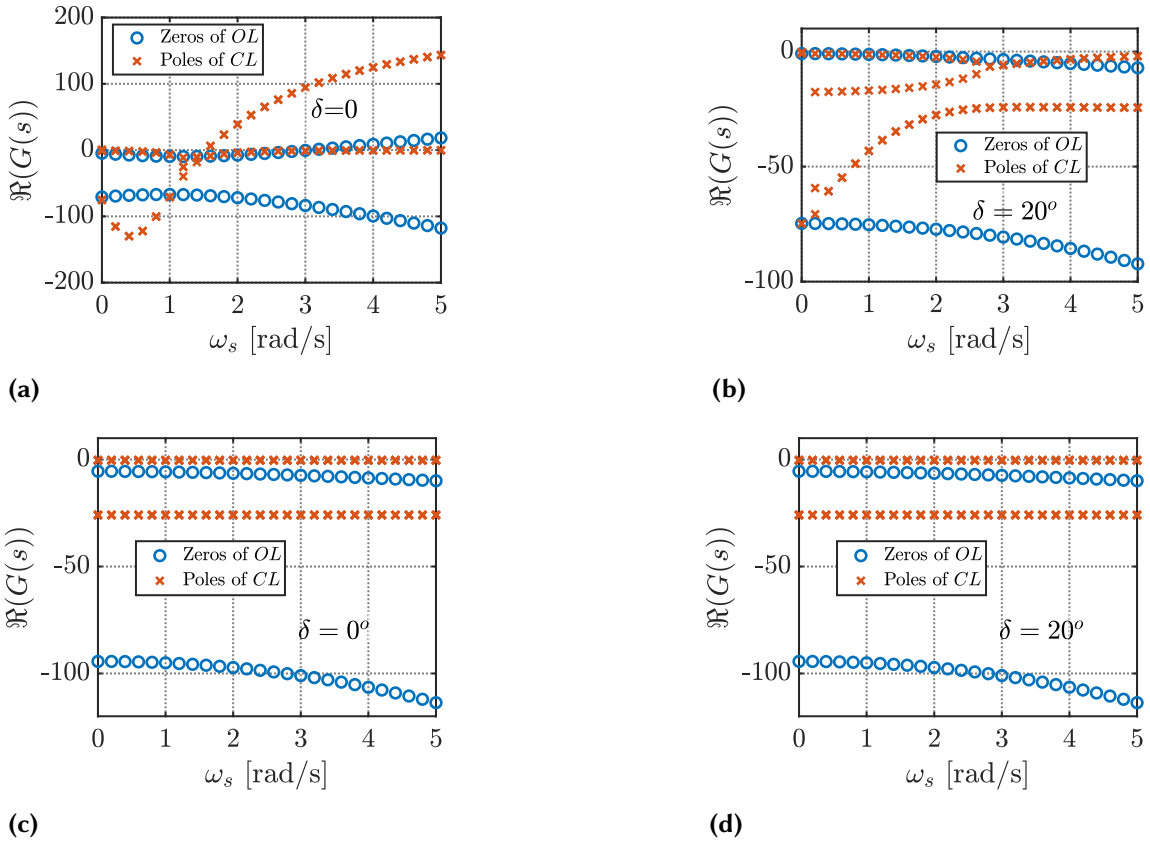

Figure 5.3: The root locus plots of the real part of the transfer function of the system ($G(s)$) with variable stator angular frequency (ω_s) in two distinct rotating angles (δ): (a) Conventional method in the first harmonic plane. (b) Proposed method in the first harmonic plane. (c) Conventional method in the third harmonic plane. (d) Proposed method in the third harmonic plane.

mode of operation. Hence, the plots are generated in both the conventional and proposed methods, for the two harmonic planes as depicted in Figure 5.3.

The simulation results depicted in Figure 5.3 (a) show the variation of the real part of the root locus plot as the stator angular frequency increases up to 5 [rad/s] in the conventional method, where δ is set to 0°. It indicates that some of the zeros and poles of the observer in the fundamental plane are unstable due to positive real eigenvalues. In contrast, when the suggested strategy is applied (at δ = 20°), introducing a phase shift in the stator current error in the dq frame, the zeros and poles migrate to negative real values, achieving stability in the low-speed regenerative mode of operation as shown in Figure 5.3 (b). Furthermore, results Figure 5.3 (c), taken at a rotating angle of 0° and Figure 5.3 (d), taken at a rotating angle of 20° illustrated the conventional and modified strategy methods in the third plane. The poles and zeros exhibit negative real values in both cases, thus achieving stability in the third harmonic plane.

5.3.3 Sensorless Pole Transition

One of the main features of VPPIMs that significantly affects the machine's torque is the pole transition, which performs a gradual change of the number of magnetic poles by feeding the machine with different harmonic plane voltage space vectors. During the pole transition, two distinct harmonic planes relative to the old and new pole configurations are excited at the same time. In this condition, both observers are used to estimate the

mechanical speed of the machine. Therefore, it is necessary to establish a rule that determines a unique value of speed estimation during the transition.

The speed estimation rule is also related to the pole transition strategy. This work implements a pole transition approach that utilizes ramp transitions between harmonic planes, specifically from the first to the third harmonic plane, as referenced in [5]. The approach involves pre-magnetization of the harmonic plane corresponding to the new pole configuration, while the harmonic related to the old pole configuration is slowly ramped down. Thus, during the pole transition both harmonic planes will exhibit a non-zero magnetizing current. The speed estimation is therefore calculated as a weighted average of the two parallel speed observers, where the weight is represented by the magnetizing current level $i_{s,d}^{(h)}$ in the harmonic plane h. The mathematical formulation is as follows:

$$\omega_r^{(1,3)} = \frac{\hat{\omega}_r^{(1)} I(1) + \hat{\omega}_r^{(3)} I(3)}{I(1) + I(3)} \tag{5.16}$$

where:

$$I(h) = \begin{cases} i_{s,d}^{(h)}, & \text{if } i_{s,d}^{(h)} > 0.7 i_{s,d,rated}^{(h)} \\ 0, & \text{otherwise} \end{cases} \tag{5.17}$$

The main reason behind the use of (5.16) is that model-based sensorless algorithms use the back-electromotive force to estimate the speed. Maintaining sufficient back-EMF during pole transition is crucial. Gradual transitions from two harmonic planes help keep speed estimates accurate and reduce torque ripples, avoiding sudden changes in current inputs used in the estimation process and resulting in smoother motor operation and less mechanical strain.

When the magnetizing current of the first or third harmonic plane falls below 0.7 times its nominal value, the dominant part of generated torque has likely shifted between harmonic planes. Therefore, the harmonic used for torque generation should also be consistently weighed in the speed estimation. The experimental test showed that a weight value below 0.7 hindered smooth sensorless transitions. A value of 0.7 allowed for quick adjustments without affecting performance. This value depends on the magnetizing current and the machine parameters.

It is also important to highlight how the third harmonic plane is characterized by a significantly lower magnetizing inductance (see Table 5.1), although the back-emf values can be of similar magnitude compare to those of the first harmonic plane due to an increased third-harmonic current and number of pole pairs (see the experimental results). Therefore, inaccuracies in the parameter estimation and in the current measurements influence the back-emf differently in the two harmonic planes. The threshold value in the speed estimation must, therefore, also consider these external factors, which are difficult to incorporate because they depend on the actual setup. While it is difficult to provide a theoretical indication of the threshold value, its validation on the setup is straightforward.

However, on the positive side, the fact that the d-axis currents on both harmonic planes are controlled simultaneously with closed-loop regulation - thanks to HPD modeling for VPPIMs - reduces the issues significantly. The absence of such regulation, leaving the currents to transition freely between two pole configurations during the transition, would most likely make the back-emf estimation tough and a sensorless speed estimation a very arduous task. A block diagram of the proposed weighted transition algorithm is provided in Figure 5.4.

The main reason behind the use of (5.16) is that model-based sensorless algorithms use the back-electromotive force to estimate the speed. Maintaining sufficient back-EMF during pole transition is crucial. Gradual transitions from two harmonic planes help keep speed estimates accurate and reduce torque ripples, avoiding sudden changes in current inputs used in the estimation process, and resulting in smoother motor operation and less mechanical strain.

When the magnetizing current of the first or third harmonic plane falls below 0.7 times its nominal value,

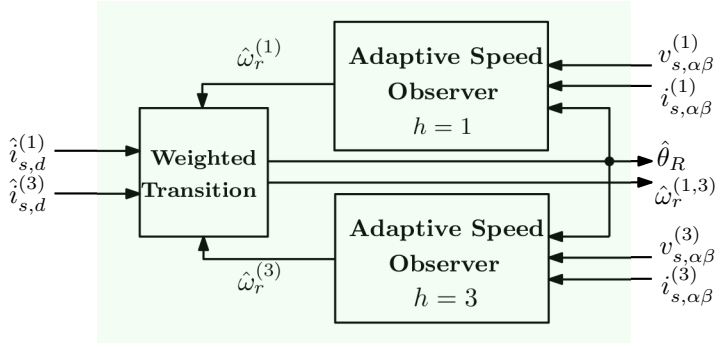

Figure 5.4: Block diagram of the proposed observer weighted speed transition between harmonic planes $[h = 1]$ and $[h = 3]$.

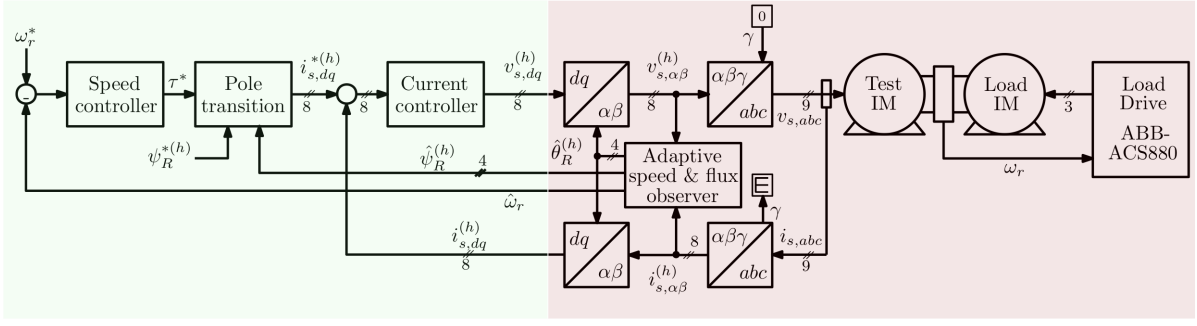

Figure 5.5: Block schematic of the sensorless VPPIM drive: The adaptive speed and flux observer is implemented in the stationary frame ($\alpha\beta$) for the first and third harmonic planes. Variables on the left (light green) are in the estimated rotor flux reference frame, while those on the right (light red) are in the stationary stator reference frame.

torque generation likely shifts between harmonic planes. Therefore, the harmonic used for torque generation should also be consistently weighed in the speed estimation. The experimental test showed that a weight value below 0.7 hindered smooth sensorless transitions. A value of 0.7 allowed for quick adjustments without affecting performance. This value depends on the magnetizing current and the machine parameters, which require calibration for each machine.

Both $I(1)$ and $I(3)$ can become zero if the stator currents fall below 0.7 of their rated values, which may occur under low load, low power demand, or in faulty conditions. This leads to a division by zero in the expression for $\omega_r^{(1,3)}$, requiring special handling, such as a fallback mechanism or calculation adjustment, to avoid errors or instability. A block diagram of the proposed weighted transition algorithm is provided in Figure 5.5.

5.3.4 Parameter sensitivity

In sensorless drives, parameter mismatches significantly impact stability and rotor-speed estimation. This research uses the method for compensating parameter sensitivity proposed in [91]. This study's method focuses on improving low-speed regenerative operation estimation, where stator resistance sensitivity is pronounced. Analytical validation shows robust stator resistance in two harmonic planes, with the estimated to actual rotor flux magnitude ratio nearing unity across rotor speed ranges, as shown in Figure 5.6. The results of the simulation suggest that the sensitivity to stator resistance changes is reduced in the third harmonic plane during low-speed regenerative operation.

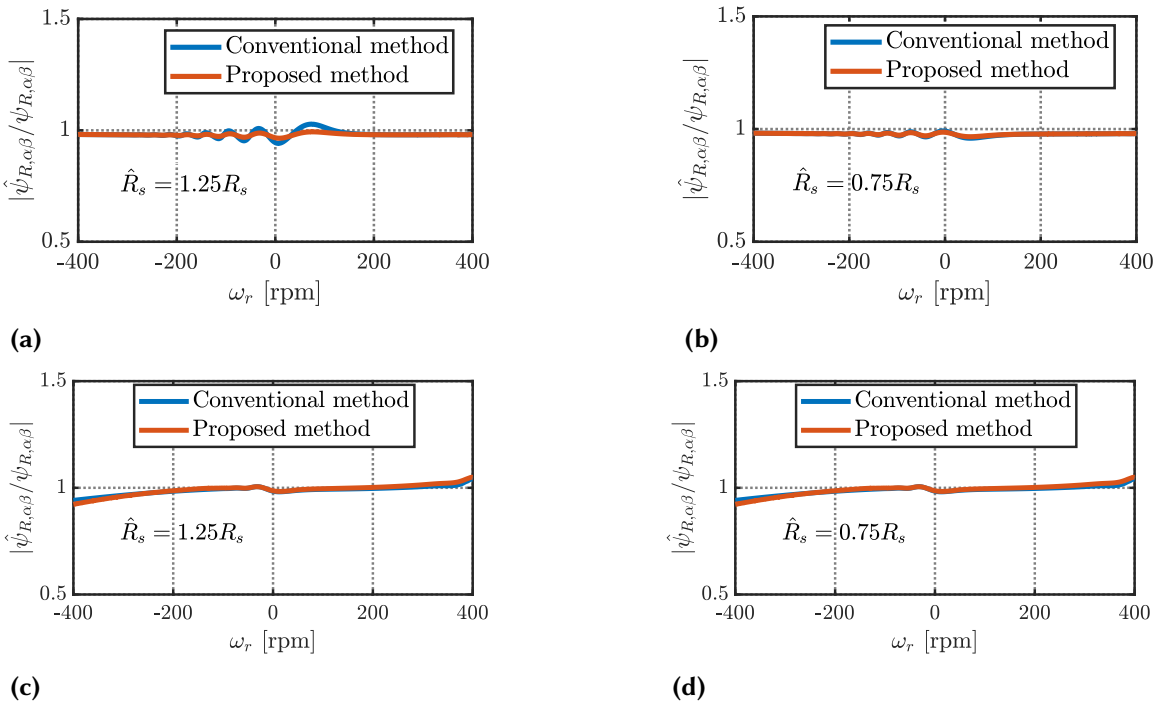

Figure 5.6: Effect of parameter errors on the rotor flux in two different harmonic planes: (a) $\hat{R}_s = 1.25R_s$ at $[h = 1]$. (b) $\hat{R}_s = 0.75R_s$ at $[h = 1]$. (c) $\hat{R}_s = 1.25R_s$ at $[h = 3]$. (d) $\hat{R}_s = 0.75R_s$ at $[h = 3]$.

5.4 Simulation Results

The proposed MRAS sensorless control has been introduced into the traditional IFOC strategy and implemented in the MATLAB/Simulink platform to validate the proposed methodology. The block diagram of the proposed scheme is shown in Figure 5.5.

5.4.1 Speed reversal performance at [h=1] and [h=3]

The results of the simulation, which examine the reversal of speed in motoring and regenerative modes in different harmonic planes under load conditions, are presented in 5.7 (a), 5.7 (b).

Figure 5.7 (a) represents the behavior of the machine in the two-pole configuration, therefore, when only the first harmonic plane is excited. The first sub-plot displays the magnetizing and torque-producing currents, $i_{s,d}^{(1)}$ and $i_{s,q}^{(1)}$ respectively. The second subplot compares the estimated, the reference, and the actual mechanical speeds in steady-state and speed deceleration during the motor and generator operating mode. It is noteworthy that the estimated speed is closely aligned with the actual speed. The third subplot shows the electromagnetic torque generated by the machine, which reaches a peak of -30 [Nm]. Lastly, the fourth subplot computes the rotor flux in the stationary reference frame.

Figure 5.7 (b) represents the behavior of the machine in the same operating conditions reported in Figure 5.7 (a) but in the six-pole configuration, therefore, when only the third harmonic plane is excited. The magnetizing and torque-producing currents are depicted in the first subplot. The second subplot shows that the speed estimation is performed effectively and compared with the reference and actual speed in the motoring and regenerating operation mode. Additionally, the third subplot represents the electromagnetic torque produced by the machine, while the last subplot of Figure 5.7 (b) illustrates the estimated rotor flux in the stationary reference frame.

5.4.2 Torque reversal and pole transition performance

The simulation results for pole transition and steady-state rotor speed estimation under load conditions are shown in Figure 5.8, specifically for motor and regenerative modes of operation in the first and third harmonic planes.

Speed estimation begins in the first harmonic plane for 400 [rpm] and covers the initial 6.5 s. A smooth transition occurs to the third plane, lasting until the 16 s mark in the motoring mode. The estimated speed aligns closely with the reference speed during this period. In the regenerative mode, the pole transition occurs in both planes. From 16 s to 26 s, speed estimation takes place in the first harmonic plane, maintaining good accuracy. Between 26 s and 36 s, the motor switches to third harmonic plane speed estimation in the regenerative mode, with results close to the reference speed as well.

5.5 Experimental Verification

The experimental test setup is shown in Figure C.1. It comprises a nine-phase symmetrical VPPIM with 36 slots and 18 coils, as illustrated in Figure 5.1, whose parameters are reported in Table 5.1. In addition, it comprises four three-phase converters (i.e., C1, C2, C3, and C4) controlled by an Opal-RT OP5700 system. C4 is not used for nine-phase configuration. These converters share a common DC-link voltage, which is powered by a 22kw regenerative load drive (ABB ACS880). The load drive also controls a 15kw three-phase one-pole pair im which is mechanically coupled to the test machine. The OP5700 is connected to a 1000 pulse encoder and a torque

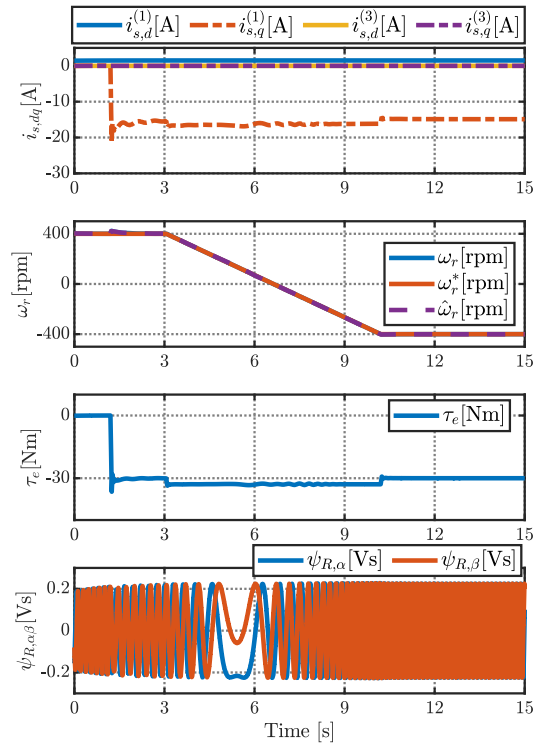

(a)

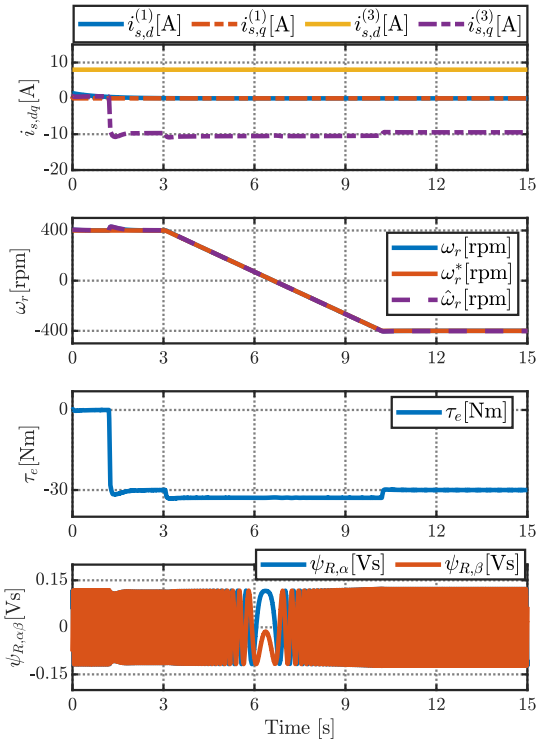

(b)

Figure 5.7: Speed reversal simulation results: (a) In the first harmonic plane, the VPPIM operates as a two-pole machine. (b) In the third harmonic plane when the VPPIM operates as a six-pole machine.

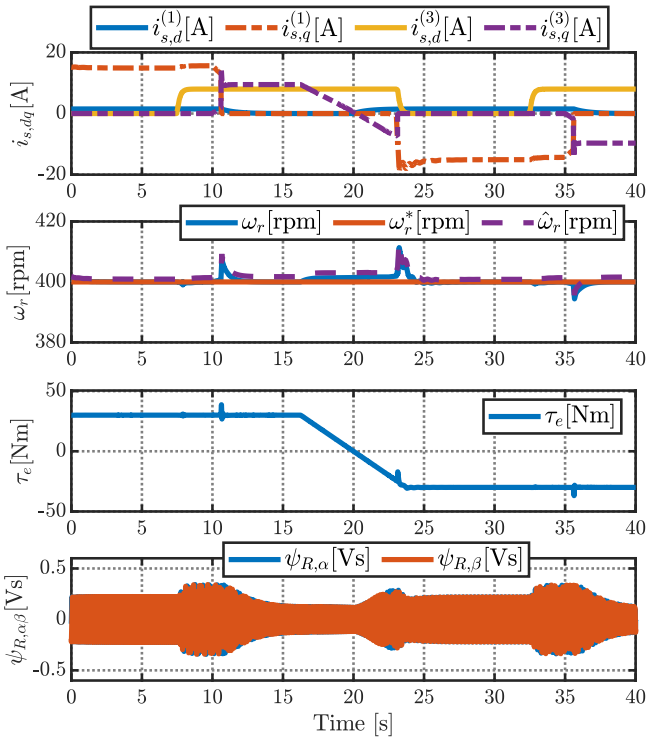

Figure 5.8: Torque reversal and pole transition simulation results in the first and third harmonic planes.

transducer to measure rotor speed and output torque. The experiment uses 4kHz as both the switching and current sampling frequency.

For the verification of the proposed MRAS observer, the test machine is operated in torque control mode, while the load machine is responsible for controlling the system's speed. As mentioned earlier, the applied magnetic pole transition strategy follows the results of [5]. The speed for pole number transition is set to 400 rpm. In general, this speed can be chosen by different criteria, one being the lowest possible losses as elaborated in [101].

5.5.1 Reference Frame Selection in the Observer Design

The adaptive law for the speed estimation is created out of this condition, where an additional proportional part is added to improve the estimation dynamics:

$$\hat{\omega}_r^{(v)} = k_p^{(v)}[\hat{\boldsymbol{\psi}}_{R,q}^{(v)}\boldsymbol{e}_{is,d}^{(v)} - \hat{\boldsymbol{\psi}}_{R,d}^{(v)}\boldsymbol{e}_{is,q}^{(v)}] + k_i^{(v)}\int_0^t [\hat{\boldsymbol{\psi}}_{R,q}^{(v)}\boldsymbol{e}_{is,d}^{(v)} - \hat{\boldsymbol{\psi}}_{R,d}^{(v)}\boldsymbol{e}_{is,q}^{(v)}]dt \tag{5.18}$$

The speed adaption law in (5.18) is derived in the dq rotating reference frame, but [104] shows how the law could be implemented in other reference frames, like the stationary $\alpha\beta$ one as described in (5.15).

5.5.1.1 Experimental results in the rotating dq- reference frame

Considering the adaptive law implemented in the rotating dq reference frame, Figure 5.9, 5.10, and 5.11 provide the experimental results when the speed is estimated by a weighted average of the (5.16) expressed for the first-harmonic and third-harmonic space vector. The weights for the averaging calculations are the d-axis

Table 5.1: Measured electrical parameters (inverse-Γ) and the rated values of the test machine configured as symmetrical 9-phase.

h	R_s [mΩ]	L_σ[mH]	L_M[mH]	R_R[mΩ]
1	285	7.3	175.8	192.6
3	285	5.0	17.4	106.8
5	285	3.9	4.8	67.4
7	285	3.1	2.0	45.5
$V_n[V]$	I_n [A]	τ_n[Nm]	ω_n[rpm]	f_n[Hz]
400	15	48	2934	50
$cos(\phi)$	$K_p^{(1)}$	$K_i^{(1)}$	$K_p^{(3)}$	$K_i^{(3)}$
0.9	10,000	150	1000	50

current values for each space vector. Furthermore, the modified algorithm described in reference [91] is also integrated to improve the low-speed estimation.

In the results presented in Figure 5.9, voltages and thus currents are initially excited with the first-harmonic space vector, corresponding to a 1 pole pair configuration, for 10 s under constant load conditions. Subsequently, the first-harmonic space vector is substituted by the third-harmonic space vector for an additional 20 seconds before returning to the first-harmonic space vector until the end of the time window. Based on the above excitation, the first subfigure illustrates the references, actual flux-generating currents ($i_d^{(1,3)}$), and torque-producing currents ($i_q^{(1,3)}$) for both space vectors. The speed estimate at 500 [rpm] remains accurate and transitions well while applying the weighted average speed adaptive law, as is evident from the second subfigure. The load remains constant at 35 [Nm] and is depicted in the third subfigure. The fourth and fifth subfigures show the voltages and currents in the *abc* reference frame. Apart from minor torque and speed disparities during the transition, the two harmonic planes exhibit smooth behavior. Furthermore, the zoomed-in plots of Figure 5.10, and 5.11 show the seamless magnetic pole transition in the fundamental and third space vector, and vice versa.

5.5.1.2 Experimental results in the stationary $\alpha\beta$ - reference frame

Similar experimental results using the speed adapting law (5.18) in the stationary $\alpha\beta$ frame are depicted in Figure 5.12, 5.13, and 5.14. Again, the speed is estimated by a weighted average of the (5.16) expressed for the first and third space vector.

In the results shown in Figure 5.12, at the beginning, the space vector is excited with the first harmonic for 10 s under constant load conditions. Subsequently, it is excited with the third harmonic for an additional 10 s before returning to the first harmonic until the end. The first sub-figure shows the references, actual flux-generating currents ($i_d^{(1,3)}$) and the torque-producing currents ($i_q^{(1,3)}$) for both harmonics. The speed estimate is accurate, as observed in the second sub-figure at 800 [rpm]. The load is constant at 30 [Nm] and is shown in the third sub-figure. The fourth and fifth plots show the voltages and currents of the stator in the *abc* reference frame. Except for some insignificant torque and speed disparity during the transition, the two harmonic planes are transitioning smoothly. Moreover, the magnified plots in Figure 5.13 and 5.14 reveal the seamless transition of the magnetic poles in the two space vectors. The findings show that both MRAS-based sensorless solutions for VPIM work reliably and effectively, both in steady-state conditions and also in the more challenging magnetic pole transition cases. From an implementation point of view, the equations in the

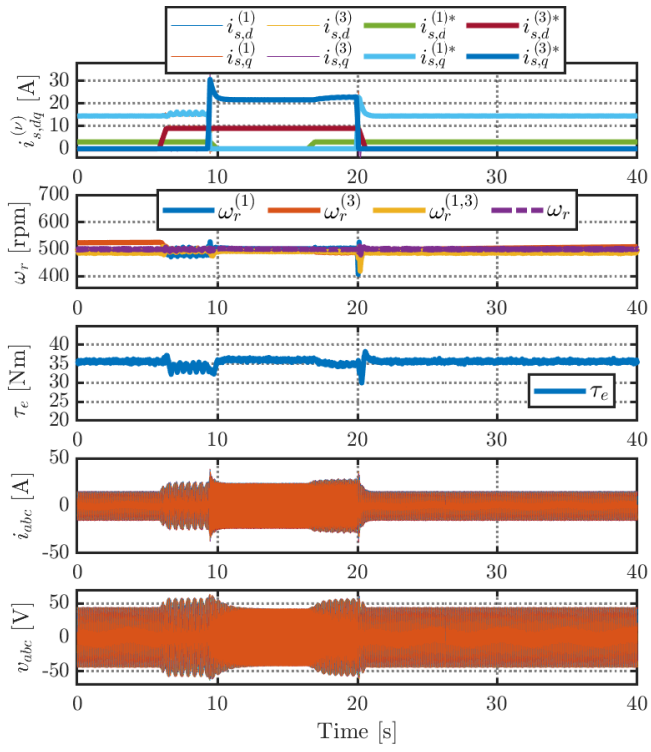

Figure 5.9: Experimental validation of speed estimation using the first-harmonic and third-harmonic space vectors using the *dq* reference frame under constant load conditions.

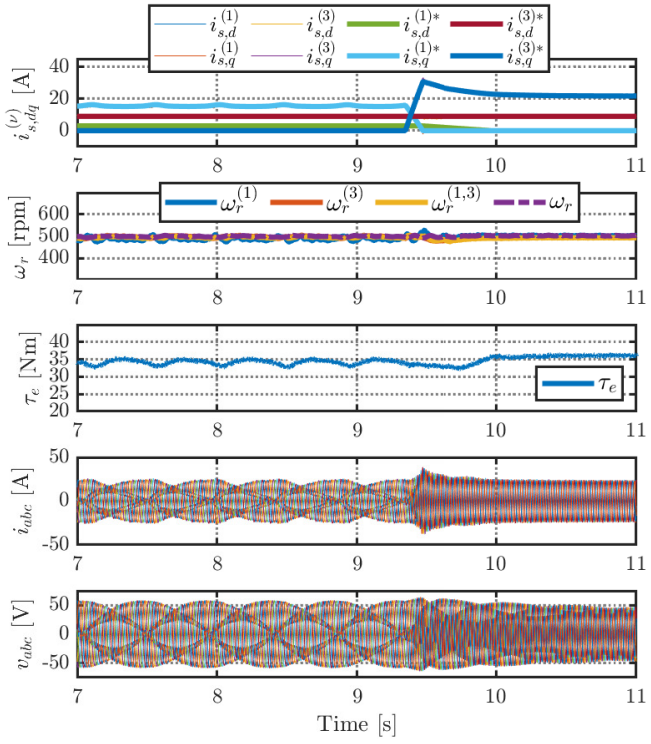

Figure 5.10: The zoomed-in plot illustrates the experimental verification of speed estimation from the first-harmonic to the third-harmonic space vector in the *dq* reference frame, considering a constant load condition.

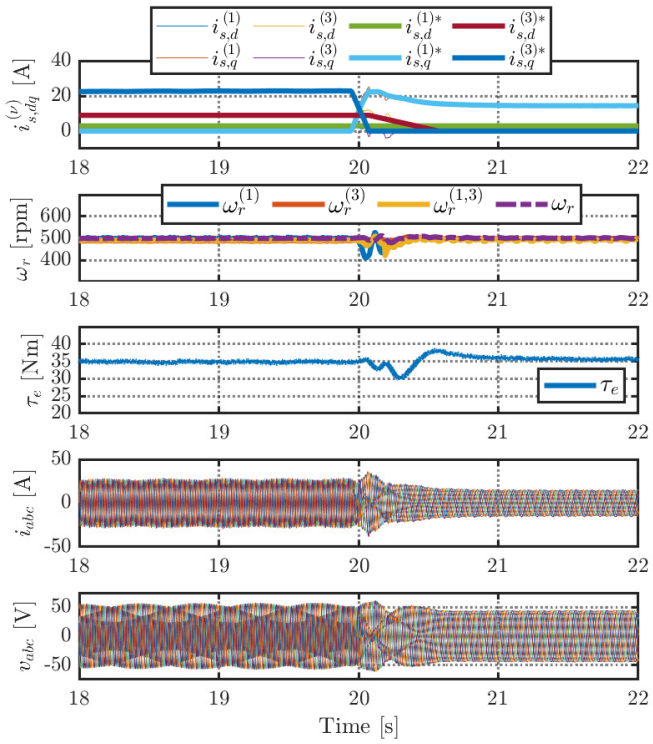

Figure 5.11: The zoomed-in plot illustrates the experimental verification of speed estimation from the third-harmonic to the first-harmonic space vector in the *dq* reference frame, considering a constant load condition.

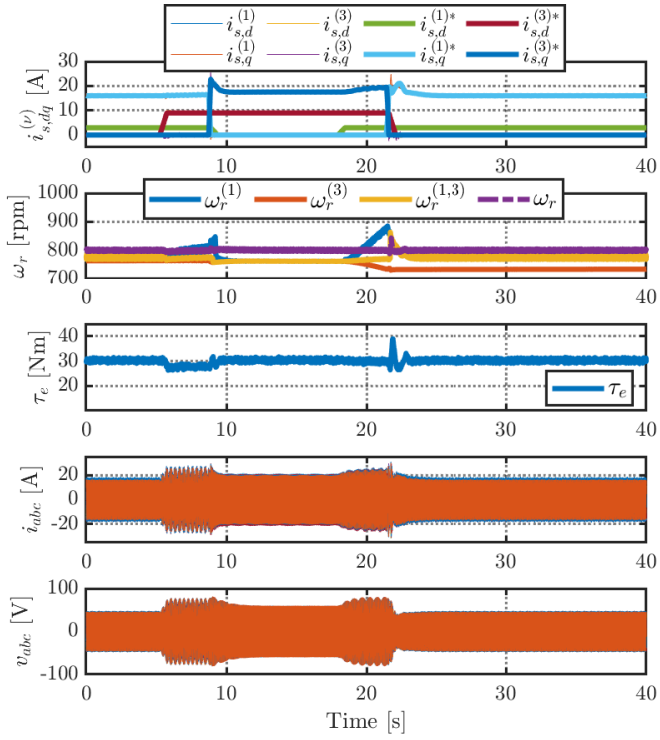

Figure 5.12: Experimental validation of speed estimation with the first-harmonic and third-harmonic space vectors using the $\alpha\beta$ reference frame under constant load conditions.

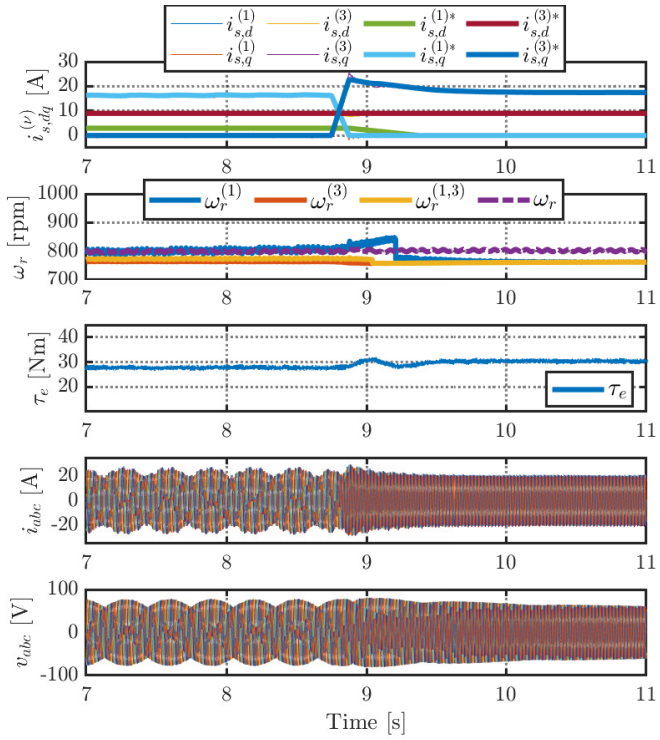

Figure 5.13: The zoomed-in plot illustrates the experimental verification of speed estimation from the first-harmonic to the third-harmonic space vector in the $\alpha\beta$-frame, considering a constant load condition.

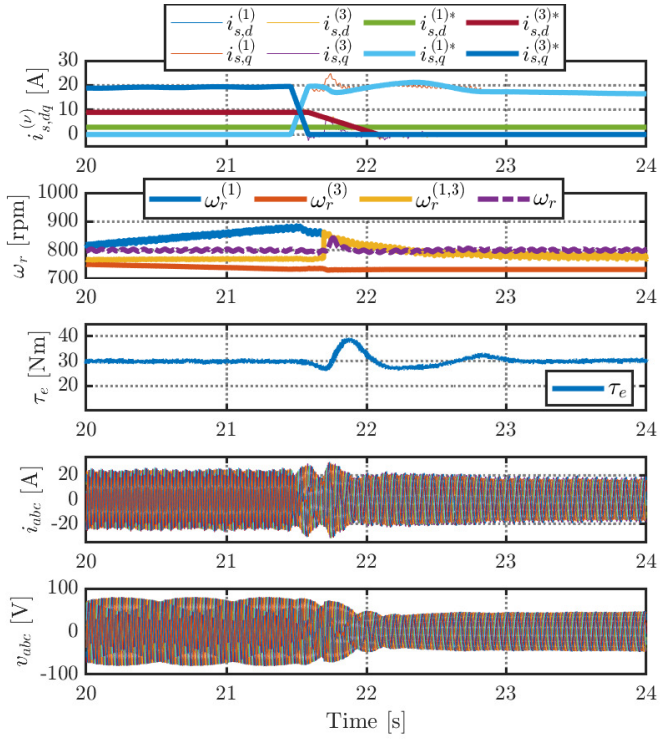

Figure 5.14: The zoomed-in plot for the experimental verification of speed estimation from the third-harmonic to the first-harmonic space vector in the $\alpha\beta$-frame, considering a constant load condition.

dq reference frame are slightly more complicated (and thus computationally intensive) due to the presence of the rotating transformations. The equations in the $\alpha\beta$ reference frame, instead, are simpler and directly related to the stator quantities.

Experimental tests have demonstrated that both the rotating reference frame and the stationary frame provide accurate speed estimates within the moderate-speed range. However, implementing the speed estimation in the stationary frame requires less computational time compared to the counterparts of the rotating frame. Therefore, for future implementations, it is advisable to use models based on the stationary reference frame, as it offers simplicity and efficient speed estimation and magnetic pole transitions based on the operating point. Consequently, the VPIM exhibits characteristics that position it as a strong candidate within the electromobility industry.

5.5.2 Speed reversal performance in the $\alpha\beta$ reference frame

As illustrated in Figure 5.15, the performance evaluation is conducted during the reversal of speed in the fundamental space vector within the stationary frame. The initial subplot shows the stator current's d and q-axis components for various space vectors, alongside their reference values, highlighting accurate current tracking. Following this, the second subplot illustrates the rotor speeds for both systems, showcasing the combined rotor speed ($\omega_r^{(1,3)}$). Step changes indicate transitions in control, although there are slight mismatches in estimating speeds when approaching zero speed. The third subplot illustrates the negative electromagnetic torque (τ_e), maintaining stability with minor fluctuations, indicating consistent system performance. The fourth subplot illustrates the applied currents (i_{abc}) in the abc frame depicted as a sinusoidal signal, and the concluding subplot presents the applied voltages (v_{abc}), likewise represented as sinusoidal waves. In general, these plots demonstrate the system's ability to estimate speed close to zero accurately and its robust dynamic response across various operating conditions.

5.5.3 Speed reversal performance in the dq reference frame

The performance characteristics related to speed reversal in the fundamental space vector within the dq reference frame are shown in Figure 5.16. The first subplot depicts the components of the d and q-axis of the stator current across different space vectors, along with their respective reference values, highlighting precise tracking of the current. The following subplot shows the estimated rotor speed using the weighted average magnetizing current algorithm, ($\omega_r^{(1,3)}$), where step changes indicate that smooth transitions are not achievable due to the high computational time required in these frames. The third subplot depicts the electromagnetic torque (τ_e), which remains unstable and has oscillations. In the fourth subplot, the applied currents (i_{abc}) are displayed as sinusoidal waveforms in the abc frame, while the final subplot illustrates the applied voltages (v_{abc}), also exhibiting sinusoidal patterns in the same frame. In conclusion, these plots reveal that in the dq frame, speed reversal is not accomplished for lower speed estimations, particularly during regenerative operation. This is due to the requirement for double the computation time on this frame.

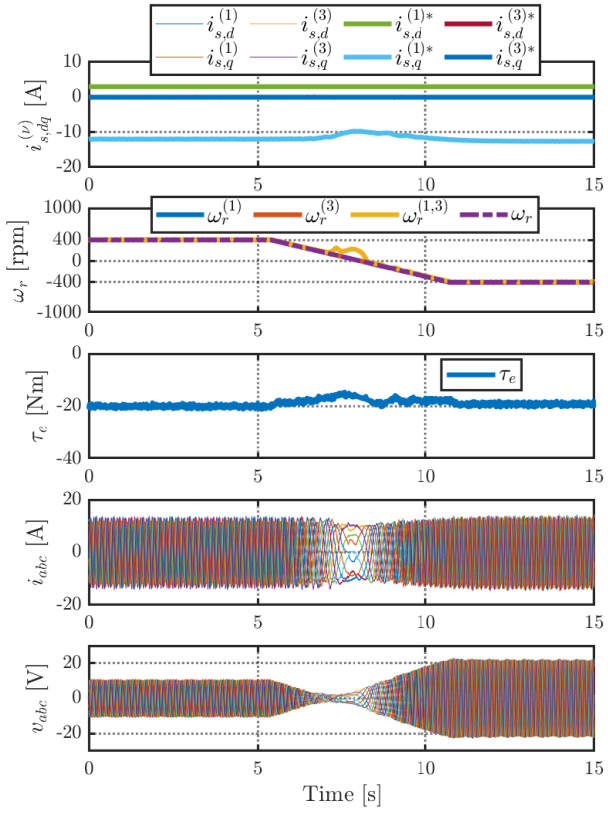

Figure 5.15: Experimental result of speed reversal performance using the fundamental space vector in the $\alpha\beta$-frame under constant load conditions.

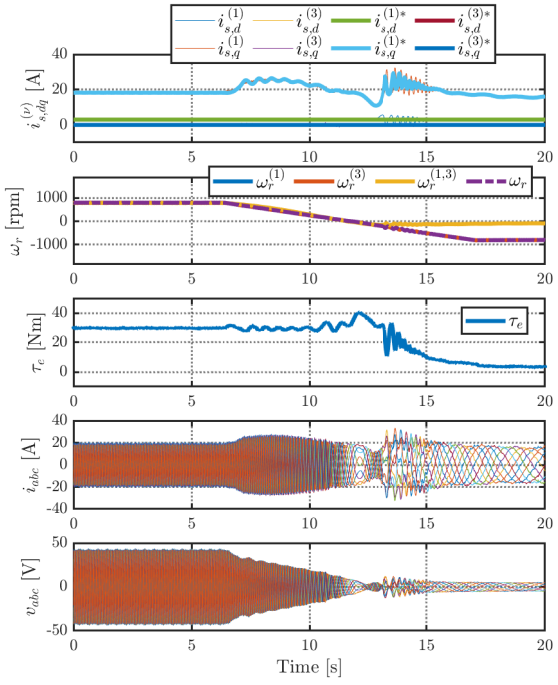

Figure 5.16: Experimental performance of speed reversal within the fundamental space vector in the *dq*-frame under a constant load condition.

5.5.4 Performance of the VPPIM at the rated speed

Figure 5.17 illustrates the rotor's rated speed performance with the suggested sensorless drive system in the base VPPIM configuration. The speed increased from 1000 rpm to 2934 rpm and then returned to 1000 rpm, consistently under a load of 30 Nm, demonstrating a good result of the speed estimates.

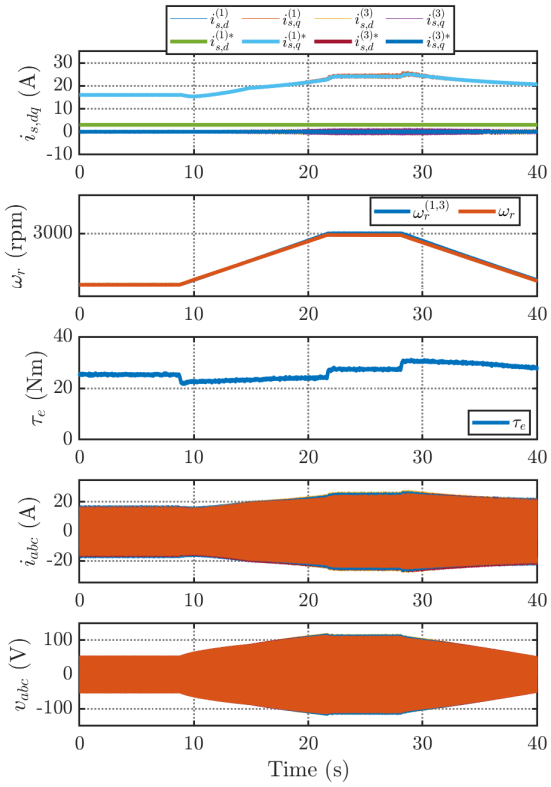

Figure 5.17: Experimental results of the VPPIM at the rated speed in the base configuration.

5.5.5 Speed reversal at [h=1] and [h=3]

In Figure 5.18 are reported the behavior of the proposed sensorless control for nine-phase VPPIM during a speed reversal when the machine operates with two-pole Figure 5.18 (a) and six-pole Figure 5.18 (b) under load conditions.

In Figure 5.18 (a), the machine operates with two poles. In the first subplot, the magnetizing current $i_{s,d}^{(1)}$ and the torque producing current $i_{s,q}^{(1)}$ are displayed. In the second subplot, a comparison is made between the actual speed and the estimated speed. Notably, during the initial 7.5 s, the generator operating mode scenario demonstrates that the measured speed at 400 rpm to -400 rpm closely aligns with the estimated speed. In addition, it provides a reliable estimate for the motor operating mode mode throughout the remaining time interval. The estimated and the actual speed can effectively cross the zero line despite minor misalignment at the crossing line. In the third subplot, the trend of the measured torque is reported. Lastly, the fourth subplot shows the estimated rotor flux linkage in the stationary frame.

In Figure 5.18 (b), the machine operates with three poles. The magnetizing and torque-producing currents are depicted in the first subplot. The second subplot of the experimental results shows the steady-state rotor speed measurement result from 400 rpm to -400 rpm in both operating modes. As seen from the results, during

a deceleration scenario from the initial point to 7.5 s, in the generator operating mode, and for the rest of the time interval for the motor operating mode, the measurement results agree well with the actual speed. The estimated and real speed can also effectively pass the zero line despite a small misalignment close to the zero crossing line. Hence, successful speed reversals under -30 Nm loaded conditions have been validated in the third harmonic plane, as shown in the third subplot. Finally, the estimation of the rotor flux linkage in the stationary frame is shown in the final subplot. In Figure 5.18 (b), the machine operates with three poles. the magnetizing and torque-producing currents are depicted in the first subplot. The second subplot of the experimental results shows the steady-state rotor speed measurement result from 400 [rpm] to -400 [rpm] in both operating modes. As seen from the results, during a deceleration scenario from the initial point to 7.5 s, in the regenerating mode, and for the rest of the time interval for the motoring mode, the measurement results are well agreed with the actual speed. The measurement and real speed can also effectively pass the zero line despite a small misalignment close to the zero crossing line. Hence, successful speed reversals under -30 [Nm] loaded conditions have been validated in the third harmonic plane, as shown in the third subplot. Finally, the estimation of the observed rotor flux in the stationary frame is shown in the final subplot.

From Figure 5.18 (a), speed and torque estimates in the fundamental harmonic plane are prone to oscillations for the time interval from 5 to 10 s due to challenges in retrieving the back-emf information. In contrast, the third harmonic plane has more back-emf information (see the rotor flux linkage magnitude for both harmonic planes). This interesting aspect results in an improved speed and torque estimates as depicted in Figure 5.18 (b) for the same time interval from 5 to 10 s. Thus, low-speed estimation should use the third harmonic plane and a high pole count for better performance in speed-sensorless algorithms. This fact is perfectly in line with our intended use of the machine: high pole counts for low speeds to achieve higher torques.

5.5.6 Torque reversal and pole transition at [h=1] and [h=3]

The speed estimation incorporating the weighted transition algorithm plays a crucial role in the sensorless drive for VPPIM when a pole transition occurs, as illustrated in Figure 5.19 and some zooms that illustrate the detail of the transitions are reported. The motoring mode of operation during transition is demonstrated by Figure 5.19. Moreover, the regenerative mode of operation is also depicted to show the verification due to pole transitions through the same figure.

In the initial 6.5 s, the machine operates in the first harmonic plane. Thereafter, a transition between the third harmonic plane and back to the first harmonic plane occurs, lasting until the 20 s mark in motoring mode with 30 [Nm] loaded. Throughout this period, the estimated speed closely tracks the actual speed as represented in the zooms of Figure 5.20 (a) and 5.20 (b). Following this, from 20 seconds on-wards until the end of the simulation, the drive operates in regenerative mode, during which speed estimation is performed using the first and third harmonic planes. In the regenerative mode, pole transitions occur in both planes again. Between 20 s and 40 s, the motor switches between the first and third harmonic planes in the regenerative mode with a load of -30 [Nm], with results close to the actual speed as represented in the zooms of Figure 5.21 (a) and 5.21 (b).

As shown in Figure 5.21, inter-plane cross-saturation phenomena are observed when both harmonic planes are magnetized simultaneously [5]. This happens during the pole transition and is followed by a smoothing-out process after the transition across all operational regions under various load conditions. Future research must focus on developing innovative strategies to reduce this effect and ensure smooth pole transitions.

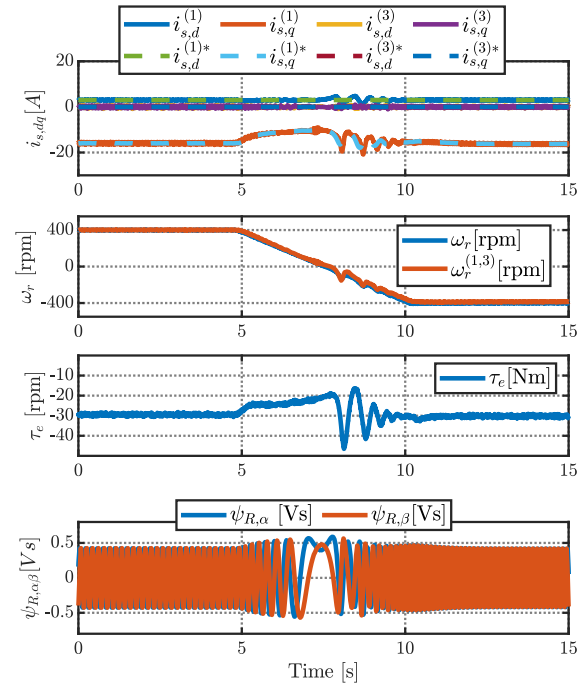

(a)

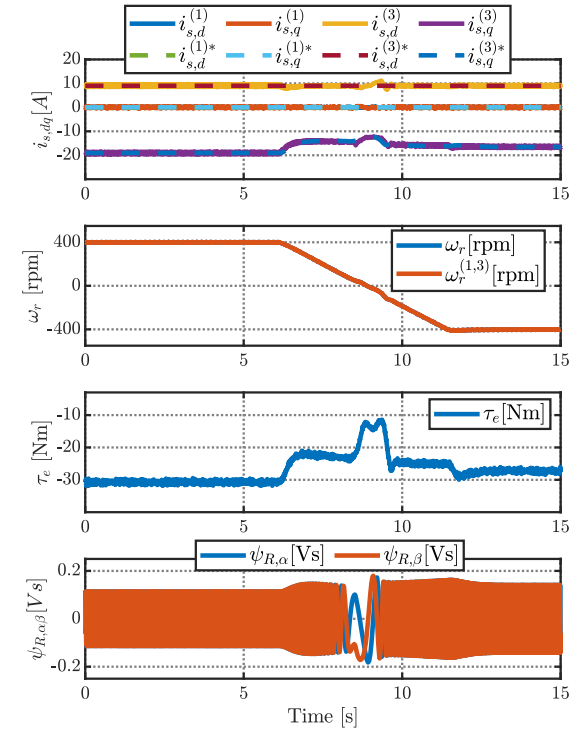

(b)

Figure 5.18: Speed reversal experimental results: (a) In the first harmonic plane when the VPPIM operates as a two-pole machine. (b) In the third harmonic plane when the VPPIM operates as a six-pole machine.

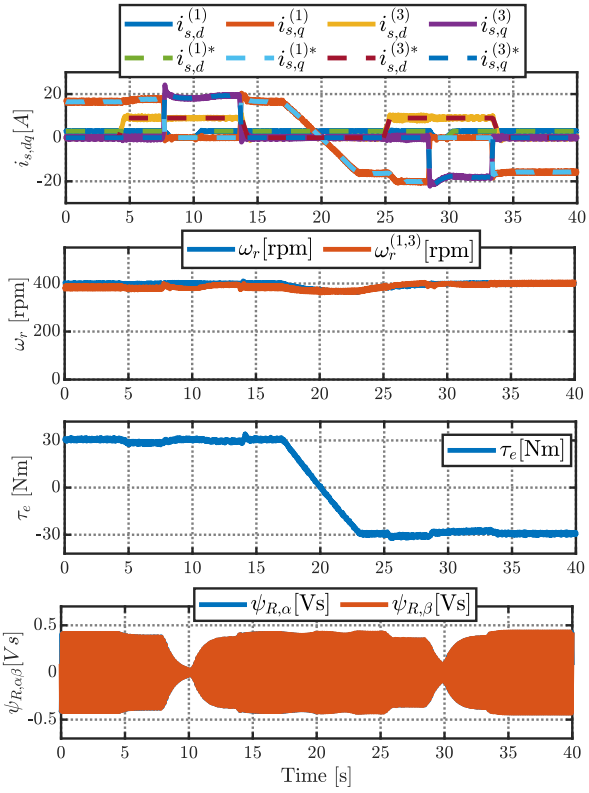

Figure 5.19: Torque reversal and pole transition experimental results in the first and third harmonic planes.

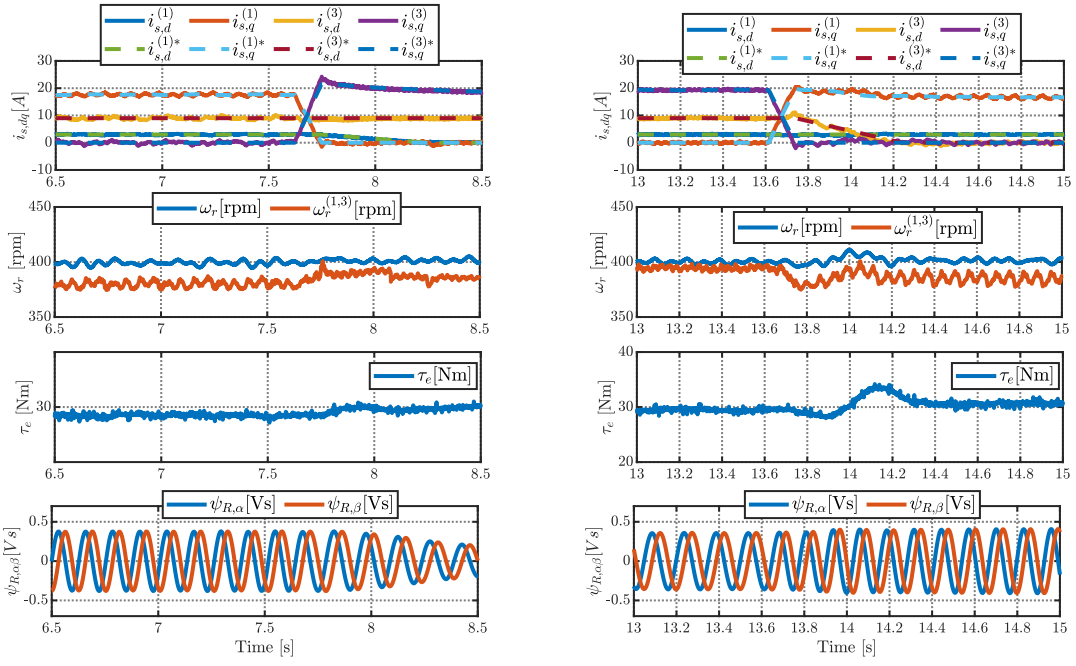

(a) **(b)**

Figure 5.20: (a) Pole transition in the motoring mode from $[h = 1]$ to $[h = 3]$. (b) Pole transition in the motoring mode from $[h = 3]$ to $[h = 1]$

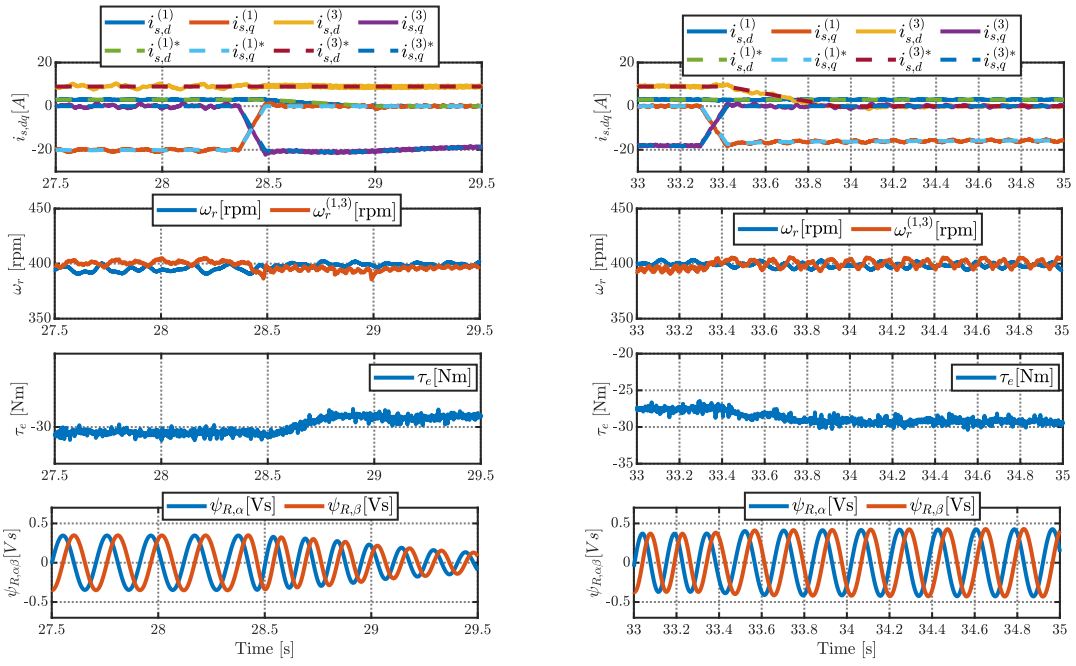

(a) **(b)**

Figure 5.21: (a) Pole transition in the regenerative mode from $[h = 1]$ to $[h = 3]$. (b) Pole transition in the regenerative mode from $[h = 3]$ to $[h = 1]$

5.5.7 Results from experiments on parameter sensitivity

The theoretical sensitivity analysis performed in the reference [105] is still valid for the machine under test. One of the most critical parameters is R_s, which varies due to temperature and affects the stability and accuracy of the speed observer at low stator frequencies. Consequently, an experimental case study is performed for each harmonic plane in which the estimated stator resistance is 70% of the real value of R_s, and the performance at low stator frequencies is analyzed. The results are presented in Figure 5.22 (a), 5.22 (b), 5.23 (a), and 5.23 (b) for the regenerating and motoring modes, respectively, considering the fundamental and the third harmonic planes.

As expected, the accuracy of the speed observer at low stator frequencies is sensitive to the discrepancies in the value of R_s. The fundamental harmonic plane starts to behave unreliably in generating mode at roughly 200 rpm, whereas the third harmonic plane remains reliable down to 75 rpm. There are multiple reasons for the existence of two distinct minimum stable speeds in the generating mode. Each harmonic plane is independent with a unique set of parameters and slip. Thus, the amplitudes of the back-EMF in the two harmonic planes differ, as illustrated in Figure 5.22 (a), 5.22 (b) . The third harmonic plane demonstrates increased stability towards lower frequencies, confirming the original thought that the operation of variable phase-pole machines towards the zero frequency should happen at the highest possible number of poles. In motoring mode, the speed observer of both harmonic planes is stable towards 0 rpm, as shown in Figure 5.23 (a), 5.23 (b) .

At zero speed, a positive stator frequency due to a non-zero load allows the back-EMF to be estimated with minimal impact from resistive voltage drops. With accurate parameters, speed estimation can closely approach the zero stator frequency.

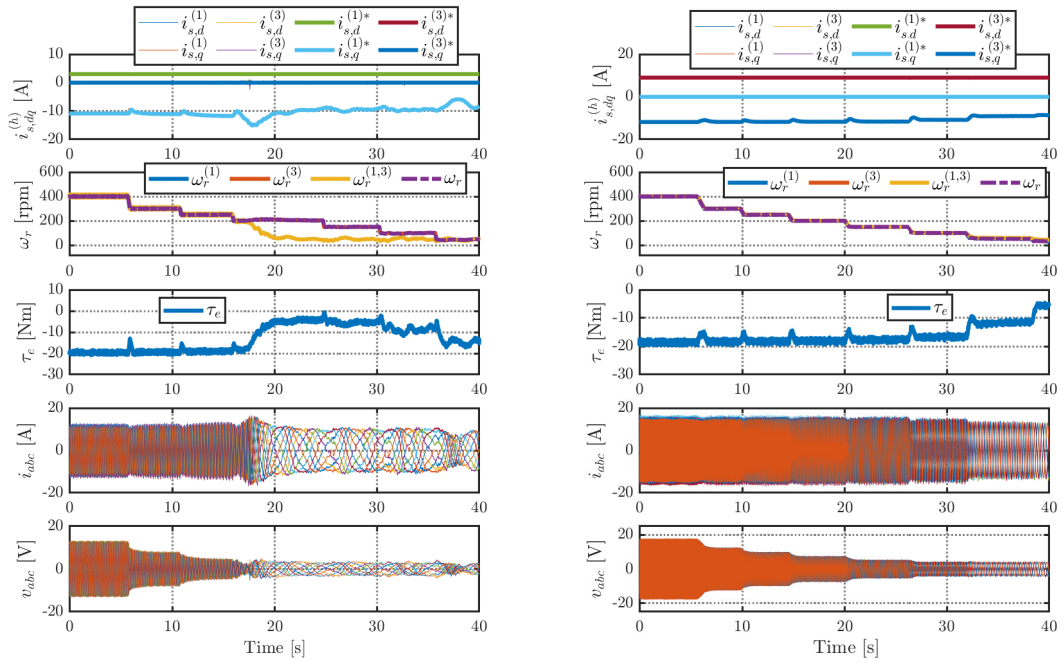

(a) (b)

Figure 5.22: Analysis of experimental sensitivity: estimated stator resistance is equal to 70% of the actual value. Step speed estimation while operating in generating mode: (a) in the first harmonic plane, (b) in the third harmonic plane.

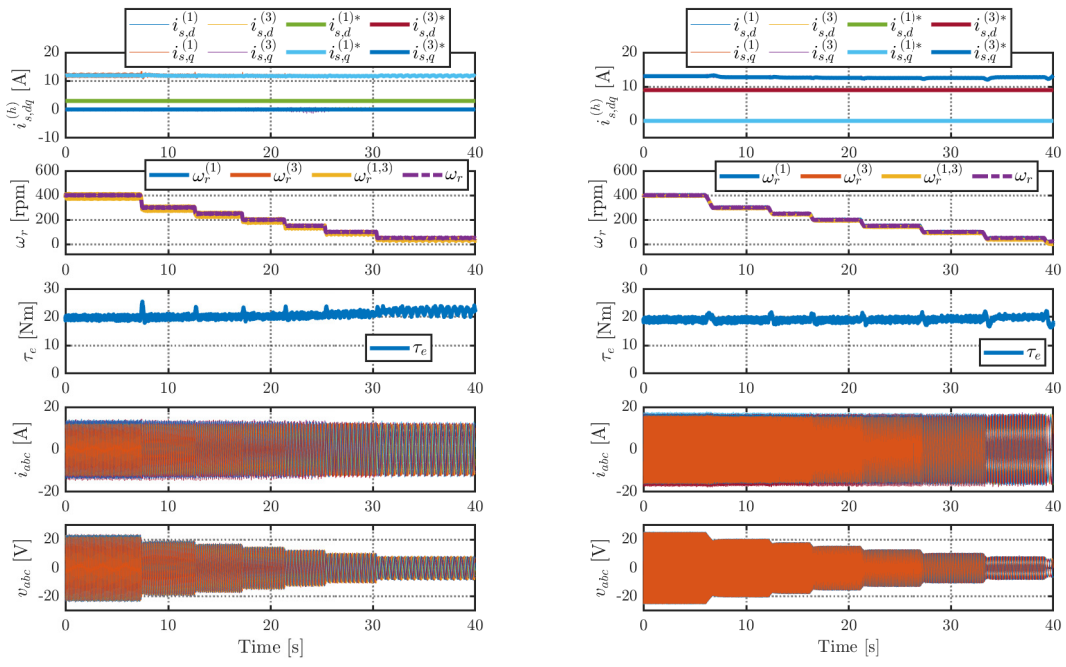

(a) (b)

Figure 5.23: Analysis of experimental sensitivity: estimated stator resistance is equal to 70% of the actual value. Step speed estimation while operating in motoring mode: (a) in the first harmonic plane, (b) in the third harmonic plane.

5.6 Summary

VPPIMs are potential candidates for electromobility due to their versatility in torque-speed range and efficiency, omitting rare-earth materials. They, however, present challenges in analytical modeling, control scheme development, and parameter estimation. A critical issue is the smooth transition between different pole-pair configurations, crucial for sensorless control. This research proposed a sensorless strategy for a variable phase-pole induction machine that effectively estimates and regulates the mechanical speed during operation in different harmonic planes, load variations, speed reversals, and pole transitions.

The algorithm is based on a full-order observer and a model reference adaptive system approach. The speed is simultaneously estimated by two parallel observers operating in two different harmonic planes, and the final speed estimation is obtained as the weighted average of the two independent speed estimations. The weight is represented by the magnetization current in each harmonic plane. The stability of the proposed method is demonstrated with the Lyapunov stability criteria. Simulations and experimental tests validate the approach, demonstrating the feasibility of sensorless operation for variable phase-pole induction machines even under pole transition. Future research should focus on evaluating the VPPIM's performance against standard driving cycles such as the Worldwide Harmonised Light Vehicles Test Procedure (WLTP) as well as conducting studies on alternative sensorless methodologies that could apply to VPPIMs.

6 Concluding Remarks

6.1 Conclusions

One of the primary contributions of the research is the high degree of agreement among several numerical methods for examining both the steady-state and transient behaviors of variable-phase-pole induction machines. The research assesses several phase-pole arrangements, looking at how the machine's performance is affected by the number of poles and phases under different operating circumstances. The consistency of the results across various setups confirms the validity and dependability of the simulation methods used. In practical applications, this comparison is essential for choosing the best phase-pole topologies, particularly when considering the trade-offs between torque and speed.

The work offers a significant suggestion for further investigation into variable phase-pole machine design. It recommends that while optimizing the machine's performance for high-speed operation at lower torque values, pole adjustments should be given priority over changes in flux linkage levels. Pole alterations provide a more realistic and effective way to achieve the desired performance over a wider range of speeds, but changing flux linkage can be a more complicated and resource-intensive technique. This makes the finding noteworthy. Therefore, more research on pole-switching techniques is needed to enhance these machines' dynamic performance in high-speed areas. This is crucial for traction applications where torque efficiency and speed are both essential.

The assessment of a parameter estimation method that combines FEA with a per-solenoid approach and HPD theory is an essential component of the study. The better accuracy and consistency of this novel methodology are demonstrated by contrasting it with traditional parameter estimation techniques. More accurate assessment of characteristics like inductances, resistances, and mutual coupling coefficients is made possible by the per-solenoid technique, which divides the machine's behavior into smaller, easier-to-manage segments (solenoids). A harmonic-based examination of the machine's magnetic field distribution is incorporated into the HPD theory, further refining the findings. Regarding computing performance, the novel method outperforms the conventional methods in terms of speed and efficiency. This approach offers a valuable tool for improving the design and operation of variable phase-pole machines in practical applications by facilitating quicker convergence and more precise key parameter estimations.

The sensorless speed regulation method created for the variable phase-pole induction machine is another noteworthy addition to this study. This technique estimates and controls the motor's speed without physical speed sensors by combining MRAS with full-order observers. While the full-order observer estimates the system's state variables, the MRAS algorithm adjusts the control signals in real time by comparing the observed output with a reference model. Through extensive simulation and experimental testing, the stability and viability of this sensorless approach are confirmed, showing that it functions well even during pole transitions — a situation in which many sensorless approaches might falter because of the inherent variations in motor parameters. The experimental findings demonstrate that this method effectively sustains correct estimation and steady speed control even when the machine alternates between various pole configurations, making it appropriate for real-world applications requiring resilience and dynamic performance.

6.2 Suggestions for future work

Inter-plane cross-saturation effects during simultaneous harmonic plane magnetization can seriously impair the accuracy and performance of magnetic systems; future studies should concentrate on reducing these effects. Cross-saturation is the result of undesirable distortions caused by the interaction of several magnetic fields, which results in inaccurate responses from the system. Researchers can increase the accuracy and efficiency of magnetic field models by tackling this problem, particularly in applications involving intricate or multi-frequency magnetization processes. More dependable and efficient magnetic systems would result from the development of sophisticated mechanisms to isolate or regulate these interacting fields, maybe through creative material design or cutting-edge computational methods. In the end, this research may improve the efficiency of machinery such as electric motors and transformers, where exact control over magnetic fields is essential for optimum performance.

In particular, increasing the efficiency, torque density, and operational stability of electrical machines requires more research into the best pole-phase topologies. Researchers can find configurations that minimize losses, lessen cogging effects, and improve overall motor control, especially under varied load conditions, by examining different combinations of pole and phase arrangements. Investigating new geometries, the effects of pole-phase mismatches, and the function of cutting-edge materials in improving these configurations are some possible topics for this study. Furthermore, the behavior of various pole-phase configurations can be modeled and predicted using computational tools and simulation techniques, making it easier to build machines that are more effective and adaptable. The ultimate objective of this effort is to provide standards for the design of machines with improved performance metrics, which will help applications in high-performance industrial motors, automotive systems, and renewable energy.

Moreover, future research should focus on investigating a synchronous machine capable of adjusting its phase and pole configurations in real-time.

A Global and Local Stability

Global stability is a good attribute of some nonlinear systems. Accordingly, $x(t)$ converges to the same equilibrium point $x^\star$ regardless of the initial position $x(0)$ in the state space. But proving global stability might be challenging. For this, so-called Lyapunov functions — also known as Lyapunov's second or direct method — are quite effective, although they are frequently tricky to locate. As will be demonstrated briefly, local stability is simpler to demonstrate. Local stability suggests that $x(t)$ will converge to $x^\star$ provided the initial point $x(0)$ is sufficiently near the equilibrium point $x^\star$. With very few exceptions, the starting position for controlling converters and drives is near equilibrium, as demonstrated in the upcoming chapters. Consequently, a property's local stability is frequently sufficient.

A.1 Analysis of Local Stability by Linearization

If $x(t) \approx x^\star$ we have $f(x(t)) \approx 0$. Hence, $f(x(t))$ can be approximated as a first-order Taylor series expansion

$$f(x(t)) \approx \underbrace{f(x^\star)}_{0} + f'(x^\star)[x(t) - x^\star] \tag{A.1}$$

It therefore appears logical that close to an equilibrium point and can be approximated as a linear system

$$\dot{\bar{x}}(t) = A\bar{x}(t), \quad A = f'(x^\star) \tag{A.2}$$

where $\bar{x}(t) = x(t) - x^\star$.

Linearization is the most commonly used method for stability analysis of nonlinear systems and is also called Lyapunov's first (or indirect) method. The stability of the linearized system can be analyzed simply by calculating the eigenvalues of A. If we restrict the analysis to second-order systems, which is the case in the applications encountered in this research this matrix is given by:

$$A = f'(x^\star) = \left[\begin{array}{cc} \dfrac{\partial f_1(x_1, x_2)}{\partial x_1} & \dfrac{\partial f_1(x_1, x_2)}{\partial x_2} \\ \dfrac{\partial f_2(x_1, x_2)}{\partial x_1} & \dfrac{\partial f_2(x_1, x_2)}{\partial x_2} \end{array}\right]_{x=x^\star} \tag{A.3}$$

There are two eigenvalues, which we denote as λ_1 and λ_2, i.e., the characteristic polynomial is given by

$$(s - \lambda_1)(s - \lambda_2) = s^2 - \underbrace{(\lambda_1 + \lambda_2)}_{a_1} s + \underbrace{\lambda_1 \lambda_2}_{a_0} \tag{A.4}$$

The type of equilibrium point is determined by the signs of the real parts of the eigenvalues.

1. **Stable equilibrium point—sink**: $\mathrm{Re}\{\lambda_1\} < 0, \mathrm{Re}\{\lambda_2\} < 0$ ($a_1 > 0, a_0 > 0$). Any trajectory starting in the vicinity of $x^\star$ will converge to $x^\star$. The system behaves as an asymptotically stable linear system about $x^\star$.

2. **Unstable equilibrium point—source**: $\mathrm{Re}\{\lambda_1\} > 0$, $\mathrm{Re}\{\lambda_2\} > 0$ ($a_1 < 0, a_0 > 0$). Any trajectory starting in the vicinity of $x^\star$ will diverge from $x^\star$. The system behaves as an unstable linear system about $x^\star$.

3. **Unstable equilibrium point—saddle point**: $\lambda_1 > 0, \lambda_2 < 0$ ($a_0 < 0$). (The eigenvalues are in this case always real.) Trajectories close to a saddle point tend first to approach the saddle point and then move away from it. Hence, most trajectories starting in the vicinity of $x^\star$ will diverge from $x^\star$. Theoretically, there are also initial values $x(0)$ for which $x(t)$ will converge to $x^\star$. These are called the stable separatrices or stable manifolds, and are important, as they determine the stable regions about each sink.

4. **Center**: $\mathrm{Re}\{\lambda_1\} = \mathrm{Re}\{\lambda_2\} = 0$ ($a_1 = 0$). Nothing conclusive about stability can be said.

B Experimental Setup

Depicted in Figure B.1 is the experimental setup at the KTH Royal Institute of Technology Laboratory, featuring VPPIMs driven by a 36-leg inverter and managed by a control board incorporating a Xilinx ZynQ 7000 SoC ZC706.

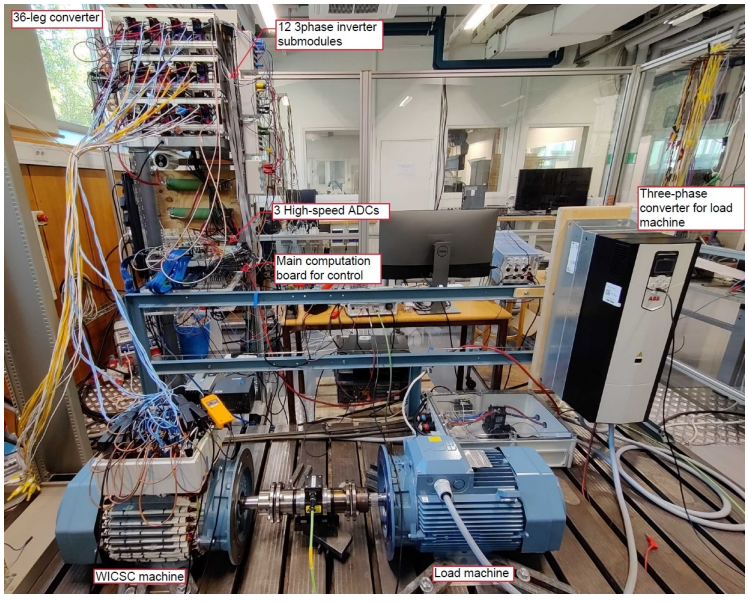

Figure B.1: The experimental setup for the verification of FEM-based parameter estimation.

C Experimental Setup

Figure C.1 illustrates the multiphase experimental setup at ABB, which comprises four three-phase converters (designated as C_1, C_2, C_3, and C_4) managed by an Opal-RT OP5700 system.

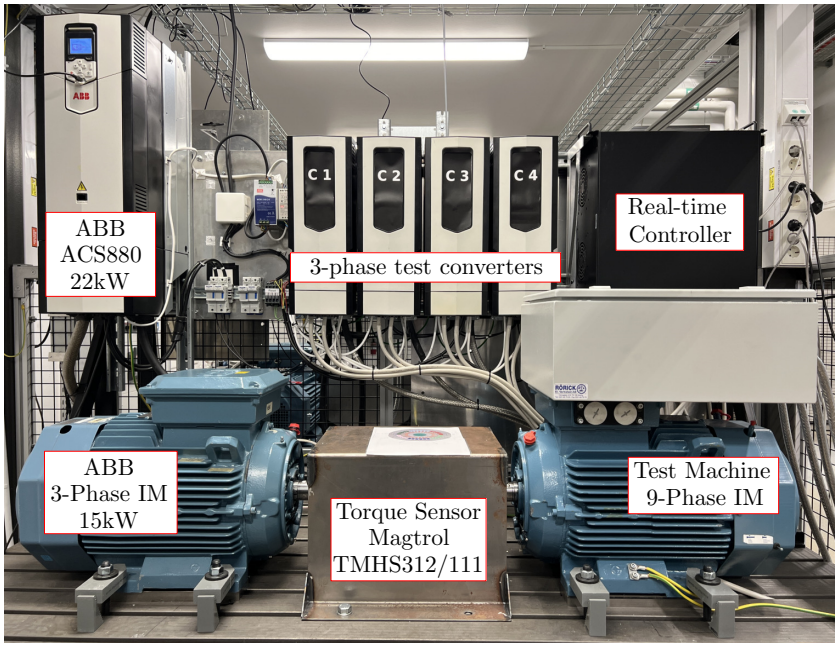

Figure C.1: Experimental test bench for the sensorless speed control.

Bibliography

[1] NOAA, **Assessing the Global Climate in July 2024**, doi: https://www.ncei.noaa.gov/news/global-climate-202407 (see pages 1, 2).

[2] B. Priest, A. Templeton, D. Helms, M. Yapur, and E. Miller, **Geospatial based analysis to assess noaa's ocean observing system architecture regarding requirement fulfillment**, in *OCEANS 2018 MTS/IEEE Charleston*, 2018, 1–4. DOI: 10.1109/OCEANS.2018.8604852 (see page 2).

[3] B. KONSTANTINA, **On Electrical Machine Topologies for Electric Vehicle Applications**, https://www.http://kth.diva-portal.org/smash/person.jsf?, Ph.D. dissertation, KTH Royal Institute of Technology, 2022 (see page 2).

[4] O. Ikram ul Haq, L. Peretti, and M. Hinkkanen, **Estimation of Equivalent Circuit Parameters of Multiphase Induction Machines by Exploitation of Space Harmonic Relations**, in *International Electric Machines & Drives Conference (IEMDC)*, San Francisco, California: IEEE, May 2023 (see pages 2, 47).

[5] Y. Wu, G. F. Olson, and L. Peretti, **Pole-transition control of variable-pole machines using harmonic-plane decomposition**, *IEEE Transactions on Industrial Electronics* (see pages 2, 4, 13, 20, 46, 52, 57, 65).

[6] L. Peretti and G. Zanuso, **Technology aspects and analytical modelling of multi-phase synchronous and induction machines**. Springer, 2019 (see page 3).

[7] Y. Wu, A. Pisani, G. F. Olson, K. Bitsi, O. Wallmark, and L. Peretti, **FEM-based parameter estimation for a variable phase-pole induction machine**, in *2021 23rd European Conference on Power Electronics and Applications (EPE'21 ECCE Europe)*, doi: https://doi.org/10.23919/EPE21ECCEEurope50061.2021.9570586, 2021, P.1–P.10 (see pages 5, 32, 36, 37, 39, 40).

[8] Y. Zhao and T. Lipo, **Modeling and control of a multi-phase induction machine with structural unbalance**, *IEEE Transactions on Energy Conversion*, vol. 11:no. 3, 570–577. DOI: 10.1109/60.537009 (see pages 5, 17).

[9] D. motion, **Darwin Motion**, doi: https://darwinmotion.com/tower-crane-applications.php (see page 8).

[10] E. Levi, **Multiphase electric machines for variable-speed applications**, *IEEE Transactions on Industrial Electronics*, vol. 55:no. 5, 1893–1909. DOI: 10.1109/TIE.2008.918488 (see page 11).

[11] F. Barrero and M. J. Duran, **Recent advances in the design, modeling, and control of multiphase machines—part i**, *IEEE Transactions on Industrial Electronics*, vol. 63:no. 1, 449–458. DOI: 10.1109/TIE.2015.2447733 (see page 12).

[12] H. S. Juan Juanchi, A. Chiba, and M. Kobayashi, **Performance evaluation of a nine-phase induction motor using finite element analysis**, in *2020 23rd International Conference on Electrical Machines and Systems (ICEMS)*, 2020, 1472–1477. DOI: 10.23919/ICEMS50442.2020.9290783 (see page 12).

[13] G. Renukadevi and K. Rajambal, **Generalized model of multi-phase induction motor drive using matlab/simulink**, in *ISGT2011-India*, 2011, 114–119. DOI: 10.1109/ISET-India.2011.6145366 (see page 12).

[14] I. Zoric, M. Jones, and E. Levi, **Vector space decomposition algorithm for asymmetrical multiphase machines**, in *2017 International Symposium on Power Electronics (Ee)*, 2017, 1–6. DOI: 10.1109/PEE.2017.8171682 (see pages 13, 32).

[15] K. Bitsi, O. Wallmark, and S. Bosga, **An induction machine with wound independently-controlled stator coils**, in *2019 22nd International Conference on Electrical Machines and Systems (ICEMS)*, 2019, 1–5. DOI: 10.1109/ICEMS.2019.8921779 (see page 13).

[16] J. Maes and J. Melkebeek, **Speed-sensorless direct torque control of induction motors using an adaptive flux observer**, *IEEE Transactions on Industry Applications*, vol. 36:no. 3, 778–785. DOI: 10.1109/28.845053 (see pages 13, 46, 48–50).

[17] Y. Wu, G. F. Olson, L. Peretti, and O. Wallmark, **Harmonic plane decomposition: An extension of the vector-space decomposition - part I**, in *IECON 2020 The 46th Annual Conference of the IEEE Industrial Electronics Society*, vol. 2020, doi: https://doi.org/10.1109/IECON43393.2020.9255228, 2020, 985–990 (see pages 13, 32, 38–40).

[18] G. F. Olson, Y. Wu, L. Peretti, and O. Wallmark, **Harmonic plane decomposition: An extension of the vector-space decomposition - part II**, in *IECON 2020 The 46th Annual Conference of the IEEE Industrial Electronics Society*, doi: https://doi.org/10.1109/IECON43393.2020.9254279, 2020, 991–996 (see pages 13, 38, 39).

[19] P. C. Nguyen, Q. D. Phan, and D. T. Nguyen, **Implementation decentralized space vector pwm method for multilevel multiphase converters**, *IEEE Access*, vol. 12, 20663–20678. DOI: 10.1109/ACCESS.2024.3358204 (see page 13).

[20] M. Bojarski, E. Asa, M. T. Outeiro, and D. Czarkowski, **Control and analysis of multi-level type multi-phase resonant converter for wireless ev charging**, in *IECON 2015 - 41st Annual Conference of the IEEE Industrial Electronics Society*, 2015, 005008–005013. DOI: 10.1109/IECON.2015.7392886 (see page 13).

[21] Z. Yu and J. Long, **Review on advanced model predictive control technologies for high-power converters and industrial drives**, *Electronics*, vol. 13:no. 24, ISSN: 2079-9292. DOI: 10.3390/electronics13244969. [Online]. Available: https://www.mdpi.com/2079-9292/13/24/4969 (see page 14).

[22] S. Aslam, M. Shamkuwar, S. B. G. T. Babu, J. Suresh, P. G, and N. L, **Smart multiphase power converter in the fault-tolerant machine development for aerospace applications**, in *2024 Ninth International Conference on Science Technology Engineering and Mathematics (ICONSTEM)*, 2024, 1–5. DOI: 10.1109/ICONSTEM60960.2024.10568598 (see page 14).

[23] L. de Lillo, L. Empringham, P. W. Wheeler, S. Khwan-On, C. Gerada, M. N. Othman, and X. Huang, **Multiphase power converter drive for fault-tolerant machine development in aerospace applications**, *IEEE Transactions on Industrial Electronics*, vol. 57:no. 2, 575–583. DOI: 10.1109/TIE.2009.2036026 (see page 14).

[24] H. Matsumoto, H. Takami, and R. Takase, **Vector control scheme for an induction motor controlled by a voltage model-operation with current control loop**, in *Conference Record of the IEEE Industry Applications Society Annual Meeting,* 1989, 368–374 vol.1. DOI: 10.1109/IAS.1989.96678 (see page 14).

[25] L. Parsa and H. A. Toliyat, **Sensorless direct torque control of five-phase interior permanent-magnet motor drives**, *IEEE Transactions on Industry Applications*, vol. 43:no. 4, 952–959. DOI: 10.1109/TIA.2007.900444 (see pages 14, 15).

[26] N. A. Ahmed, B. N. Alajmi, I. Abdelsalam, and M. I. Marei, **Soft switching multiphase interleaved boost converter with high voltage gain for ev applications**, *IEEE Access*, vol. 10, 27698–27716. DOI: 10.1109/ACCESS.2022.3157050 (see page 15).

[27] H. Guo, R. Wang, W. Kong, and R. Qu, **Design of multiphase inverter system for variable-speed applications based on dsp and fpga**, in *2019 22nd International Conference on Electrical Machines and Systems (ICEMS)*, 2019, 1–4. DOI: 10.1109/ICEMS.2019.8921773 (see page 15).

[28] E. Levi, **Advances in converter control and innovative exploitation of additional degrees of freedom for multiphase machines**, *IEEE Transactions on Industrial Electronics*, vol. 63:no. 1, 433–448. DOI: 10.1109/TIE.2015.2434999 (see page 15).

[29] Ó. Lopez, J. Alvarez, J. Doval-Gandoy, and F. D. Freijedo, **Multilevel multiphase space vector pwm algorithm**, *IEEE Transactions on Industrial Electronics*, vol. 55:no. 5, 1933–1942. DOI: 10.1109/TIE.2008.918466 (see page 15).

[30] O. Lopez, J. Alvarez, J. Doval-Gandoy, and F. D. Freijedo, **Multilevel multiphase space vector pwm algorithm with switching state redundancy**, *IEEE Transactions on Industrial Electronics*, vol. 56:no. 3, 792–804. DOI: 10.1109/TIE.2008.2004390 (see page 15).

[31] Z. Liu, Z. Zheng, L. Xu, K. Wang, and Y. Li, **Current balance control for symmetrical multiphase inverters**, *IEEE Transactions on Power Electronics*, vol. 31:no. 6, 4005–4012. DOI: 10.1109/TPEL.2015.2508142 (see page 15).

[32] R. Shi and H. Toliyat, **Vector control of five-phase synchronous reluctance motor with space vector pulse width modulation (svpwm) for minimum switching losses**, in *APEC. Seventeenth Annual IEEE Applied Power Electronics Conference and Exposition (Cat. No.02CH37335)*, vol. 1, 2002, 57–63 vol.1. DOI: 10.1109/APEC.2002.989227 (see page 15).

[33] K. Gopakumar, V. Ranganthan, and S. Bhat, **Split-phase induction motor operation from pwm voltage source inverter**, *IEEE Transactions on Industry Applications*, vol. 29:no. 5, 927–932. DOI: 10.1109/28.245716 (see page 15).

[34] Z. Xue, S. Niu, A. M. H. Chau, Y. Luo, H. Lin, and X. Li, **Recent advances in multi-phase electric drives model predictive control in renewable energy application: A state-of-the-art review**, *World Electric Vehicle Journal*, vol. 14:no. 2, ISSN: 2032-6653. DOI: 10.3390/wevj14020044. [Online]. Available: https://www.mdpi.com/2032-6653/14/2/44 (see page 16).

[35] M. P. Magill, P. T. Krein, and K. S. Haran, **Equivalent circuit model for pole-phase modulation induction machines**, in *2015 IEEE International Electric Machines and Drives Conference (IEMDC)*, 2015, 293–299. DOI: 10.1109/IEMDC.2015.7409074 (see page 16).

[36] E. Libbos, B. Ku, S. Agrawal, S. Tungare, A. Banerjee, and P. T. Krein, **Variable-pole induction machine drive for electric vehicles**, in *2019 IEEE International Electric Machines and Drives Conference (IEMDC)*, 2019, 515–522. DOI: 10.1109/IEMDC.2019.8785212 (see page 16).

[37] R. Raj, P. Subramaniyane, and L. Peretti, **Design of a variable phase-pole induction machine for electric vehicle applications**, in *2022 International Conference on Electrical Machines (ICEM)*, 2022, 976–982. DOI: 10.1109/ICEM51905.2022.9910688 (see pages 16, 21, 23).

[38] G. Kovács, **Calculation of synchronous torques and radial magnetic forces for pole-changing winding using the 3//y / 3//y method**, in *2020 International Conference on Electrical Machines (ICEM)*, vol. 1, 2020, 90–96. DOI: 10.1109/ICEM49940.2020.9270765 (see page 17).

[39] D. Sun, B. Ge, and D. Bi, **Winding design for pole-phase modulation of induction machines**, in *2010 IEEE Energy Conversion Congress and Exposition*, 2010, 278–283. DOI: 10.1109/ECCE.2010.5618026 (see page 17).

[40] Y. Wu, G. F. Olson, L. Peretti, and O. Wallmark, **Harmonic plane decomposition: An extension of the vector-space decomposition - part i**, in *IECON 2020 The 46th Annual Conference of the IEEE Industrial Electronics Society*, 2020, 985–990. DOI: 10.1109/IECON43393.2020.9255228 (see pages 17, 46).

[41] M. Osama and T. Lipo, **Experimental and finite element analysis of an electronic pole-change drive**, in *Conference Record of the 1999 IEEE Industry Applications Conference. Thirty-Forth IAS Annual Meeting (Cat. No.99CH36370)*, vol. 2, 1999, 914–921 vol.2. DOI: 10.1109/IAS.1999.801617 (see pages 17, 21).

[42] E. Libbos, S. Chaubal, A. Maheshwari, A. Banerjee, and P. T. Krein, **Bumpless electronic pole changing for variable-pole induction machines**, *IEEE Transactions on Transportation Electrification*, 1–1. DOI: 10.1109/TTE.2024.3401613 (see page 17).

[43] B. Daniels, J. Gurung, H. Huisman, and E. Lomonova, **Feasibility study of multi-phase machine winding reconfiguration for fully electric vehicles**, in *2019 Fourteenth International Conference on Ecological Vehicles and Renewable Energies (EVER)*, 2019, 1–6. DOI: 10.1109/EVER.2019.8813594 (see page 17).

[44] M. P. Magill, **An investigation of electronic pole changing in high inverter count induction machines**, https://www.ideals.illinois.edu/items/79621, Ph.D. dissertation, University of Illinois at Urbana-Champaign, 2015 (see pages 17, 21, 32, 33, 46).

[45] A. S. Abdel-Khalik, A. Massoud, and S. Ahmed, **Nine-phase six-terminal pole-amplitude modulated induction motor for electric vehicle applications**, *IET Electric Power Applications*, vol. 13:no. 11, 1696–1707 (see page 17).

[46] J. A. Riveros, A. G. Yepes, F. Barrero, J. Doval-Gandoy, B. Bogado, O. Lopez, M. Jones, and E. Levi, **Parameter identification of multiphase induction machines with distributed windings—part 2: Time-domain techniques**, *IEEE Transactions on Energy Conversion*, vol. 27:no. 4, 1067–1077. DOI: 10.1109/TEC.2012.2219862 (see page 18).

[47] H. Hussain, J. Yang, and G. Yang, **Harmonic and fundamental rotor resistance estimation scheme for multiphase induction motor based on nonsinusoidal supply control**, *IEEE Journal of Emerging and Selected Topics in Power Electronics*, vol. 10:no. 2, 2052–2064. DOI: 10.1109/JESTPE.2021.3136285 (see page 18).

[48] A. M. Fadel, A. S. Abdel-Khalik, and R. A. Hamdy, **Genetic algorithm based parameter estimation of six-phase induction machine sequence circuits**, in *2021 22nd International Middle East Power Systems Conference (MEPCON)*, 2021, 233–238. DOI: 10.1109/MEPCON50283.2021.9686302 (see page 18).

[49] W. Li, G. Feng, Z. Li, M. S. Toulabi, and N. C. Kar, **Extended kalman filter based inductance estimation for dual three-phase permanent magnet synchronous motors under the single open-phase fault**, *IEEE Transactions on Energy Conversion*, vol. 37:no. 2, 1134–1144. DOI: 10.1109/TEC.2021.3129283 (see page 18).

[50] M. I. Abdelwanis, R. A. Sehiemy, and M. A. Hamida, **Hybrid optimization algorithm for parameter estimation of poly-phase induction motors with experimental verification**, *Energy and AI*, vol. 5, 100083, ISSN: 2666-5468. DOI: https://doi.org/10.1016/j.egyai.2021.100083. [Online]. Available: https://www.sciencedirect.com/science/article/pii/S2666546821000379 (see page 18).

[51] S. H. Kia, H. Henao, and G.-A. Capolino, **A high-resolution frequency estimation method for three-phase induction machine fault detection**, *IEEE Transactions on Industrial Electronics*, vol. 54:no. 4, 2305–2314. DOI: 10.1109/TIE.2007.899826 (see page 19).

[52] A. G. Yepes, J. A. Riveros, J. Doval-Gandoy, F. Barrero, Ó. Lopez, B. Bogado, M. Jones, and E. Levi, **Parameter identification of multiphase induction machines with distributed windings part 1: Sinusoidal excitation methods**, *IEEE Trans. Energy Convers.*, vol. 27:no. 4, doi: http://dx.doi.org/10.1109/TEC.2012.2220967, 1056–1066 (see pages 19, 32).

[53] H. Toliyat, E. Levi, and M. Raina, **A review of rfo induction motor parameter estimation techniques**, *IEEE Transactions on Energy Conversion*, vol. 18:no. 2, 271–283. DOI: 10.1109/TEC.2003.811719 (see pages 19, 32).

[54] A. G. Yepes, F. Baneira, J. Malvar, A. Vidal, D. Pérez-Estévez, O. López, and J. Doval-Gandoy, **Selection criteria of multiphase induction machines for speed-sensorless drives based on rotor slot harmonics**, *IEEE Transactions on Industrial Electronics*, vol. 63:no. 8, 4663–4673. DOI: 10.1109/TIE.2016.2548979 (see page 20).

[55] S. R. Arya and M. Pudari, **Sensorless adaptive control of vsi-fed induction motor drive with optimized mlp-neural network**, *Australian Journal of Electrical and Electronics Engineering*, vol. 20:no. 3, 291–308. DOI: 10.1080/1448837X.2023.2206598. [Online]. Available: https://doi.org/10.1080/1448837X.2023.2206598 (see page 20).

[56] H. Zhao, D. Wang, X. Yi, and P. Hu, **Sensorless control of multiphase permanent magnet synchronous motor considering phase-to-phase coupling**, in *The proceedings of the 10th Frontier Academic Forum of Electrical Engineering (FAFEE2022)*, X. Dong, Q. Yang, and W. Ma, Eds., Singapore: Springer Nature Singapore, 2023, 461–472, ISBN: 978-981-99-3408-9 (see page 20).

[57] C. Liu and J. Shang, **Sensorless drive strategy of open-end winding pmsm with zero-sequence current suppression**, *IEEE Transactions on Energy Conversion*, vol. 36:no. 4, 2987–2997. DOI: 10.1109/TEC.2021.3069891 (see page 20).

[58] B. S. S. G. Yelamarthi and S. R. Sandepudi, **Predictive torque control of three-phase induction motor drive with inverter switch fault-tolerance capabilities**, *IEEE Journal of Emerging and Selected Topics in Power Electronics*, vol. 9:no. 3, 2774–2788. DOI: 10.1109/JESTPE.2020.3020328 (see page 20).

[59] M. P. Magill and P. T. Krein, **A dynamic pole-phase modulation induction machine model**, *2015 IEEE International Electric Machines & Drives Conference (IEMDC)*, 13–19 (see page 20).

[60] J. Holtz, **Sensorless control of induction machines—with or without signal injection?** *IEEE Transactions on Industrial Electronics*, vol. 53:no. 1, 7–30. DOI: 10.1109/TIE.2005.862324 (see pages 20, 46).

[61] L. Harnefors and R. Ottersten, **Regenerating-mode stabilization of the "statically compensated voltage model"**, *IEEE Transactions on Industrial Electronics*, vol. 54:no. 2, 818–824. DOI: 10.1109/TIE.2007.891781 (see page 20).

[62] J. Choi, G. C. Lim, C. Hwang, B. R. Park, and J.-I. Ha, **Feedback gain design of induction machine full-order flux observer**, *IEEE Transactions on Industrial Electronics*, vol. 70:no. 10, 9870–9881. DOI: 10.1109/TIE.2022.3217605 (see page 20).

[63] J. Chen, X. Yuan, F. Blaabjerg, and C. H. T. Lee, **Overview of fundamental frequency sensorless algorithms for ac motors: A unified perspective**, *IEEE Journal of Emerging and Selected Topics in Power Electronics*, vol. 11:no. 1, 915–931. DOI: 10.1109/JESTPE.2022.3194520 (see page 20).

[64] B. Ge, D. Sun, W. Wu, and F. Z. Peng, **Winding design, modeling, and control for pole-phase modulation induction motors**, *IEEE Transactions on Magnetics*, vol. 49:no. 2, 898–911 (see pages 21, 23).

[65] G. Dajaku and D. Gerling, **Low costs and high efficiency asynchronous machine with stator cage winding**, in *IEEE International Electric Vehicle Conference (IEVC 2014)*, doi: http://dx.doi.org/10.1109/IEVC.2014.7056083, IEEE, 2014, 1–6 (see pages 21, 33).

[66] K. Bitsi, O. Wallmark, and S. Bosga, **An Induction Machine with Wound Independently-Controlled Stator Coils**, *22nd International Conference on Electrical Machines and Systems (ICEMS 2019)*, vol. 1, doi: http://dx.doi.org/10.1109/ICEMS.2019.8921779 (see pages 21, 22, 33).

[67] L. Ou, X. Wang, and W. Pan, **Study on the effect of permanent magnets in a novel pole-changing motor**, in *2016 19th International Conference on Electrical Machines and Systems (ICEMS)*, 2016, 1–4 (see page 21).

[68] Y. Matsuyama, K. Ishizuka, T. Kosaka, H. Matsumori, and N. Matsui, **Design study on high torque density multiphase pole-change induction motor for vehicle propulsion drive**, in *2021 24th International Conference on Electrical Machines and Systems (ICEMS)*, 2021, 426–431. DOI: 10.23919/ICEMS52562.2021.9634455 (see page 21).

[69] A. Gautam, O. Ojo, M. Ramezani, and O. Momoh, **Computation of equivalent circuit parameters of nine-phase induction motor in different operating modes**, in *2012 IEEE Energy Conversion Congress and Exposition (ECCE)*, doi: https://doi.org/10.1109/ECCE.2012.6342830, 2012, 142–149 (see pages 21, 32).

[70] E. Libbos, R. Hao, B. Ku, A. Banerjee, and P. T. Krein, **Modular multiphase drives for variable-pole induction machines in electric vehicles**, in *2020 IEEE Applied Power Electronics Conference and Exposition (APEC)*, 2020, 696–703. DOI: 10.1109/APEC39645.2020.9124085 (see page 21).

[71] M. Tilahune, G. F. Olson, L. Peretti, and M. Mamo, **Validation of fem-based parameter estimation for variable phase-pole induction machines**, *IEEE Transactions on Energy Conversion*, 1–8. DOI: 10.1109/TEC.2023.3272950 (see pages 22, 24, 46).

[72] A. Arkkio, **Analysis of induction motors based on the numerical solution of the magnetic field and circuit equations**, English, Doctoral thesis, Acta polytechnica Scandinavica. El, Electrical engineering series; 59, 1987, 97, ISBN: 951-22-6076-X (see pages 23, 24, 26).

[73] O. Wallmark, **AC Machine Analysis: Fundamental Theory**. Division of Electric Power and Energy Systems, KTH Royal Institute of Technology, 2020 (see pages 23, 25, 26, 44, 45).

[74] M. Osama and T. A. Lipo, **Modeling and analysis of a wide-speed-range induction motor drive based on electronic pole changing**, *IEEE Trans. Appl. Ind.*, vol. 33:no. 5, doi: http://dx.doi.org/10.1109/28.633794, 1177–1184 (see page 32).

[75] E. Libbos, E. Krause, A. Banerjee, and P. T. Krein, **Inverter design considerations for variable-pole induction machines in electric vehicles**, *IEEE Transactions on Power Electronics*, vol. 37:no. 11, doi: http://dx.doi.org/10.1109/TPEL.2022.3177082, 13554–13565 (see pages 32, 46).

[76] E. Libbos, B. Ku, S. Agrawal, S. Tungare, A. Banerjee, and P. T. Krein, **Loss minimization and maximum torque-per-ampere operation for variable-pole induction machines**, *IEEE Trans. on Trans. Electr.*, vol. 6:no. 3, doi: https://doi.org/10.1109/TTE.2020.2997692, 1051–1064 (see page 32).

[77] C. Grantham and D. McKinnon, **Rapid parameter determination for induction motor analysis and control**, *IEEE Transactions on Industry Applications*, vol. 39:no. 4, doi: http://dx.doi.org/10.1109/TIA.2003.813737, 1014–1020 (see page 32).

[78] L. Peretti and M. Zigliotto, **Automatic procedure for induction motor parameter estimation at standstill**, *IET Electric Power Applications*, vol. 6:no. 4, doi: http://dx.doi.org/10.1049/iet-epa.2010.0262, 214–224 (see page 32).

[79] J. A. Riveros, A. G. Yepes, F. Barrero, J. Doval-Gandoy, B. Bogado, O. Lopez, M. Jones, and E. Levi, **Parameter identification of multiphase induction machines with distributed windings part 2: Time-domain techniques**, *IEEE Trans. Energy Convers.*, vol. 27:no. 4, doi: http://dx.doi.org/10.1109/TEC.2012.2219862, 1067–1077 (see page 32).

[80] Y. Wang, J. Yang, R. Deng, and G. Yang, **Parameters estimation for multiphase induction machine with concentrated windings through finite element method**, *IET Electric Power Applications*, vol. 14:no. 10, doi: http://dx.doi.org/10.1049/iet-epa.2019.0869, 1807–1817 (see page 32).

[81] G. Falk Olson and L. Peretti, **Parameter estimation of multiphase machines applicable to variable phase-pole machines**, in *2022 International Conference on Electrical Machines (ICEM) :* Part of proceedings: ISBN 978-1-6654-1432-6QC 20221021, Institute of Electrical and Electronics Engineers (IEEE), 2022, 949–955. DOI: 10.1109/ICEM51905.2022.9910883 (see pages 32, 41).

[82] D. Meeker, **Finite element method magnetics: Induction motor example**, *Induction Motor Example*. [Online]. Available: https://www.femm.info/wiki/InductionMotorExample (see pages 34, 35).

[83] T. A. Lipo, **Introduction to AC machine design**. Hoboken: IEEE Press series on power engineering, 2017, doi: http://dx.doi.org/10.1002/9781119352181 (see pages 36, 38, 40).

[84] A. A. Rockhill and T. A. Lipo, **A generalized transformation methodology for polyphase electric machines and networks**, in *2015 IEEE International Electric Machines & Drives Conference (IEMDC)*, doi: http://dx.doi.org/10.1109/IEMDC.2015.7409032, 2015, 27–34 (see page 39).

[85] M. Hinkkanen, A. K. Repo, M. Ranta, and J. Luomi, **Small-signal modeling of mutual saturation in induction machines**, *IEEE Trans. Appl. Ind.*, vol. 46:no. 3, doi: http://dx.doi.org/10.1109/TIA.2010.2046290, 965–973 (see page 44).

[86] O. I. u. Haq, Y. Wu, L. Peretti, S. G. Bosga, and R. S. Kanchan, **Generalized harmonic injection strategy for multiphase induction machine control**, *IEEE Transactions on Energy Conversion*, 1–10. DOI: 10.1109/TEC.2023.3331233 (see page 46).

[87] G. F. Olson, Y. Wu, O. I. U. Haq, and L. Peretti, **Enabling variable phase-pole drives with the harmonic plane decomposition**, *IEEE Access*, vol. 12, 40049–40063. DOI: 10.1109/ACCESS.2024.3375752 (see pages 46, 47).

[88] T. Latif, S. Agoro, M. Z. M. Jaffar, and I. Husain, **Control of a 4-pole/2-pole electronic pole-changing induction motor for traction applications**, *IEEE Transactions on Industry Applications*, vol. 59:no. 6, 6704–6714. DOI: 10.1109/TIA.2023.3307090 (see page 46).

[89] S. V. S. P. K. Ch, V. Sonti, and S. Jain, **Gradual electronic pole changing technique to minimize the circulating currents during pole/mode transition in induction motor drive**, *IEEE Transactions on Industry Applications*, vol. 59:no. 1, 959–969. DOI: 10.1109/TIA.2022.3207984 (see page 46).

[90] T. Latif, S. Agoro, M. Z. M. Jaffar, and I. Husain, **Dynamic loss minimization control of a 4-pole/2-pole electronic pole-changing induction motor using a look-up table**, *IEEE Transactions on Industry Applications*, vol. 59:no. 6, 6715–6725. DOI: 10.1109/TIA.2023.3307054 (see page 46).

[91] M. Hinkkanen and J. Luomi, **Stabilization of regenerating-mode operation in sensorless induction motor drives by full-order flux observer design**, *IEEE Transactions on Industrial Electronics*, vol. 51:no. 6, 1318–1328. DOI: 10.1109/TIE.2004.837902 (see pages 46, 48–50, 54, 58).

[92] S. J. Rind, A. Amjad, and M. Jamil, **Rotor flux mras based speed sensorless indirect field oriented control of induction motor drive for electric and hybrid electric vehicles**, in *2018 53rd International Universities Power Engineering Conference (UPEC)*, 2018, 1–6. DOI: 10.1109/UPEC.2018.8542009 (see page 46).

[93] H. Chen, J. Li, Y. Lu, K. Yang, L. Wu, and Z. Liu, **Stability improvement of adaptive full-order observer for sensorless induction motor drives in low-speed regenerating mode**, *IEEE Transactions on Transportation Electrification*, vol. 10:no. 1, 8–18. DOI: 10.1109/TTE.2023.3257056 (see pages 46, 50).

[94] Z. Wu, C. Cheng, W. Hua, and H. Zhang, **A high-frequency signal injection-based sensorless control method robust to single and double open-phase faults for a dual three-phase motor**, *IEEE Transactions on Power Electronics*, vol. 38:no. 12, 16010–16021. DOI: 10.1109/TPEL.2023.3315238 (see page 46).

[95] H. Kubota, I. Sato, Y. Tamura, K. Matsuse, H. Ohta, and Y. Hori, **Regenerating-mode low-speed operation of sensorless induction motor drive with adaptive observer**, *IEEE Transactions on Industry Applications*, vol. 38:no. 4, 1081–1086. DOI: 10.1109/TIA.2002.800575 (see page 46).

[96] W. Sun, Y. Yu, G. Wang, B. Li, and D. Xu, **Design method of adaptive full order observer with or without estimated flux error in speed estimation algorithm**, *IEEE Transactions on Power Electronics*, vol. 31:no. 3, 2609–2626. DOI: 10.1109/TPEL.2015.2440373 (see page 46).

[97] B. Chen, W. Yao, F. Chen, and Z. Lu, **Parameter sensitivity in sensorless induction motor drives with the adaptive full-order observer**, *IEEE Transactions on Industrial Electronics*, vol. 62:no. 7, 4307–4318. DOI: 10.1109/TIE.2014.2388197 (see page 46).

[98] G. F. Olson, Y. Wu, L. Peretti, and O. Wallmark, **Harmonic plane decomposition: An extension of the vector-space decomposition - part ii**, in *IECON 2020 The 46th Annual Conference of the IEEE Industrial Electronics Society*, 2020, 991–996. DOI: 10.1109/IECON43393.2020.9254279 (see page 46).

[99] G. F. Olson, Y. Wu, and L. Peretti, **Parameter estimation of multiphase machines applicable to variable phase-pole machines**, *IEEE Transactions on Energy Conversion*, 1–10. DOI: 10.1109/TEC.2023.3288368. [Online]. Available: https://ieeexplore.ieee.org/document/9910883 (see pages 46, 47).

[100] O. Ikram ul Haq, L. Peretti, S. G. Bosga, and R. S. Kanchan, **Online Winding Reconfiguration of a Multiphase Stator**, in *Power Electronics & Drive Systems (PEDS)*, Montreal, Canada: IEEE, Aug. 2023 (see page 47).

[101] E. Libbos, B. Ku, S. Agrawal, S. Tungare, A. Banerjee, and P. T. Krein, **Loss minimization and maximum torque-per-ampere operation for variable-pole induction machines**, *IEEE Journal of Emerging and Selected Topics in Industrial Electronics*, vol. 6:no. 3, 1051–1064. [Online]. Available: https://doi.org/10.1109/TTE.2020.2997692 (see pages 48, 57).

[102] S. V. S. P. K. Ch, V. Sonti, S. Jain, and B. Singh, **High-frequency model for analysing leakage currents in electronic pole-changing induction motor drive**, *IEEE Journal of Emerging and Selected Topics in Industrial Electronics*, 1–11. [Online]. Available: https://doi.org/10.1109/JESTIE.2025.3531757 (see page 48).

[103] M. P. Magill and P. T. Krein, **A dynamic pole-phase modulation induction machine model**, in *2015 IEEE International Electric Machines and Drives Conference (IEMDC)*, 2015, 13–19. [Online]. Available: https://doi.org/10.1109/IEMDC.2015.7409030 (see page 48).

[104] M. Hinkkanen, **Analysis and design of full-order flux observers for sensorless induction motors**, *IEEE Transactions on Industrial Electronics*, vol. 51:no. 5, 1033–1040. DOI: 10.1109/TIE.2004.834964 (see page 57).

[105] M. Hinkkanen and J. Luomi, **Parameter sensitivity of full-order flux observers for induction motors**, in *Conference Record of the 2002 IEEE Industry Applications Conference. 37th IAS Annual Meeting (Cat. No.02CH37344)*, vol. 2, 2002, 851–855 vol.2. DOI: 10.1109/IAS.2002.1042658 (see page 68).